
University *of* Leicester

# Solar wind charge exchange emission in the Earth's exosphere and its contribution to the XMM-Newton X-ray background

**Thesis submitted for the degree of**

**Doctor of Philosophy**

**at the University of Leicester**

**by**


## Jennifer Alyson Carter

**X-Ray & Observational Astronomy Group**

**Department of Physics and Astronomy**

**University of Leicester**


**August 30, 2011**

# Copyright

# Declaration

I hereby declare that no part of this thesis has been previously submitted to this, or any other University as part of the requirement for a higher degree. The work described herein was conducted by the undersigned, except for contributions from colleagues as acknowledged in the text.

Jennifer Alyson Carter

Leicester, 2011

*Y si un día me siento transformado,*
*y decido reorientar la dirección,*
*tomaré un nuevo rumbo sin prejuicios*
*porque en el cambio está la evolución.*

Chambao, Dibujo en el aire

# Solar wind charge exchange emission in the Earth's exosphere and its contribution to the XMM-Newton X-ray background

**Jennifer Alyson Carter**

## Abstract

The XMM-*Newton* observatory provides unrivalled capabilities for detecting low surface brightness emission features from extended and diffuse sources, by virtue of its large field-of-view (15 arcminutes in radius) and high effective area (2150 $cm^2$ at 1 keV). XMM-*Newton* observes X-ray emission along its entire line-of-sight, whether that be the intended, generally distant astronomical target, or from much closer, for example within the Solar System. The main motivation of this thesis was to characterise one source of locally produced, diffuse X-ray emission; that of solar wind charge exchange (SWCX) interactions between solar wind ions and neutral atoms in the Earth's exosphere.

Whilst SWCX is a source of background for astrophysicists concerned with studies of Galactic and extragalactic emission, it provides a diagnostic of the charge-state distribution of the solar wind and mass transport around the Earth's magnetosheath. This thesis describes an archival study of XMM-*Newton* observations to identify those affected by temporally-variable SWCX emission. 3.4% of 3012 XMM-*Newton* observations studied unambiguously contain a variable exospheric SWCX signal; they are preferentially detected around the sub-solar point of the Earth's magnetosheath.

This thesis contains a detailed investigation into the temporal and spectral characteristics of the SWCX-affected observations. It also contains a study of one particular observation, whose emission likely resulted from Coronal Mass Ejection plasma moving through the vicinity of the Earth. A model of exospheric SWCX is presented to provide some predictive power, using the orbital and target-pointing parameters of XMM-*Newton* during a particular observation. The model is in reasonable agreement with the observed fluxes for approximately 60% of cases.

Finally, an idea for a future wide-field X-ray imager with an accompanying plasma monitor and magnetometer is presented. This would observe plasma dynamics in the Earth's magnetosheath via the mechanism of SWCX emission occurring in this region.

# Acknowledgements

Since starting at Leicester and throughout the work for this thesis, both Steve Sembay and Andrew Read have been the most patient, professional and helpful supervisors I could have wished for; thank you for the daily support, advice, time and supervision and also for the positive working environment within the team. Thank you to my academic supervisors George Fraser and Robert Warwick for the guidance over the past few years.

I would like to thank Andy Pollock at ESAC for giving me the fantastic opportunity to join the XMM-*Newton* community and for the ongoing support and enlightening discussions. I would also like to thank Richard Saxton for all the help during my time at ESAC. Thank you to Marcus Kirsch for welcoming me into the ESAC trainee group. From Leicester, I would like to express my thanks to Simon Vaughan for helpful discussions at the beginning of this work and to Martin Turner for the professional inspiration and for encouraging me to make a decision. Thank you to the XMM-*Newton* EPIC background working group and calibration teams, in particular to Steve Snowden, Kip Kuntz and Konrad Dennerl for their extra advice. I have gained so much from the most recent collaborations in my work; many thanks to the *MagEX*, STORM and AXIOM proposal teams. I have used both the IDL Astronomy and Coyote IDL programme libraries extensively throughout my work and I would like to acknowledge the vast resource of open-source software that is available and that I use daily.

Thank you to my parents, my sister Jaclyn and my partner Rafa for the unwavering unconditional love, encouragement and support that is always there; this thesis is dedicated to you. This journey started a long time ago and without the guidance of amazing family, friends and teachers it would never have happened. Thank you especially to Mr Quick, who truly inspired me. To my family, Mel, Will, Ali, Ash and the Bristol crowd for the friendship, laughter and motivation. To Pat, Kris, Valentina, Silvia, Mao and Gaut for the everyday support and keeping things in perspective. Thank you also to my friends from ESAC and in Madrid for whom the distance never matters; Carmen, Ana, Mar, Celia, Flori, Isa, Paul, Rubén, Aure, Gabi, Alfonso, Enrico, Elena and Héctor and especially to Pili.

# List of publications

- CARTER, J. A., SEMBAY, S. & READ, A. M. (2011). Identifying XMM-Newton observations affected by solar wind charge exchange - Part II. *A&A*, 527, A115+
- CARTER, J. A., SEMBAY, S. & READ, A. M. (2010). A high charge state coronal mass ejection seen through solar wind charge exchange emission as detected by XMM-Newton. *MNRAS*, 402, 867–878
- CARTER, J. A. & SEMBAY, S. (2008). Identifying XMM-Newton observations affected by solar wind charge exchange. Part I. *A&A*, 489, 837–848
- CARTER, J. A. & READ, A. M. (2007). The XMM-Newton EPIC background and the production of background blank sky event files. *A&A*, 464, 1155–1166
- BRANDUARDI-RAYMONT, G., SEMBAY, S. F., EASTWOOD, J. P., SIBECK, D. G., ABBEY, A. ET AL. (2011). AXIOM: Advanced X-ray Imaging Of the Magnetosphere. *ArXiv e-prints*
- BODEWITS, D., VILLANUEVA, G. L., MUMMA, M. J., LANDSMAN, W. B., CARTER, J. A. ET AL. (2011). Swift-UVOT Grism Spectroscopy of Comets: A First Application to C/2007 N3 (Lulin). *AJ*, 141, 12–+

- ROBERTSON, I. P., SEMBAY, S., STUBBS, T. J., KUNTZ, K. D., COLLIER, M. R. ET AL. (2009). Solar wind charge exchange observed through the lunar exosphere. *Geophys. Res. Lett.*, 36, 21102–+

- PORTER, F. S., ABBEY, T. F., BANNISTER, N. P., CARTER, J. A., COLLIER, M. ET AL. (2008). The Lunar X-ray Observatory (LXO). In Proceedings of the SPIE Conference Series, vol. 7011

# Contents

# List of Figures

# List of Tables

Chapter 1

# Introduction

High-energy, X-ray astronomy requires observations be taken from outside the constraints of the Earth's atmosphere, which is opaque to this wavelength regime. There are now an unprecedented number of X-ray observatories in orbit about the Earth, including the European-led mission XMM-*Newton*. Each of these observatories is sensitive to varying levels of 'background'; some level of signal that contributes an unwanted component to the data intended to be collected. This background must be carefully categorised, decomposed into its various constituents and understood to be correctly eliminated and to allow proper consideration of the remaining scientific data of interest. In contrast possibly to the majority of users of a particular observatory, the background signal may in itself be of scientific interest to a section of the community. The precise level of background experienced by the science instrumentation will depend on the structure of the satellite in question, its orbit and the local environmental conditions about the spacecraft at the time of observation.

What constitutes the background will depend on the object or region of interest. The removal of a background component is a particularly acute problem for the study of diffuse emission as observed by an imaging instrument, as compared to the procedures used during the analysis

of point sources. The diffuse emission of interest may completely fill the field of view of the imager, and therefore it may be difficult to eliminate any background component via comparison of on-source to off-source regions. In contrast, for a point source embedded in a region of diffuse emission, the background is dominated by this emission in which it is surrounded. In studies of diffuse and extended regions, for example within the Galaxy or of unresolved extragalactic sources, the 'background' itself is of scientific interest. However, in studies of both point sources and diffuse emission, background components that are purely instrumental in origin must be discarded.

One source of background is that of terrestrial charge exchange X-ray emission. This emission results from the interaction of highly charged ions in the solar wind with neutral atoms in the vicinity of the Earth. Charge exchange emission may be considered a contaminant by the majority of those XMM-*Newton* users whose main scientific interest is extra-Solar System astrophysics. However, in its own right, the study of charge exchange can provide useful information regarding the solar-terrestial connection and solar wind constituents that may be inferred from its signal. This thesis considers in detail this particular component to the X-ray background, with regards to the XMM-*Newton* observatory and the analysis of data obtained via its imaging cameras.

## 1.1 The XMM-Newton observatory

XMM-*Newton* (Jansen et al., 2001) is a European Space Agency (ESA) Horizon 2000 Science Programme mission, that includes imaging and high-spectral resolution X-ray instrumentation along with a supporting optical monitor. The imaging suite of cameras known collectively as the European Photon Imaging Camera (EPIC), comprises two MOS (Turner et al., 2001) and one pn (Strüder et al., 2001) charged coupled device (CCD) cameras positioned at the foci of the three telescopes. The observatory was launched on 10$^{th}$ December

1999 and has been operating in scientific operational mode since July 2000. Due to its large effective area (approximately 2000 $cm^2$ at 1 keV for the combined EPIC cameras) and wide field of view (30 arcminutes diameter), XMM-*Newton* provides unprecedented detailed studies of galaxies, SNRs, clusters and other extended and diffuse sources. Approximately 30% of its observations are of diffuse and extended sources.

In more detail, the observatory consists of three telescopes which each consist of 58 grazing-incidence Wolter-I nested mirrors, with a focal length of 7.5 m. Each mirror consists of a paraboloid and an associated hyperboloid surface to focus incident X-rays. The mirrors were manufactured by electro-coating a nickel substrate with gold. Each telescope contains an electron deflector, producing a small magnetic field to prevent low-energy electrons from reaching the focal plane and a stray-light baffle to prevent light from outside the field-of-view undergoing single reflections in the mirror module and reaching the detector. Additional components to the observatory include star trackers, an optical monitor and instrument radiators. A schematic of the telescope is shown in Figure 1.1. The two high-spectral resolution Reflection Grating Spectrometers (RGS) are found behind two of the telescopes which divert about half of the light entering the telescope. The remaining light is directed to the EPIC-MOS instruments. The EPIC-pn (or simply pn) camera is found behind the third telescope. Each of the EPIC CCD-cameras is accompanied by a stand-off structure consisting of a filter wheel, door, calibration source, internal vacuum bulkhead and radiation shielding. The CCDs must be cooled and the temperature is controlled by a cryostat. This is achieved by radiating passively to deep space. The filter wheel can be rotated to select the optical and UV blocking filter required. The filter wheel options are thin (1600 Å polyimide film with 400 Å aluminium), medium (1600 Å polyimide film with 800 Å aluminium) or thick (3300 Å polypropylene with 1100 Å aluminium and 450 Å tin) for normal science operations, or the wheel can be placed in the closed position. In addition, a $^{55}$Fe radioactive calibration source can be used to illuminate the detectors. The closed and cal-closed (when both the door is closed and the radioactive calibration source is in use) positions are important for background

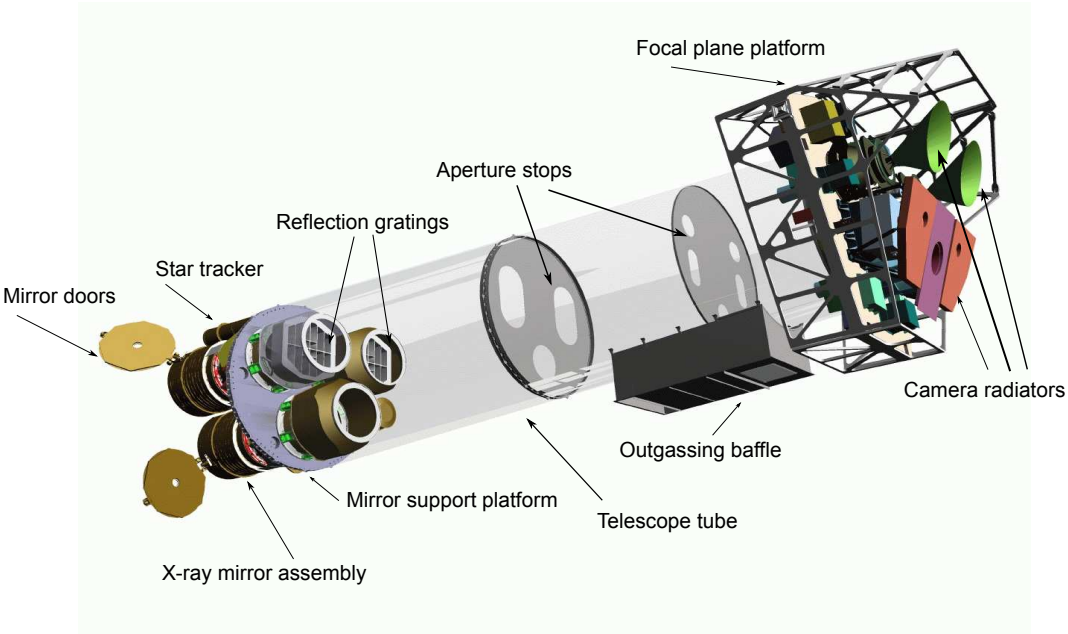


**Figure 1.1:** Schematic, transparent view of XMM-*Newton*. Credit: Jansen et al. (2001).

and calibration studies, which are explored later in Chapter 2. The telescope achieves an angular resolution of 6 arcseconds (FWHM) and the EPIC-cameras have an energy resolution of $\frac{E}{\Delta E} \sim 20$ at 1 keV.

XMM-*Newton* orbits the Earth following a highly elongated elliptical path. The orbit is discussed in more detail in Section 3.5, however it has a duration of ∼48 hours, including approximately 6 hours of non-science operational time as the satellite passes through the radiation belts.

The EPIC-MOS (metal oxide semi-conductor) cameras consist of seven front-illuminated charge-coupled devices (CCDs, manufactured by e2v[1], type 22 CCD) in a staggered arrangement so that the central CCD (CCD 1) is at the focal point of the optical axis. The other CCDs are offset from the central CCD towards the mirror module by 4.5 mm. Each CCD comprises 600×600 40 $\mu$m square pixels (equivalent to 1.1×1.1 arcseconds). The camera is sensitive, for scientific operations, in the range 0.2 to 10 keV. Due to a micro-meteor event, CCD 6 of

[1] http://www.e2v.com

MOS1 has been non-operational since revolution 961. The pn camera consists of 12 individual back-illuminated CCDs arranged in quadrants. Each CCD comprises $64\times200$ 150 $\mu$m square pixels (equivalent to $4.1\times4.1$ arcseconds). The camera is sensitive in the range 0.2 to 15 keV. The detector layouts and name of each chip are presented for each EPIC camera in Figure 1.2.

X-ray sensitive CCDs function by the absorption of an X-ray photon in the silicon layer which may result in the ejection of a free photo-electron (for example as reviewed in Howell 2006). This electron moves through the silicon lattice, producing a trail of electron-hole (an electron vacancy) pairs along its path. The number of electron-hole pairs produced is a function of the incident energy of the X-ray photon. The photon could theoretically transfer all its kinetic energy ($E$) to the liberation of electrons throughout the lattice (an average of 3.6 eV is required per electron, parameter $w$), but in practice this is not the case. Divergence from this outcome is termed the *Fano factor* ($F$). This can be described as a deviation away from a purely Poissonian process in the release of the electrons as each electron-hole creation event is not mutually independent (Fraser, 1989). The energy resolution of the detector is determined by the variance in the number of electrons released ($E/w$) reduced by the factor $F$. The resulting electrons that are released drift towards the nearest anode of the device, under the applied electric field. They may then be counted to approximate the energy of the incident photon and an image (in the case of the EPIC cameras) and spectrum may be built up as successively more photons are absorbed.

The EPIC cameras can operate in timing or imaging modes. The imaging modes are further subdivided into the partial window modes (small or large), full-frame mode, and in the case of the pn, extended full-frame mode. Both the MOS and pn cameras can operate in timing mode for improved timing resolution (1.75 ms and 0.03 ms respectively), when imaging is reduced to only one CCD dimension. The pn has an additional burst mode with very high time resolution (7 $\mu$s). Observations of faint, diffuse and extended sources are normally taken

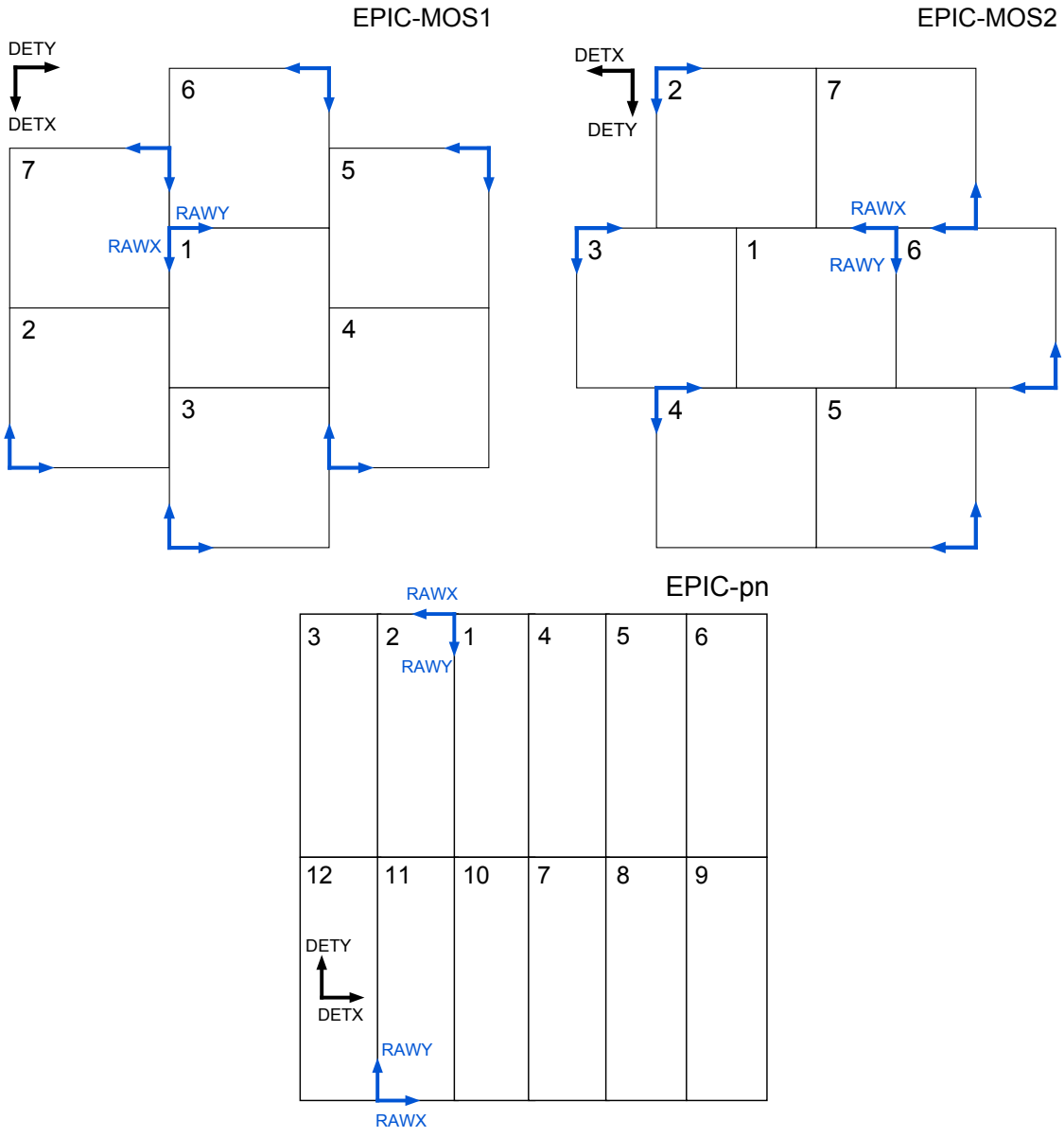


**Figure 1.2:** Detector plane layouts for (top left, top right, bottom) the EPIC MOS1, MOS2 and pn detectors on board XMM-*Newton*, with each chip number labelled. The direction of the detector and raw coordinate (for each CCD) systems are noted. CCD 6 of MOS1 has been turned off since revolution 961.

**Table 1.1:** XMM-*Newton* EPIC instruments and imaging modes. We note the number of pixels used in each case (in the X and Y directions) for the central CCD for the MOS cameras and over the whole camera for the pn. The small window mode of the pn only uses CCD 4. Frame time and the percentage of the frame time required for readout are also given.

| Instrument | Mode | Pixels | Frame time (ms) | Read out time % |
|---|---|---|---|---|
| EPIC-pn | Small window | 63×64 | 5.7 | 29.0 |
| EPIC-pn | Large window | 198×384 | 47.7 | 5.1 |
| EPIC-pn | Full-frame | 376×384 | 73.4 | 0.1 |
| EPIC-pn | Extended full-frame | 376×384 | 199.1 | ∼0 |
| EPIC-MOS1 | Small window | 100×100 | 300 | 2.5 |
| EPIC-MOS1 | Large window | 300×300 | 900 | 0.5 |
| EPIC-MOS1 | Full-frame | 600×600 | 2600 | ∼0 |
| EPIC-MOS2 | Small window | 100×100 | 300 | 2.5 |
| EPIC-MOS2 | Large window | 300×300 | 900 | 0.5 |
| EPIC-MOS2 | Full-frame | 600×600 | 2600 | ∼0 |

in the full or extended full-frame modes. Details of the imaging modes available to the EPIC instruments and the frame time for each are given in Table 1.1.

Observations may be stopped at any time if thresholds are breached by the on-board radiation monitor. The scientific instruments are put into a safe-mode (with the filter wheel in the closed position) to avoid damage until acceptable levels of radiation are recorded. The radiation monitor consists of two silicon diode detectors: one to register the incidence of low energy protons and electrons and the other for higher energy particles. The low energy detector records electrons with energies greater than 130 keV and protons over 1 MeV. The high energy detector records electrons with energies greater than 0.5 MeV and protons over 8 MeV.

XMM-*Newton* is controlled through real-time interactions through data links from ground stations at Perth, Australia and Kourou, French Guiana with back-up stations located at the European Space Astronomy Centre (ESAC), Spain and Santiago, Chile. Mission operations, flight dynamics and some software support are provided by teams at the XMM-Newton mission operation centre (MOC) at ESA's Space Operation Centre, Germany. Data downloaded

from the satellite passes through the MOC to the science operations centre (SOC), also at ESAC, where other software, mission and user support teams are located. Calibration and scientific data analysis procedures are developed at ESAC and those institutions (such as the University of Leicester) that were involved with the construction of the spacecraft and its science payload.

## 1.2 The XMM-Newton background working group and motivation

In 2004 the XMM-*Newton* EPIC Background Working Group (BGWG) was established, following from a request by the XMM-*Newton* User Group, to investigate background issues for the EPIC cameras. This investigation includes the characterisation of the sky background from X-ray photons along with the particle-induced background and electronic noise. Information gathered by the group is disclosed via its public web site [2], available through the XMM-*Newton* Science Operations Centre.

This thesis results from work initiated by the BGWG, led by the motivation to characterise and quantify the incidence and level of charge-exchange produced X-ray emission contamination in XMM-*Newton* data, and forms the main aim of this thesis. We concentrate on the identification of XMM-*Newton* observations that have been affected when this particular component of the background is time variable. We shall show that X-ray emission from charge exchange emission imparts useful information regarding the composition of the solar wind and may be used in the future to image large areas of the Earth's magnetosheath with the end to understanding in greater detail the complicated relationship between the solar wind and the Earth.

[2] http://xmm2.esac.esa.int/external/xmm_sw_cal/background/index.shtml

## 1.3 Thesis outline

This thesis is laid out as follows. In Chapter 2 we describe the various background components, both sky and instrumental, of XMM-*Newton*. In Chapter 3 we introduce the charge exchange process and present an overview of solar-wind charge-exchange induced X-ray emission within the Solar System, concentrating on the interaction of the solar wind with the terrestrial system. In Chapter 4 we present the method used to identify cases of Earth-exospheric time-variable charge exchange as seen by XMM-*Newton* and we summarise the overall results of this procedure in this chapter and in Chapter 5. We apply a spectral model to each of the charge-exchange affected XMM-*Newton* observations identified in Chapter 6. One particular incidence of charge exchange emission seen in data from XMM-*Newton* that required more detailed attention is discussed in Chapter 7. In Chapter 8 we present a model to estimate the expected time-variable component of charge exchange X-ray emission for an XMM-*Newton* observation. We discuss how exospheric charge-exchange emission could be exploited in studies of the solar-terrestrial relationship through novel technology in Chapter 9. A discussion and outlook are given in Chapter 10.

Chapter 2

# The XMM-Newton EPIC background

The XMM-*Newton* EPIC background can be separated into particle, photon and electronic noise components (as described in the work of Lumb et al. 2002 and Read & Ponman 2003, and references therein). Several contributions are focused by the mirrors, whereas others arrive at the detectors directly even through the shielding. The particle background can be further sub-divided into contributions from soft protons and cosmic-ray induced events, and the photon background can be sub-divided into contributions from hard and soft X-rays. There may be other, more minor contributions to the background and the contributions mentioned here do not form a completely comprehensive list. However, each of the major components to the background is described in this chapter by discussing their temporal, spectral and spatial properties.

## 2.1 Particle background

The particle background consists primarily of focused soft protons and unfocused cosmic ray induced events.

### 2.1.1 Soft protons

This contribution to the background originates from solar soft protons, accelerated by magnetospheric reconnection events and trapped by the Earth's magnetosphere, which are then gathered by XMM-*Newton*'s grazing mirrors. They dominate times of high background. These soft protons can occur in flares up to ten times the quiescent level in an observation. They are highly unpredictable and affect 30% to 40% of XMM-*Newton* observation time. The frequency and intensity of soft proton flares increases closer to perigee. Within a single observation, a significant component may survive after good time interval screening to remove periods of flaring from a data set (De Luca & Molendi 2004, and described in more detail in Chapter 4). Spectrally the soft protons are variable in intensity and shape. They produce a wide-band, whole field-of-view (FOV) signal that can dominate the recorded signal throughout an observation. For energies $>0.5$ keV the continuum spectrum, which shows no lines, can be fitted by an unfolded XSPEC[1] power law, i.e. one not convolved with the instrumental response (specifically a double-exponential or broken power law, with the break energy at approximately 3.2 keV, and with the spectrum becoming flatter at higher intensities). Below 0.5 keV, much less flux is seen (Kuntz & Snowden, 2008). The soft protons are distributed over the detector in a similar manner to X-rays, but the vignetting function (the change in effective area of the telescopes as a function of off-axis angle) is flatter than for photons. In addition, the vignetting function for low-energy protons is flatter than that of high-energy protons. They are generally only observed inside the FOV, unless the solar flare is particularly intense, when some fraction can be scattered into the out-FOV region. There is no other spatial structure seen in the pn, but some structure may occur in the MOS cameras due to the presence of the Reflection Grating Array on board XMM-*Newton*. In Figure 2.1 we show a MOS1 and a pn image in detector coordinates from an observation (identifier 0008020101) that has been severely contaminated by soft protons. We also show a MOS1

[1] http://heasarc.gsfc.nasa.gov/docs/xanadu/xspec/index.html

and a pn image in detector coordinates from an observation (identifier 0112680801) that is scarcely affected by soft protons. The in-FOV area is much more pronounced in the soft-proton affected pair of images than the images without this contamination. All images were created from events using a flag selection (FLAG&0X766A0F63)==0, and with the pattern selection (PATTERN<=12) or (PATTERN<=4) for MOS1 and pn respectively. In addition we show a high-energy lightcurve from the same observation, showing considerable soft-proton flaring throughout and a large flare in the second half of the observing period. The lightcurve has been constructed from the observation *background time-series* product from the XMM-*Newton* 2XMM catalogue (Watson et al., 2009), using events above 14 keV. XMM-*Newton* data sets can be cleaned for soft protons by employing *good-time-interval* filtering to identify periods of flaring that can then be removed. Methodology for flare-filtering by good-time-intervals is discussed in more detail in Chapter 4.

### 2.1.2 Internal cosmic ray induced events: the instrumental background

This component of the background results from high-energy particles producing charge directly in the CCDs, and from the interaction of high energy particles with the detector, causing associated instrumental fluorescence. Within an observation this component can vary by up to 10%. For MOS the shape of the continuum above 2 keV is reasonably stable, but below 1.5 keV this can vary, possibly due to the redistribution of the Al calibration line (De Luca & Molendi, 2004). From observation to observation there is some variation; up to 10 times more intense an effect can be seen during periods of intense solar flares, but no increase is seen after the occurrence of solar flares so activation is unlikely.

The continuum spectrum is flat (with an photon index of $\sim$0.2). The major instrumental fluorescence lines for MOS are found at 1.5 keV (Al-K), 1.7 keV (Si-K), plus some contribution from high energy lines (Cr, Mn, Fe-K and Au). For the pn, Al-K is seen at 1.5 keV, whereas

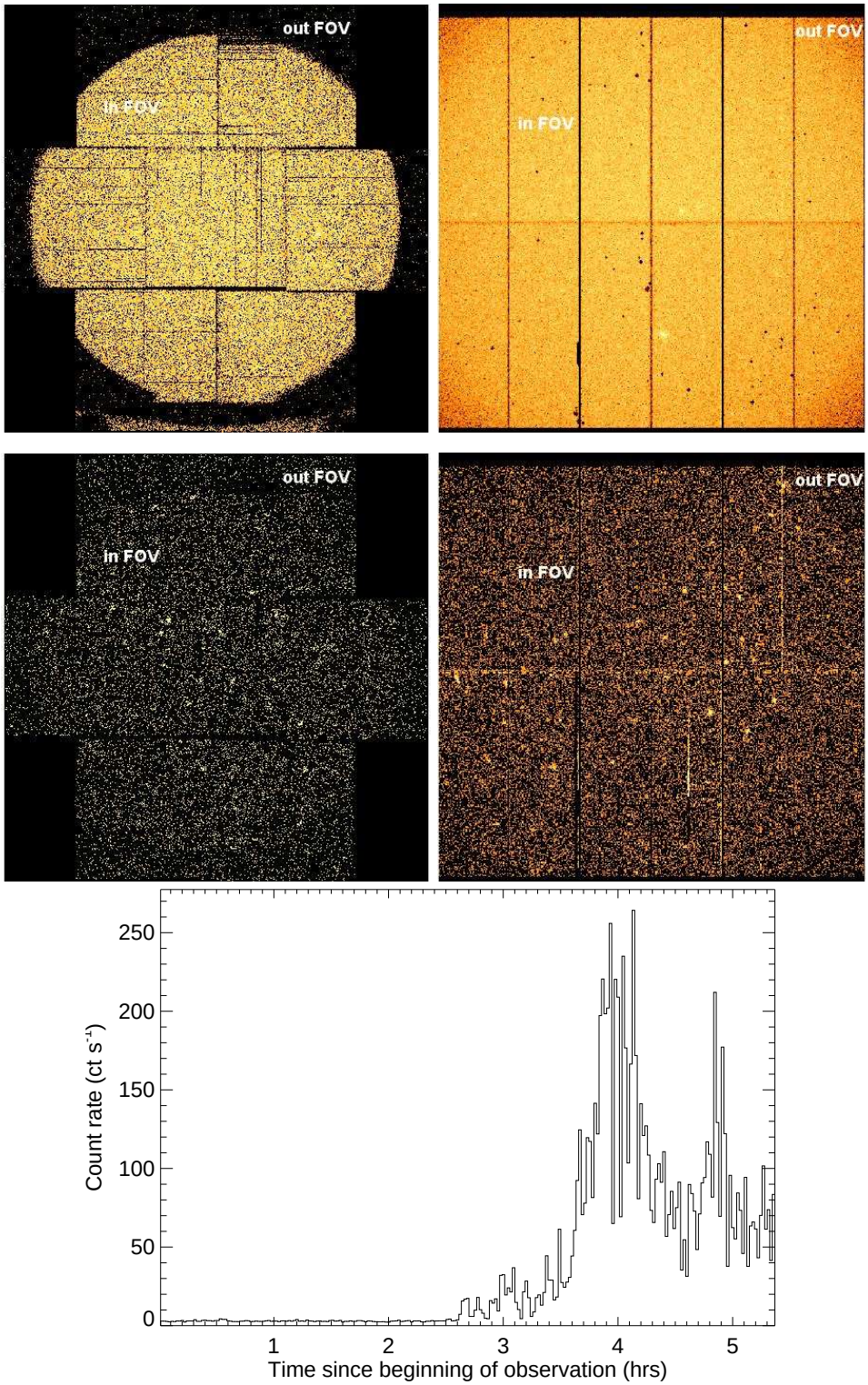


**Figure 2.1:** Top row, from left: a MOS1 then a pn image from an observation during which severe levels of soft-proton contamination have occurred. Middle row, from left: similar images for MOS1 and pn from an observation during which the particle background was low. The in-FOV and out-FOV regions have been labelled for all images. Bottom panel: a high-energy lightcurve from this observation (pn) showing a very large flare towards the latter half. Time periods after $\sim$2.6 hrs would be rejected via good-time-interval filtering methods.

the silicon line is self-absorbed, and high energy contributions are seen from Cu, Ni, Zn and Ti. Detector noise occurs below 0.3 keV and is discussed in Section 2.1.3. A pn and a MOS1 particle-induced background spectrum are shown in Figure 2.2.

The internal instrumental background has a spatial distribution different from that of X-ray photons as it is not vignetted. In the outer CCDs for MOS there is more Al, whereas the CCD edges show enhanced Si. There are continuum differences between the out-FOV and in-FOV below the Al-line, possibly resulting from redistribution, as previously mentioned. There is more Au seen out-FOV due to the Al-shielding which is coated with gold on its inner surfaces. Energies and widths of the lines appear to be stable (little or no corrections to the instrumental gain are required), whereas line intensities can vary. In the pn, line intensities show large spatial variation from the electronics board, for example the 'copper hole', where a deficit in high-energy instrumental lines is seen at the detector centre (Freyberg et al., 2004). Residual low-energy instrumental background components are seen near the CMOS Amplifier and Multiplexing Chip (CAMEX) readout areas. Examples of the spatial distribution of these background components are shown in Figure 2.3.

The BGWG provides individual and combined data sets from observations taken when the filter wheel was in the closed position (filter wheel closed, FWC), i.e. that do not contain a photon contribution. These files are extremely useful for performing background analysis, given the spatial and spectral distributions of the particle-induced background as described above.

The overall level of the particle-induced background has changed throughout the XMM-Newton mission. In Figure 2.4 we show a lightcurve, created using pn combined FWC event files. Enhanced numbers of cosmic rays can reach inner regions of the Solar System during periods of solar minimum and this is the primary cause of the slow and steady ramp-up of the particle-induced count rate throughout the length of the mission. In addition, FWC obser-

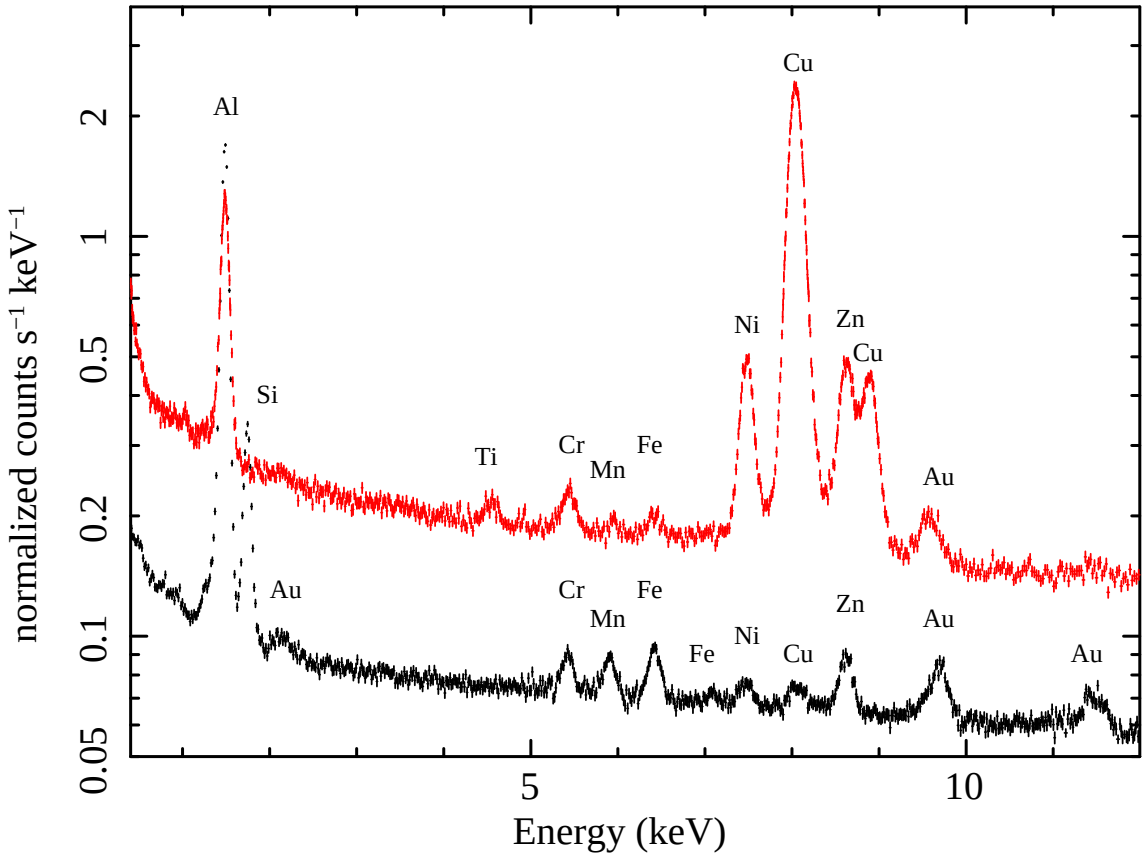


**Figure 2.2:** MOS1 (black) and pn (red) particle-induced background spectra. Major fluorescence lines have been labelled.

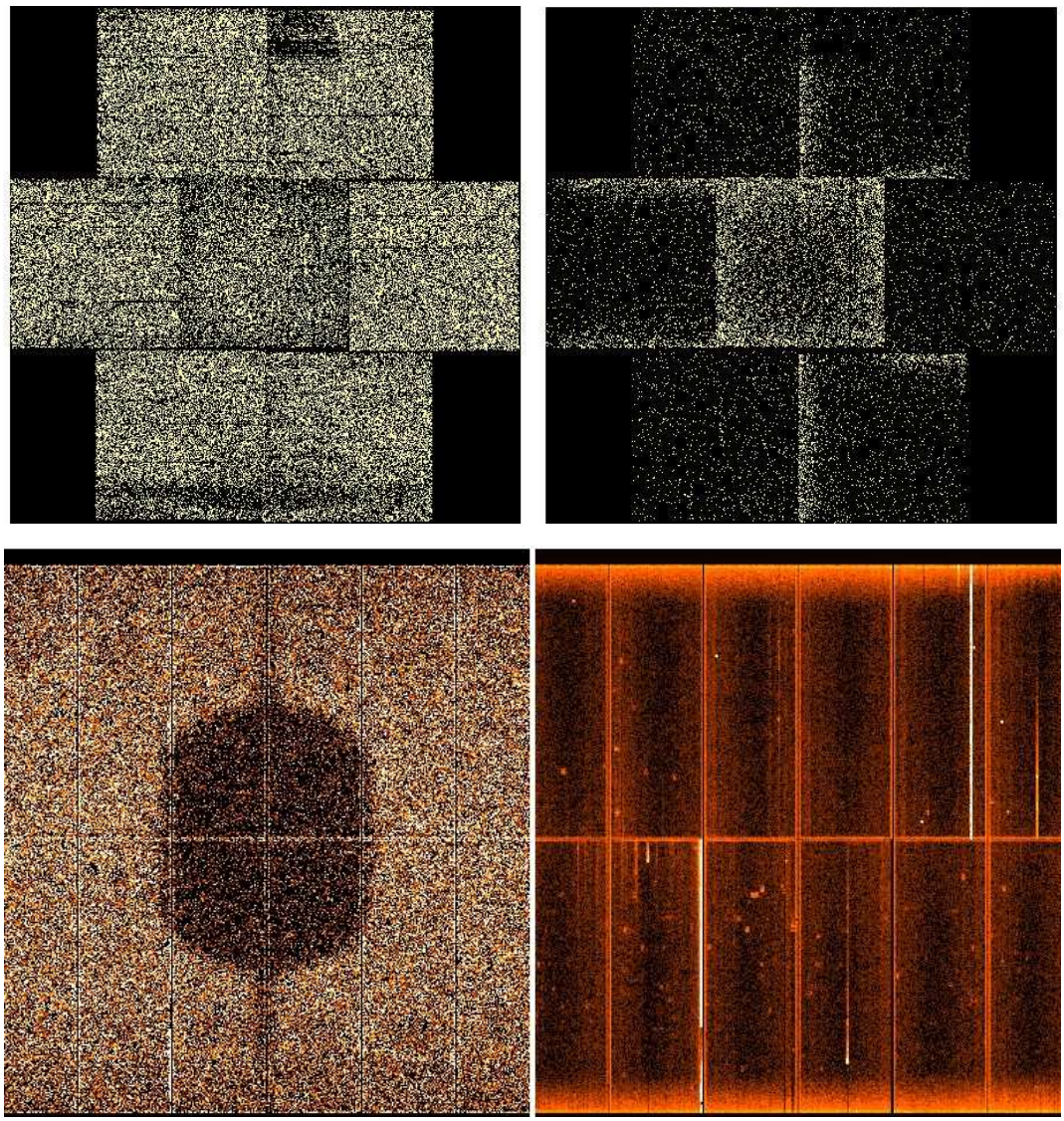

**Figure 2.3:** Example images of the spatial distribution of the particle-induced background. Left upper panel: MOS1 Al distribution, in the energy band 1.45 to 1.55 keV. Right upper panel: MOS1 Si distribution, in the energy band 1.70 to 1.80 keV. Left lower panel: pn Cu distribution, in the energy band 7.8 to 9.1 keV. Right lower panel: pn CAMEX noise along with bad pixels and bright columns, in the energy band 0.2 to 0.5 keV.

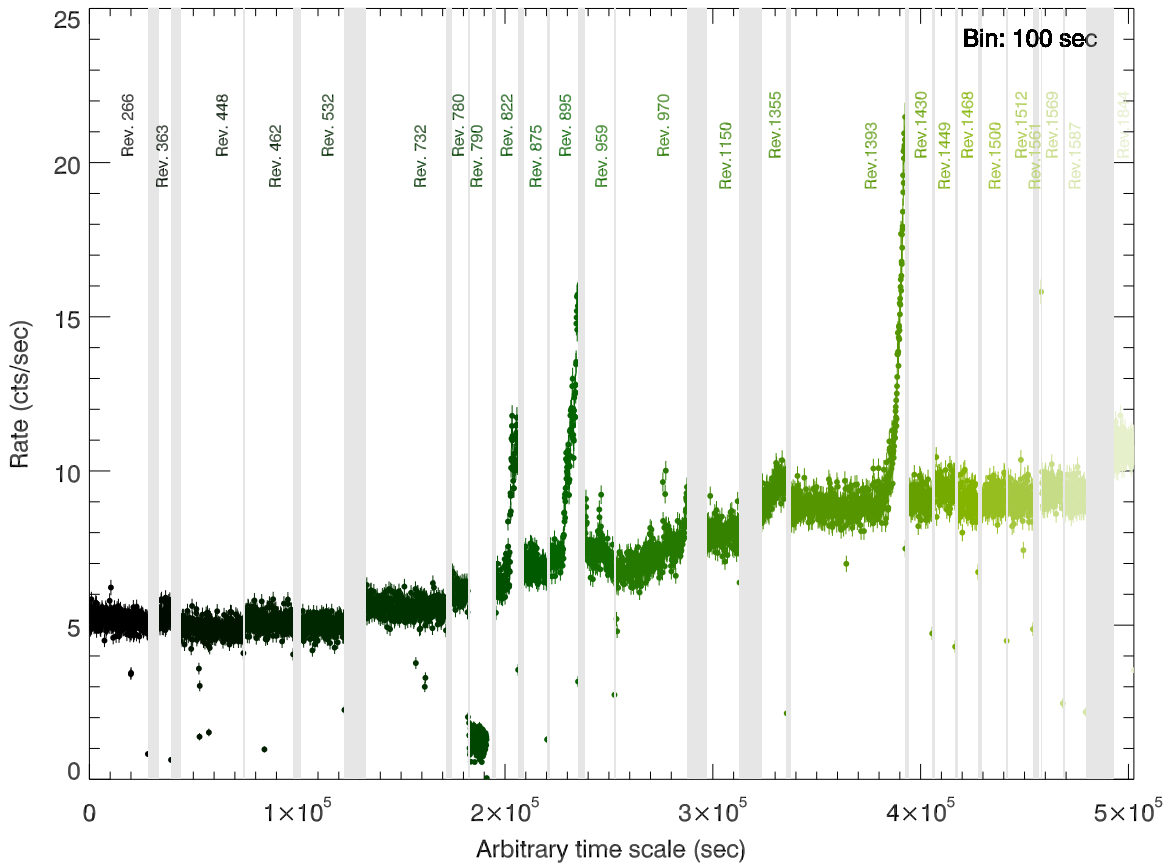


**Figure 2.4:** Particle-induced pn background lightcurve throughout the XMM-*Newton* mission. The revolutions when the count rates were calculated are noted on the figure. Note that the observations are typically a few months apart. Credit: XMM-*Newton* Science Operations Centre, ESA.

vations are often performed immediately prior to or after perigee passage of XMM-*Newton*, when the instruments are placed in a safe mode to protect them from radiation damage when passing through the radiation belts. This, along with extremely large flares, may be the cause of the sharper flares seen in the lightcurve.

### 2.1.3 Electronic noise

Electronic noise results from bright pixels and parts of columns, CAMEX readout noise in the pn and artificial low-energy enhancements in the outer CCDs of MOS (e.g. Figure 2.3, lower right panel). Dark current may also contribute, but this is thought to be negligible.

Persistent noise occurs from thermal processes in each CCD pixel which creates events with sufficient charge to appear above the detector threshold. This electronic noise component is essentially fixed. No temporal variations in rate are seen within an observation apart from the bright pixel and column component that can vary by up to 10%. Bright pixels, primarily due to pixels damaged by radiation, fluctuate greatly between observations. Pixels so bright that they can cause the event rate to exceed the instrument telemetry limit are blocked on board.

For the pn, the CAMEX readout noise is mode dependent; extended-full-frame mode suffering the least from this noise, and small window mode the most. Artificial low-energy enhancements may affect up to 20% or more of observations, and are enhanced during periods of high background rate. Spectrally, this component is seen at low energies (below 300 eV) for the bright pixel and CAMEX readout contributions. The bright pixels and columns are seen at certain locations; CAMEX structure is seen near to the pn readout.

Certain MOS CCDs show some peculiarities in and out of the FOV (Kuntz & Snowden, 2008; Pradas & Kerp, 2005) and spatial inhomogeneities are seen within a single MOS CCD. An as yet poorly understood feature is seen in various MOS CCDs at low energies (Kuntz & Snowden, 2008). Occurrences of this sort are known as the ‘anomalous state’ for the MOS CCD affected. Severely affected CCDs are MOS1-CCD 2, 4, and 5 and MOS2-CCD 4 and 5. Spectra taken from these CCDs during an anomalous state exhibit an almost flat enhancement below $\sim$1 keV. The cause of this feature is currently under investigation by the instrument teams and BGWG.

## 2.2 Photon background

The photon background can be split into components from hard and soft X-rays and these components are focused by the mirrors.

### 2.2.1 Hard X-ray photons

The hard X-ray background photons mainly originate from unresolved active galactic nuclei (AGN) within the FOV. There are also single reflections into the FOV from all kinds of out-FOV sources, both bright and faint, resolved and unresolved (the unresolved out-FOV sources being, as for the in-FOV, predominately AGN). Out-of-time events (OOT) are also a contributor to the hard X-ray background of the pn, and to a lesser extent the MOS. OOTs are smeared along the readout direction from bright sources of X-rays (Freyberg et al., 2004). The hard X-ray photon background does not vary within an observation or between observations in a given pointing direction, although OOTs are mode dependent for the pn; the full-frame mode experiencing more of this effect than both the extended-full-frame and large window mode, due to the percentage of the frame time used for readout.

The hard X-ray photon background can be modelled by a power law of spectral index $\sim$1.4. In times of low-background, and below 5 keV, this component dominates over the internal instrumental component of the background, whereas above 5 keV, the internal component dominates. As they are genuine X-ray photons, they are spatially vignetted.

Diffuse flux from single reflections gathered from out-of-field angles of 0.4-1.4 degrees that are reflected into the FOV ('single reflections'), contribute $\sim$7% of the in-FOV flux (Lumb et al., 2002), and the effective area of one of the telescopes is approximately 3 $cm^2$ at 20-80$'$ off-axis (de Chambure et al., 1999).

### 2.2.2 Soft X-ray photons

Soft X-rays originate from the Local Bubble, Galactic Disk, Galactic Halo, extragalactic sources and the Solar Wind Charge Exchange (Snowden et al. (2004) and discussed more fully in Chapter 3), single reflections from outside the FOV and OOT events. Solar Wind

Charge Exchange is an interaction between the highly ionised solar wind and either interstellar neutrals in the heliosphere or materials in the Earth's exosphere. There is little variation seen in the soft X-ray background during a single observation, although long observations may be affected by charge exchange. Variations of up to 35% are seen between observations as observation pointings differ in Right Ascension and Declination. The charge exchange component may effect observations differently and is the main subject of this thesis.

The diffuse contributions from the Local Bubble, Galactic Disk and Galactic Halo have a thermal component with emission lines $\lesssim$1 keV. The extragalactic component above 0.8 keV has an index of 1.4, whereas the galactic contribution in terms of emission and absorption varies. The charge exchange component is very soft and the Snowden et al. (2004) work suggested that it comprises unusual O VIII/O VII line ratios and strong O VIII and Mg XI features.

The soft X-ray background component is vignetted as it is made up of genuine X-ray photons. Spatially, the only structure seen is from real astronomical objects, and the extragalactic component above 0.8 keV is spatially uniform. Charge exchange emission is seen over the whole FOV. The single reflections and OOT events behave as those resulting from hard X-rays.

## 2.3 Summary

We have summarised the XMM-*Newton* background in terms of its components as categorised by the XMM-Newton EPIC BGWG.

The background has shown itself to be extremely complicated and made up of various photon, particle-induced and electronic components. When performing detailed XMM-*Newton* EPIC

analysis, a good knowledge of the background is required. Sometimes it may be possible to extract the background from a region close to the particular source one is interested in (using a so-called 'local' background). For a large or extended source however, one may have to extract the background far from the target source (the source may in fact be so extended that no local background is visible within the FOV). Here, a number of effects, due to many of the features described above, can cause the extracted local (off-axis) background to be highly inappropriate in analysing the (normally on-axis located) target source, such as changes in the effective area of the mirrors with off-axis angle, instrumental fluorescence and the spectral response which can depend on the position on the detector (these off-axis effects are corrected in the XMM-*Newton* EPIC calibration). Hence careful consideration of the background is required when analysing diffuse and extended emission.

The remainder of this thesis concentrates on just one of the background components, that of SWCX emission due to the interaction of solar wind ions with neutrals found in the vicinity of the Earth. The next chapter provides an introduction to the charge exchange physical process and descriptions of the interacting components, i.e. the solar wind and neutral atoms in near-Earth interplanetary space. We also aim to put the study of charge exchange emission in the Solar System in context, with reference to the literature and current understanding.

Chapter 3

# Solar wind charge exchange in the Solar System

This chapter contains a description of the charge exchange process and a discussion of charge exchange in terms of the emission of X-rays. We consider various sites of charge exchange X-ray emission within the Solar System. We examine the possible implications of this emission for X-ray observatories, in particular XMM-*Newton*.

## 3.1 Charge exchange emission

In contrast to most other physical processes that result in the emission of X-rays, charge exchange does not require interactions involving hot electrons. The charge exchange process involves the transfer of one or more electrons from an atom or molecule (the donor) to an ion (the projectile). The electron is received by the ion into an excited state with a high energy level $n$ (principal quantum number). In the subsequent relaxation of the ion a photon is emitted. If the initial charge state of the projectile ion was sufficiently high, the emitted

photon can have an energy in the X-ray regime. The basic process of charge exchange and the relaxation of the ion in the excited state are given in Equations 3.1 and 3.2.

$$A^{q+} + B \rightarrow A^{(q-1)^{+*}} + B^{+} \tag{3.1}$$

$$A^{(q-1)^{+*}} \rightarrow A^{(q-1)^{+}} + h\nu \tag{3.2}$$

Where $A$ is the projectile ion and $B$ the target donor atom or molecule.

Cross-sections for charge exchange electron transfers are very high compared to that of electron impact (or direct) excitation (for example $\sim 10^{-14}\,\mathrm{cm}^2$ as compared to $\sim 10^{-20}\,\mathrm{cm}^2$ for NeX Ly-$\alpha$ at approximately 1.02 keV, Wargelin et al. 2008). Although multiple electron capture can occur if the donor species has more than one electron, we consider only single electron capture here as this is more appropriate in the case of terrestial charge exchange (see the discussion below).

Various theoretical models have been proposed to describe charge exchange and we discuss one such model here. The Classical Over the Barrier model (COB, Ryufuku et al. 1980; Mann et al. 1981) is the most simple and is appropriate for collisions energies between 100 eV/amu and 10 keV/amu and we consider this in terms of single electron capture below.

As the projectile ion approaches the donor, the energy levels of both are distorted (Stark shift). At a certain distance, an electron from the donor can transfer to the ion in the joint potential well of the quasi-molecular state; at the so called 'curve crossing'. This occurs when the height of the potential well is lower than that of the electron's binding energy. Curve crossings can occur at several internuclear distances and so the electron can be captured into several different energy levels (Wargelin et al., 2008). However, highly charged incoming ions overlap their energy levels at a high energy and receive a donor electron into a corre-

spondingly high-$n$ energy level. The electron will radiatively decay either through a cascade or directly to the ground state, resulting in the emission of a high-energy (X-ray) photon.

A step-by-step analysis of the charge exchange process can be explained by considering an electron of the donor atom undergoing the following steps (from Bodewits 2007, assuming the use of the atomic unit system so that the charge and mass of the electron along with the Coulomb constant are set to 1):

- at infinite separation, the electron of the donor atom has a (negative) binding energy $I_b$.
- as the ion approaches the donor atom, the binding energy of the electron in the donor atom is increased by a Stark shift:

$$I_b(R) = I_b(\infty) - \frac{q}{R} \tag{3.3}$$

  where $R$ is the separation between the ion and the donor atom and $q$ the charge of the incoming ion.

- the electron experiences a total potential energy $V$ (which is the sum of the potential of the ion and the potential of the donor):

$$V(r) = -\frac{q}{|R-r|} - \frac{1}{r} \text{ , for } 0 < |r| < |R| \tag{3.4}$$

  where $r$ the distance of the electron from the nucleus of the donor atom

- at a certain distance $r_{max}$, the top of the potential barrier between the ion and donor is reached and the differential of the potential $V(r)$ is zero:

$$r_{max} = \frac{R}{\sqrt{q}+1} \tag{3.5}$$

- at $r_{max}$, we find potential $V_{max}$:

$$V_{max} = -\frac{(\sqrt{q}+1)^2}{R} \tag{3.6}$$

- the electron can transfer from the donor to the ion when the $V_{max}$ is smaller than the binding energy of the electron (Equation 3.3). This occurs at a distance $R_c$:

$$-\frac{(\sqrt{q}+1)^2}{R} = I_b(\infty) - \frac{q}{R} \tag{3.7}$$

$$R_c = \frac{2\sqrt{q}+1}{-I_b(\infty)} \tag{3.8}$$

- using $R_c$ we can find the cross-section of the charge exchange process:

$$\sigma = \pi R_c^2 \tag{3.9}$$

- this cross-section should be adjusted by the probability of the charge exchange process taking place, which is about 50% (the electron either stays with the donor or transfers to the ion).

- the electron is now bound to the ion. As the ion moves away from the donor, which is now charged, it induces a change in the potential of the electron by a Stark shift:

$$I_f = I_b + \frac{q-1}{R_c} \tag{3.10}$$

- the electron is now found at a higher binding energy, in a high-energy level of the ion (now with charge $q-1$). The energy level in which the electron is most likely to be found, if the donor atom is hydrogen, can be approximated by (Wargelin et al., 2008):

$$n_{max} \sim q^{3/4} \tag{3.11}$$

For fully-stripped $O^{8+}$ for example, in collision with hydrogen, the most likely energy level to be populated is $n = 5$, resulting in the hydrogen-like ion $O^{7+}$. For hydrogen-line ions the captured electron is likely to be in a *p* state, from which it can decay via cascades or directly to the 1*s* ground state releasing a photon, resulting in strong high-*n* energy level Lyman emission (Wargelin et al., 2008). In comparison, direct excitation results in a dominance of Lyman-$\alpha$ emission with less emission resulting from the higher-*n* states. Emission from helium-like ions, such as the incoming ion $O^{7+}$, leading after charge exchange to $O^{6+}$, is complicated by the need to consider the spins of the two electrons present in the resulting ion, which either results in a singlet (S = 0) or triplet (S = 1) state. The singlet state decay results, for example, in the strong resonance line (*w*, $1s^2\ ^1S_0 - 1s2p\ ^1P_1$). The triplet state is prevented by the spin selection rule ($\Delta S = 0$) from decaying directly to ground and so an electron must be passed through the $n = 2$ level. From this level the electron can decay via the forbidden line (*z*, $1s^2\ ^1S_0 - 1s2s\ ^3S_1$, fed from contributions from the $^3P_{0,1,2}$ states) or intercombination line transitions (*x*, *y*, $1s^2\ ^1S_0 - 1s2p\ ^3P_{1,2}$). For O VII, the branching ratios between the forbidden and intercombinations lines are 0.7:0.3 (calculated via theoretical transition rates and assumed population of the triplet state, $^3P$), so the forbidden line is by far the most prominent transition (Bodewits et al., 2007; Krasnopolsky et al., 2004).

The COB model described above is a simplified model of the charge exchange process that does not fully predict the populations of the *n* and *l* levels of the resulting ion (with charge $q-1$). Other more complex theoretical models, such as the Classical Trajectory Monte Carlo technique, Landau-Zener approximation or quantum-mechanical close-coupling method, aim to incorporate more detailed quantum characteristics into their calculations. Theoretical efforts are supported by laboratory studies, using a variety of high-resolution techniques to determine cross-sections for different ions and collision velocities. Outstanding discrepancies

between predicted and observed cross-sections may be due to the participation of multiple electrons and the classical assumptions taken by the models. Astrophysical X-ray sources such as comets have become recognised as important additional sites to observe and characterise the charge exchange process (Dennerl, 2010).

When the projectile ion originates in the solar wind, the charge exchange process is often referred to as solar wind charge exchange (SWCX). We use this acronym throughout this thesis. A SWCX spectrum is characterised by emission lines corresponding to the ion species present in the solar wind. Although the solar wind is approximately 99% protons, electrons and $\alpha$-particles, the remainder of the wind consists of heavier elements such as C, O, Mg, Si, Fe and Ni. The heavier elements found in the solar wind are often of high charge state due to the high temperatures of the solar corona. The relative abundances of the elements are dependent on the conditions of the Sun when the solar wind leaves the solar corona. We discuss the solar wind briefly in the next section.

## 3.2 The solar wind

The Sun continuously releases a million tonnes of plasma every second in the form of the solar wind. This collisionless plasma (with a mean free path of approximately 1 AU) consists primarily of electrons and protons with energies of 10 to 100 keV, although around 1% is provided by heavier elements. The speed of the solar wind can vary drastically, from approximately $250\,\mathrm{km\,s^{-1}}$ to $1000\,\mathrm{km\,s^{-1}}$. During times of solar minimum, slow solar wind originates from about 30° or less from the solar equator, whereas faster solar wind originates from coronal holes (areas of open field lines) in the polar regions. During periods of solar maximum however, this rough stratification is less well defined and the plasma is, in general, highly variable. Along with its speed, the composition of the solar wind can change and is dependent on the 'freeze-in' temperature of the plasma, reflecting the region in the solar

corona from where the wind originated. This freeze-in effect occurs when the solar wind draws out faster than it can equilibriate to the local electron temperature (Geiss et al., 1995). The slow solar wind has a higher temperature (with a freeze-in temperature of $\sim$1.7 MK for $O^{7+}$ to $O^{6+}$) than that of the fast solar wind (with a freeze-in temperature of $\sim$1.2 MK) and therefore generally contains ions with higher charge states. This situation is complicated by several phenomena. Coronal Mass Ejections (CMEs) for example are large, structured clouds of plasma that are released in solar storms with very fast velocities and distinctive compositional signatures. Co-rotating regions (CIRs) occur when faster moving streams of equatorial plasma in the slow solar wind catch up and subsequently pile-up against the slower moving ambient plasma. Both CMEs and CIRs have implications for space-based technology in orbit about the Earth which may be affected by the arrival of higher density plasma in their vicinity.

Although they make up a very small percentage of the solar wind plasma, minor ions (those heavier than $^4$He) carry information about the solar corona into interplanetary space (Bochsler, 2007, and references therein). The dominant oxygen species is $O^{6+}$. To create the higher charge states of minor ions electron collisions must occur and so compositional data can allude to electron temperatures within the solar corona. In addition, the heavy ions must be accelerated by coupling to lighter particles such as protons and electrons to overcome gravity and reach escape speeds to become assimilated in the solar wind. The acceleration of the minor ions and the heating mechanism within the solar corona is an important area of science and can only be touched upon briefly here. However, Feldman et al. (2005) note that elemental abundances can be used as tracers to locate the sources from which the slow and fast winds emerge.

When discussing solar-wind and coronal abundances it is commonplace to talk about the First Ionisation Potential (FIP) effect. This compares the abundance ratio of an element-to-oxygen in the solar wind to the corresponding element-to-oxygen ratio in the Solar System. Low-FIP elements (such as Al, Na or Mg) below the Lyman-$\alpha$ limit (10 eV) are enhanced

over typical solar-system abundances, whereas high-FIP elements (such as N, Ne or He) are depleted. This suggests that ions are separated before they are accelerated into the solar wind (Richardson & Cane, 2004). The Low-FIP enhancement is known as the FIP-plateau. Coronal hole solar wind (in general, the source of the fast solar wind at solar minimum) exhibits a less-marked FIP-plateau than a slow solar wind stream (Bochsler, 2007) and less low-FIP elements than the slow solar wind (Zurbuchen et al., 2002; Geiss et al., 1995). Although abundance data from many solar cycles is limited, no systematic variation in composition has been seen between successive cycles, for a particular solar wind type (Reisenfeld et al., 2007). Along with differences between the fast and slow wind compositional fractionation, transient events such as CMEs show marked abundance signatures that can be used to identify plasma of this type. The presence of highly charged iron, elevated oxygen states along with enhanced $\alpha$-to-proton ratios for example are indicators of CME plasma (Richardson & Cane, 2004; Zurbuchen & Richardson, 2006; Zhao et al., 2007). Other indicators such as a proton and electron temperature decrease or enhancements in the magnetic field strength are also used (see Table 1 of Zurbuchen & Richardson 2006).

As the solar wind streams away from the Sun, it drags with it and distorts the Sun's magnetic field, known as the interplanetary magnetic field (IMF). The solar wind flow is radial, but as the Sun rotates (about once every 24 days), the field lines dragged along with it are bent into a spiral form. This is known as the *Parker Spiral*, a schematic of which is shown in the left panel of Figure 3.1 (Parker, 1958). At 1 AU the solar wind has a density of about 10 particles $\mathrm{cm}^{-3}$. The flow of the solar wind continues to fill the entire heliosphere, out to the heliospheric boundary which separates the solar wind and interstellar plasmas.

## 3.3 The Earth's magnetosheath and exosphere

The Earth's rotation and fluid, ferrous interior generate a magnetic field ($B_Z \sim 31\,\mu$T at the equator) that can be approximately described by that resulting from a dipole placed at the Earth's centre. This dipole field is slightly misaligned from the spin axis of the planet by about 10°. Due to the so-called frozen-in assumption that the Sun's magnetic field is dragged out into the Solar System and is tied to the movement of the solar wind plasma, no mixing can occur between the plasma of the solar wind and that of the Earth (the magnetic field lines of the solar wind plasma cannot cross or intermingle with those of the Earth-based plasma, otherwise the conservation of magnetic flux, via Maxwell's equations, would be violated). As a result of the gradient between the two magnetic fields, and to a first approximation, a thin current sheet, known as the Chapman-Ferraro current is formed. The position of this boundary current sheet layer, called the magnetopause, is determined by the pressure balance between the two plasmas. The solar wind moves supersonically, unimpeded through the Solar System until it encounters an obstacle such as the Earth's magnetic field, whereby it is slowed down at the magnetopause boundary. A shock wave, known as the bow shock, is formed upstream, causing the slowing, heating and compressing of the solar wind plasma as it flows around the magnetopause. The region between the bow shock and magnetopause is termed the magnetosheath. The subsolar (or nose) region is defined as the dayside area of the magnetosheath approximately along the Earth-Sun line. Further downstream of the Earth the solar wind continues on its path unaffected and the resulting cavity of Earth-based plasma is known as the magnetosphere. The situation is complicated by the breakdown of the frozen-in approximation, leading to reconnection and the diffusion of the solar wind plasma into the Earth system, which manifests itself in phenomena such as the aurora borealis. However, this large scale description of the magnetosheath gives a sufficiently detailed picture for the work in this thesis. A schematic of the Earth system is shown in the right panel of Figure 3.1.

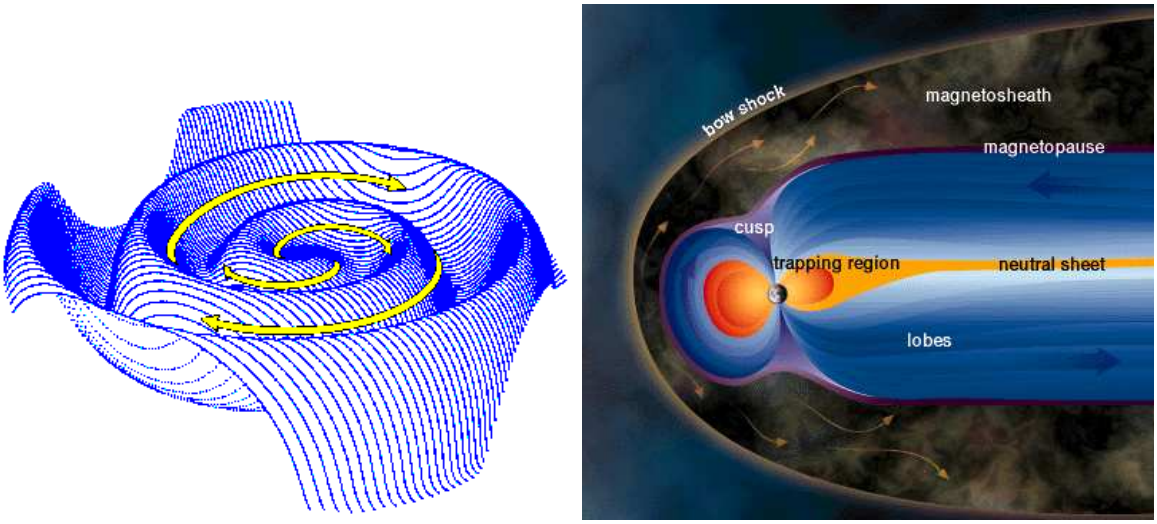


**Figure 3.1:** Left panel: the Parker spiral, credit: J. Jokipii, University of Arizona. Right panel: schematic of the Earth local environment, including the magnetosheath and bowshock, credit: Windows to the Universe, National Earth Science Teachers Association.

At an altitude of approximately 600 km ($\sim$0.1 Earth radii or $R_E$) the Earth's thermosphere (a layer of warm atmospheric gases which lies above other atmospheric layers defined by their temperature profiles) gives way to the exosphere, where hydrogen, still trapped in the gravitational potential well of the planet, travels on ballistic trajectories. The exosphere is the transition zone between the Earth and interplanetary space and the upper limit of this region occurs where solar radiation pressure overcomes the gravity of the Earth at approximately 30 $R_E$. We have described how Earth-based plasma is trapped in the Earth's magnetosphere due to the frozen-in approximation. Neutral atoms and molecules however are not limited by this restriction. Typical neutral hydrogen density values at 10 $R_E$ are 25 $cm^{-3}$ (Hodges, 1994). Østgaard et al. (2003) used measurements of the Lyman-$\alpha$ column brightness as measured by the Earth orbiting satellite IMAGE to produce models of the neutral density above 3.5 $R_E$, which we use for our modelling efforts in Chapter 8. These neutral hydrogen atoms in the Earth's exosphere become the donor atoms for SWCX occurring in the vicinity of the planet, which we describe in more detail in Section 3.4.2.

## 3.4 Sites of SWCX in the Solar System

SWCX processes occur at many locations within the Solar System including planetary exospheres, the corona of comets, within the heliosphere and at the heliospheric boundary where the outer reaches of the interplanetary magnetic field encounter that of the surrounding interstellar medium. There are comprehensive review papers on the subject of X-ray emission and charge exchange in the Solar System (Bhardwaj et al., 2007; Dennerl, 2010). We give a brief account of several of the charge exchange emission sites within the Solar System here.

### 3.4.1 Comets

Comet Hyakutake was the first comet whose X-ray emission, as observed by ROSAT (Lisse et al., 1996), was assigned to the SWCX emission process (Cravens, 1997). This SWCX emission occurs from the interaction of the solar wind with neutral species that outgas from the comet as it enters the inner Solar System, and the amount of outgassing is dependent on the comet's distance from the Sun. These neutral species are mainly water and its dissociation products. The SWCX emission must occur in cometary regions where photoionisation and destruction of the neutral species can occur. Water has a short lifetime when exposed to solar UV photons and therefore survives longer in the coma interior, whereas its dissociation products (along with CO providing the comet has a sufficiently high carbon abundance) can survive further into the outer coma regions. A detailed description of X-ray emission from comets, primarily using data from the *Chandra* observatory, can be found in Bodewits et al. (2007).

As we have seen, the solar wind is a collisionless plasma and so its ion composition is determined in the solar corona (bar any changes caused by charge exchange processes occurring within the inner heliosphere, which are discussed in Section 3.4.3). Signatures of SWCX

occurring throughout the Solar System can therefore be used to infer the composition of the solar wind, which varies considerably throughout the solar cycle and with solar latitude. As cometary orbits are not restricted to the ecliptic plane they are ideal locations to study compositional signatures from solar wind originating from a variety of solar wind latitudes (Dennerl et al., 1997). Bodewits et al. (2007) was able to use cometary X-rays to distinguish emission resulting from three solar wind types: the cold and fast wind, the warm and slow wind and the warm and disturbed wind (such as during transient solar wind phenomena). In addition, as the gas around a comet is cold and due to the absence of strong magnetic fields in its vicinity, thermal and X-ray emission resulting from energetic electrons is essentially neglible providing an ideal laboratory for the study of charge exchange reactions.

### 3.4.2 Planets

The presence of magnetic fields deflects and accelerates the highly charged ions of the solar wind. Therefore it is useful to consider SWCX emission from those planets with and without a magnetic field as separate cases (Dennerl, 2010). Venus and Mars have no substantial magnetic fields but have non-neglible atmospheres (densities of $\sim 10^{14}\,\mathrm{cm}^{-3}$ and $\sim 10^{12}\,\mathrm{cm}^{-3}$ at a height of 110 km respectively). Charge exchange emission may occur in the outer layers of the atmosphere, before the incoming ion has been neutralised by the ongoing process of electron gain. In addition to charge exchange, X-rays originating from the Sun are observed that have been scattered by the atmosphere. Scattering cross-sections are much smaller than charge exchange cross-sections ($\sim 10^{-18}\,\mathrm{cm}^2$ as compared to $\sim 10^{-15}\,\mathrm{cm}^2$ at X-ray energies corresponding to SWCX emission), although scattering may dominate providing the solar X-ray flux to heavy-ion ratio is sufficiently large (Dennerl, 2010).

Venus was first observed by an X-ray observatory with *Chandra* in January 2001 (Dennerl et al., 2002) (XMM-*Newton* is unable to view Venus due to solar avoidance restrictions),

wherein fluorescence lines of C-K$_\alpha$, O-K$_\alpha$ and N-K$_\alpha$ were observed in emission from along the sunward limb of the planet. Later observations of the planet, also by *Chandra*, revealed an additional X-ray emission component from charge exchange (Dennerl, 2008). Charge exchange X-ray emission was observed at Mars with XMM-*Newton* that accompanied the fluorescence that had previously been detected by *Chandra* (Dennerl, 2006, and references therein), and the sources of emission in the later observation could be spatially resolved. The charge exchange emission originated in the much more extended exosphere of the planet and fluorescence emission, dominated by $CO_2$ lines, was observed in the upper atmosphere.

The gas giants of Jupiter and Saturn have also been seen to emit in X-rays. Jupiter has the largest planetary magnetic field in the solar system ($\sim$0.4 mT at the equator). X-ray emission from the auroral regions has been observed by XMM-*Newton* primarily in the O VII band (Branduardi-Raymont et al., 2007, and references therein). A component from bremsstrahlung emission resulting from electron precipitation into the magnetosphere was also observed and its variability on the order of a few days suggested it was related to solar activity. X-rays from the disk region of the planet, rather than the aurorae at the poles, show a spectrum markedly different in shape than that from the aurorae (Branduardi-Raymont et al., 2007). The disk spectrum is harder than the aurorae and suggests scattering of solar radiation, as shown by observations taken by both XMM-*Newton* and *Chandra*.

Saturn has been observed several times by XMM-*Newton* and *Chandra*. Similarly to the disk emission from Jupiter, the X-ray emission from this region is interpreted as originating from the scattering of solar X-rays (using an optically thin coronal model with average temperature of 0.5 keV), with an additional fluorescence line at $\sim$0.53 keV from oxygen (Branduardi-Raymont et al., 2010). The disk emission is variable and has been shown to decrease in correlation with a decrease in solar activity, over the range of a few years over which the observations were taken. Saturn aurorae (visible in the far ultra-violet) have not been detected through X-ray emission, as the strength of the expected emission is likely to be beyond the ca-

pabilities of the current suite of X-ray observatories. Similarly, remote Solar System objects, such as the outer planets of Uranus and Neptune, are expected to emit X-rays, via scattering or precipitation but they are probably too faint to be observed with current Earth-orbiting instrumentation (Bhardwaj et al., 2007).

After the charge-exchange related cometary studies in the 1990s and onwards, it was postulated that the same emission mechanism could be responsible for X-ray emission originating in the Earth's exosphere (Dennerl et al., 1997; Cox, 1998; Freyberg, 1998). The so-called Long Term Enhancements (LTEs) in observations taken by ROSAT (Snowden et al., 1995) were later assigned to time-variable SWCX. Images from the ROSAT all sky survey, before and after cleaning of the LTEs, are given in Figure 3.2. Observations of the Moon by *Chandra* (Wargelin et al., 2004), following on from those previously by ROSAT, re-interpreted the time-variable X-ray emission as resulting from charge exchange, rather than a bremsstrahlung continuum (Schmitt et al., 1991).

Modelling efforts by Robertson & Cravens (2003a,b) and Robertson et al. (2006) have used input solar wind conditions and a model of neutral hydrogen about the Earth (the Hodges 1994 model under solar conditions with the solar-activity proxy of the 10.7 cm radio flux value (also known as the $F_{10.7}$ index) at 180 solar flux units) to generate X-ray images of exospheric SWCX emission from various vantage points. Two such examples are shown in Figure 3.3. The left panel shows an image created from a model constructed using nominal solar wind conditions ($n_{sw} \sim 7\,\mathrm{cm}^{-3}$, $v_{sw} \sim 400\,\mathrm{km\,s}^{-1}$, with a line-of-sight integration length of $100\,R_E$). The right panel shows an image created using input conditions based on a solar storm that occurred on $31^{st}$ March 2001 (integration length $50\,R_E$). The increase in intensity by a factor of about 20 is the remarkable difference between the two sets of conditions and illustrates how the time variable nature of the solar wind can result in sharp changes in the level of SWCX emission. In addition, the cusp regions of the magnetosheath have been added in the model for the solar storm and can clearly be detected for these conditions. During the

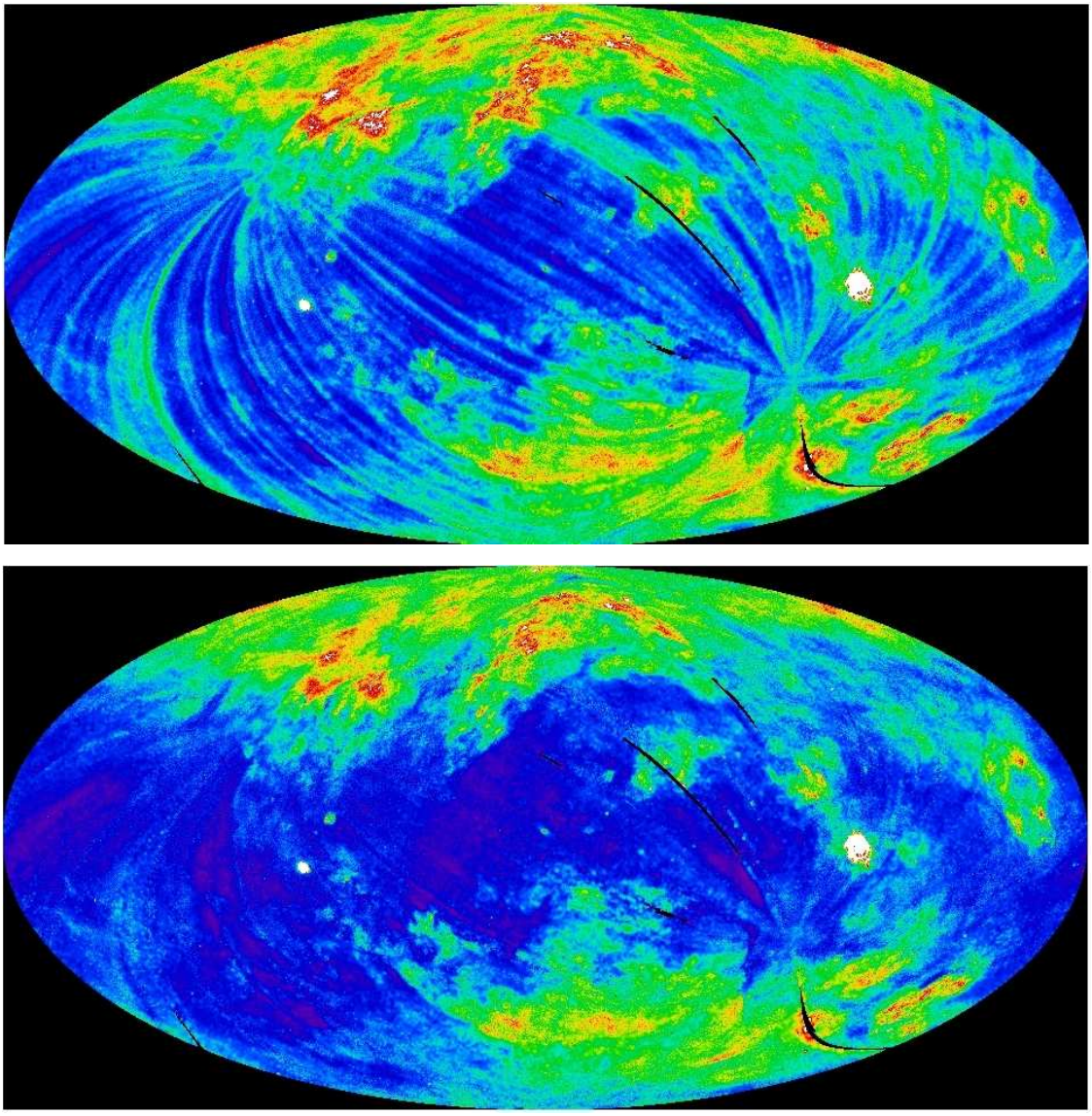

**Figure 3.2:** ROSAT particle-induced and solar X-ray background removed $\frac{1}{4}$ keV band images, plotted in Galactic coordinates using an Aitoff-Hammer equal-area projection. LTEs, in the form of streaks across the image, are visible in the first panel. A cleaned image with the LTEs removed is given in the second panel, credit: Steve Snowden (NASA).

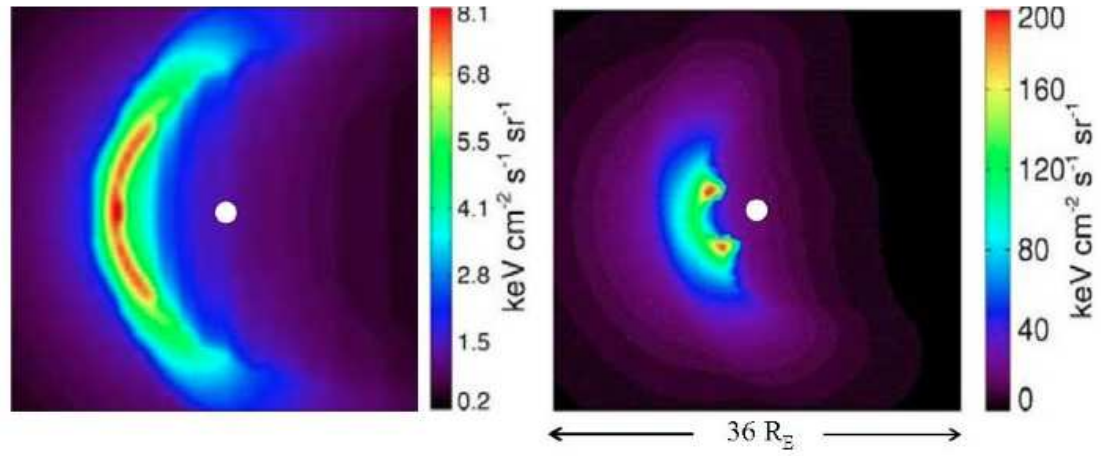


**Figure 3.3:** Modelled X-ray images of SWCX occurring in the Earth's exosphere, for nominal solar wind conditions (left panel) and for storm event conditions (right panel). The Sun is to the left in both cases, credit: Robertson et al. (2006).

solar storm the Earth's magnetic field is compressed closer to the surface, allowing solar wind plasma to be funnelled into regions with higher densities of neutrals. These modelling efforts have indicated that imaging of the magnetosheath using X-ray emission may reveal much about the structure of the magnetosheath and aid studies of the solar-terrrestrial connection.

Enhancements in soft-band X-ray XMM-*Newton* spectra have been attributed to exospheric-SWCX in the literature. This has almost exclusively involved the comparison of multiple pointings of the same field which has enabled the serendipitous detection of the low-energy enhancement, most notably around the O VII helium-like triplet at approximately 0.56 keV. Snowden et al. (2004) were able to detect one of a set of four observations of the *Hubble* Deep Field North that showed an increase in the band 0.52 to 0.75 keV compared to steady values in a higher energy band from 2.0 to 8.0 keV, which was deemed to be the result of exospheric SWCX. As a field free of bright X-ray sources, the authors were able to easily compare the count rates over an observing campaign that was spread over a two week period in 2001, not long into the XMM-*Newton* mission and during solar maximum conditions. The line-of-sight required by the target pointing passed through the subsolar region of the Earth's magnetosheath. Lightcurves from the affected observation (the last of the set) were compared

with the solar wind proton flux and $O^{7+}/O^{6+}$ ratio, using data from the solar wind monitoring spacecraft the Advanced Composition Explorer (ACE, Stone et al. 1998). The 0.52 to 0.75 keV band lightcurve showed an enhancement in the first half of the observation for approximately 4 ks and this period was termed the 'high' state. The latter half saw the lightcurve return to levels typical of the average count rates seen in the other three observations of the set. Increases in both the solar wind proton flux and $O^{7+}/O^{6+}$ ratio occurred during the 'high' state, however short-term variations in the solar proton flux were not reflected in the X-ray lightcurve. Later work by Collier et al. (2005) explained that, due to the size and orientation of the solar wind wavefront travelling through the Solar System, the smoothing of the X-ray lightcurve was the result of the intersection of the line-of-sight of XMM-*Newton* with the solar wind enhancement considerably upstream of the subsolar region, and also as it moved closer to and past the Earth. After using the previous three XMM-*Newton* observations along with a spectrum derived from the ROSAT All Sky Survey to constrain the diffuse sky background in the pointing direction of the field of study, the authors were able to produce a model of SWCX emission that contained 7 lines for the 'high' state period. Lines were added for C VI, O VII, O VIII, a complex made up of iron or higher order O VIII transitions, Ne IX and Mg XI. The contribution from the O VII ion required a flux of approximately 8 line units (LU or photons $cm^{-2}\,s^{-1}\,sr^{-1}$).

Henley & Shelton (2010) conducted a large archival XMM-*Newton* survey with the aim to characterise, particularly at energies representative of O VII and O VIII, the soft X-ray background in a large area of the sky. Their sample contained 69 sets of multiple pointings of the same target field. By comparing the brightest O VII or O VIII flux to the faintest in each set, they determined that enhancements due to SWCX typical show increases in the O VII flux of $\lesssim$4 LU or $\lesssim$2 LU for O VIII. The maximum enhancements seen were 26 LU and 8 LU for O VII and O VIII respectively. Potential correlations were investigated between solar wind proton and O VII fluxes, but the authors concluded that the solar wind proton flux is not a good indicator of the level of SWCX enhancement detected. In addition, they found

no correlation with the closeness of the line-of-sight passing through the subsolar region of the magnetosheath and the magnitude of the oxygen enhancement. Kuntz & Snowden (2008) also observed cases of exospheric-SWCX enhancement within a large data set originally analysed to investigate the particle-induced background of the XMM-*Newton* EPIC-MOS cameras. The analysis of several sets of multiple pointings towards the same target field enabled the identification of these cases. After constructing a simple model of the magnetosheath and noting the pointing direction of each SWCX case, they concluded that significant SWCX enhancements are seen for when both the solar wind proton flux exceeds $4\times10^8\,\mathrm{cm^{-2}\,s^{-1}}$ and the line-of-sight intersects the subsolar region. One case exhibited a very high proton flux of $1.5\times10^9\,\mathrm{cm^{-2}\,s^{-1}}$, but occurred when the line-of-sight intersected not the subsolar region but the flanks of the magnetosheath.

A long, 100 ks observation taken by XMM-*Newton*, specifically to study exospheric SWCX, was taken in June 2006 (Snowden et al., 2009). The pointing geometry was chosen to intersect the subsolar region of the magnetosheath and towards a target field that was faint in the $\frac{3}{4}$ keV band to minimise the cosmic background. The solar wind was however, at the time of the observation, in a fairly quiescent state. The authors modelled the expected X-ray emission by perturbing the incoming solar wind $O^{7+}$ flux in the region of the magnetosheath and using a simple model of neutral hydrogen in the exosphere and helium in near interplanetary space. After intergrating out to 200 $R_E$ they produced a lightcurve of modelled X-ray SWCX emission in a band representative of O VII. A good correlation was found between the modelled and observed X-ray lightcurve with an average intensity of 2.6$\pm$0.5 LU. The authors also commented that a sufficiently refined model of SWCX emission may allow subtraction of its contribution from future X-ray data, although various uncertainities remain in the model of the solar wind perturbations in the magnetosheath and that the model is limited by the time resolution of the upstream solar wind data. Also, it should be noted that solar wind data (proton or ion fluxes) are not always available during an XMM-*Newton* observation or that these data might be sparse. A time resolved model of expected X-ray emission is discussed

in Chapter 8.

Observations in the literature using data from both *Suzaku* and *Chandra* have reported SWCX enhancements that have been attributed to exospheric or near-Earth emission, whose results are reviewed briefly here.

Fujimoto et al. (2007) observed a low-energy (0.2 to 2 keV) enhancement period (the flare) lasting approximately 10 ks in an observation of the North Ecliptic Pole, taken using the X-ray Imaging Spectrometer onboard the *Suzaku* satellite. The line-of-sight of this observation intersected the northern cusps region of the Earth's magnetosphere and the authors concluded that the emission resulted from charge exchange occuring between 2 and 8 $R_E$ from the Earth. The X-ray enhancement corresponded with a period of increased solar proton flux, once the delay between ACE and the Earth was taken into account. Shorter scale variations of the low-energy enhancement during the flare period were attributed to changes in the distance to the emitting region of the magnetosheath. Nine emission lines were required to be added to the model of the steady-state background signal during the flare period. An emission line from a high-*n* transition of C VI at 459 eV (4p-1s) was comparable in strength to that of the C VI line at 367 eV (2p-1s). High-*n* transitions are expected from charge exchange spectra as described in Section 3.1. Emission from O VII, O VIII, Ne X, Mg XI, low energy blends of carbon (modelled as a single line at 269 eV) and blends of iron, oxygen and neon (between 750 and 900 eV, modelled as two lines at 796 eV and 882 eV) was also seen. A deep, 100 ks *Suzaku* observation of the Galactic Ridge (Ezoe et al., 2010) also exhibited time-variable emission in the band 0.5 to 0.65 keV (O VII) that was correlated with an enhancement in the solar wind proton flux measured by the *Wind* spacecraft (Acuña et al., 1995) and the solar wind $O^{7+}$ flux as measured by ACE. After eliminating the possibility that the emission resulted from X-ray fluorescence scattering in the Earth's atmosphere, the time-variable component was concluded to originate from exospheric SWCX, contributing almost double the flux from the soft X-ray background plus any other SWCX-emission contribution from the heliosphere

combined. In addition, the O VII observed during this case was greater in flux to that observed in the previous Fujimoto et al. (2007) exospheric-SWCX example. The line-of-sight for this pointing intersected the subsolar region of the magnetosheath. Bautz et al. (2009) required a SWCX component to be added to their model when fitting data, obtained by *Suzaku*, of the cluster Abell 1795. They required line emission from the O VII triplet at 0.574 keV plus additional, less prominent lines from O VIII, Ne IX, Ne X, Mg XI and Mg XII. The strength of the O VII line for the Fujimoto et al. (2007) case was 5 LU whereas 7 LU was seen for the Ezoe et al. (2010) case, which was the upper limit for the O VII component required by Bautz et al. (2009).

An observation taken by *Chandra* towards the molecular cloud MBM 12, with the aim to measure the local X-ray background in an oxygen band, appears to have detected solar wind charge exchange resulting from a CME interacting with neutral gas in interplanetary space (Smith et al., 2005). The authors arrived at this interpretation after noting the high O VIII to O VII ratio ($\sim$1.3), which is uncharacteristic of a steady, slow solar wind.

### 3.4.3 Interplanetary space and the heliosphere

As well as in the vicinity of comets and planets, charge exchange can occur within interplanetary space within the heliosphere and to a much lower level at the heliosheath boundary. Soft X-ray emission originating from charge exchange within the heliosphere was first proposed by Cox (1998) and there have been considerable modelling efforts to characterise this emission due to its implications for wider studies of diffuse emission, particularly the debate surrounding the nature of the Local Hot Bubble; the 100 pc cavity of low-density X-ray emitting hot gas ($\sim 10^6$ K) in thermal equilibrium in which the Sun apparently resides (Snowden et al., 1990). By combining the modelling of heliospheric oxygen emission and comparing this to observational evidence from the ROSAT All Sky Survey, Koutroumpa et al. (2009b) conclude

that the 3/4 keV band emission is entirely due to heliospheric emission. The task to separate local components is not simple as charge exchange from the geocorona and heliosheath show very similar emission line spectra. The dominant contributions from oxygen also form the major component of the supposedly distant diffuse X-ray emission. This relatively quiescent component to the X-ray background (along with any quiescent exospheric-SWCX component) has serious implications for the model of the Local Hot Bubble. Alternative models of a modified Local (Hot) Bubble, after considering the contribution from heliospheric X-rays, have been put forward that require the reduction in temperature of the supposedly hot gas and a reconsideration of its spatial distribution (Welsh & Shelton, 2009). It is therefore important to understand and quantify SWCX emission to fully assess its impact on the gathering of astronomical X-ray data, not only in the vicinity of the Earth, but also in the wider heliosphere.

Interstellar hydrogen and helium flow into the heliosheath where they can be photoionised by solar ultraviolet radiation or charge exchange with solar protons or alpha particles. Hydrogen, compared to helium, is strongly affected by radiation pressure, which results in a lack of hydrogen close to the Sun and an anisotropic distribution between the upwind and downwind directions (Fahr, 1974; Quemerais et al., 1993). Helium, due to its lower cross-section, is less affected by photoionisation so it can permeate deeper into the heliosphere where it is gravitationally focussed downstream of the Sun. This is caused by the Sun's relative motion in the Local Interstellar Cloud region of the Galaxy (a low density extended structure in which the Sun is passing, Slavin 2009) of $\sim$20 km s$^{-1}$ in the direction of 252°, 7° (ecliptic longitude and latitude) into the distribution known as the helium focussing cone (Weller & Meier, 1974). The helium focusing cone is directed towards 73.9°, -5.6° (ecliptic longtidude and latitude, Witte et al. 1996). The Earth is found inside the helium focusing cone region during the northern hemisphere winter. Hydrogen and helium in the inner Solar System can also charge exchange with solar wind heavy ions, as in the case of charge exchange in the terrestrial exosphere, resulting in the emission of X-rays. This emission is

also dependent on the composition and intensity of the solar wind and so is dependent on the solar cycle. The spatial distribution, and the spectral and temporal nature of the intensity of the heliospheric X-ray component has been modelled for the inner Solar System (up to $\sim$10 AU) (Cravens, 2000; Cravens et al., 2001; Koutroumpa et al., 2006, 2007; Lallement, 2004; Pepino et al., 2004; Robertson et al., 2001; Robertson & Cravens, 2003a). Robertson & Cravens (2003a) calculate that the X-ray intensity in the helium focusing cone can be as much as $26\,\mathrm{keV\,cm^{-2}\,s^{-1}\,sr^{-1}}$. Because of the distribution of hydrogen and helium within the Solar System and the stratification of the solar wind (especially during solar minimum conditions as previously described), the heliospheric contribution varies strongly with heliospheric latitude. This has been observed by comparing observations of the North and South Ecliptic Pole to observe away from and through the helium cone respectively, although further observations are required to constrain SWCX emission from the cone and its dependence on the solar cycle (Koutroumpa et al., 2009a).

## 3.5 X-ray missions and viewing exospheric SWCX

There are multiple examples of observations, from a variety of X-ray observatories, exhibiting an enhancement in a soft-energy band ($<$2 keV) that have been attributed to exospheric SWCX, as mentioned in this chapter. Excluding a dedicated observation to observe exospheric SWCX (as described in Snowden et al. (2009) and summarised in Section 3.4.2), these examples have identified SWCX affected time-periods via comparisons between same-field multiple pointings with the intention to study a different astronomical target. This thesis, however, contains a method to identify individually affected observations, without the need for such a comparison, which is described in subsequent chapters.

The possibilities for viewing exospheric SWCX emission in the vicinity of the Earth depend on the orbital and viewing constraints of the observatory in use. During various periods of

its orbit and depending on observational constraints, XMM-*Newton* may view regions of the Earth's magnetosheath which are predicted to exhibit the highest X-ray emissivity due to exospheric SWCX (the subsolar region, Robertson et al. 2006, and references therein). A schematic of the orbit of XMM-*Newton* with reference to the approximate position of the magnetosheath is shown in Figure 3.4. As described before, the magnetosheath position and shape is not static, but will move in response to conditions in the solar wind. XMM-*Newton* is not able to observe through the subsolar region at all times due to the configuration of its highly elongated, 48 hour elliptical orbit. The viewing direction of XMM-*Newton* is strongly constrained by the fixed solar panels and those constraints imposed to protect the instruments from directly viewing the Sun (a solar aspect angle of between 70° and 110° must be maintained at all times), the X-ray and optically bright Earth and Moon, and the non-operational periods during the telescope's passage through perigee as it passes through the radiation belts. The resulting effect is that XMM-*Newton* is only able to view the subsolar region at certain times throughout the year. SWCX-affected observations are therefore expected to occur with a higher frequency during the summer months (northern hemisphere) as this is when the telescope is able to be in a position to look through the subsolar region and bright flanks of the magnetosheath. However, the apogee and perigee positions of XMM-*Newton*'s orbit are slowly precessing. The evolution of the distances from Earth to both the apogee and perigee positions of XMM-*Newton* are shown in the left-hand panel of Figure 3.5. The orbit is becoming less elliptical as the mission progresses. This has the effect that apogee is no longer found sunward at approximately the middle of summer. The precession of the apogee and perigee positions is shown in the right-hand panel of Figure 3.5. Here we plot the Geocentric Solar Ecliptic Coordinates (GSE) X coordinate of the apogee and perigee positions against time. The GSE coordinate system is defined so the positive X-axis is directed from the centre of the Earth to the Sun. The Y-axis is positive in the direction that opposes the orbital motion of the planet and the Z-axis is positive towards the Ecliptic North Pole. The maxima and minima of the apogee distance per year is slowly moving away from the current summer and

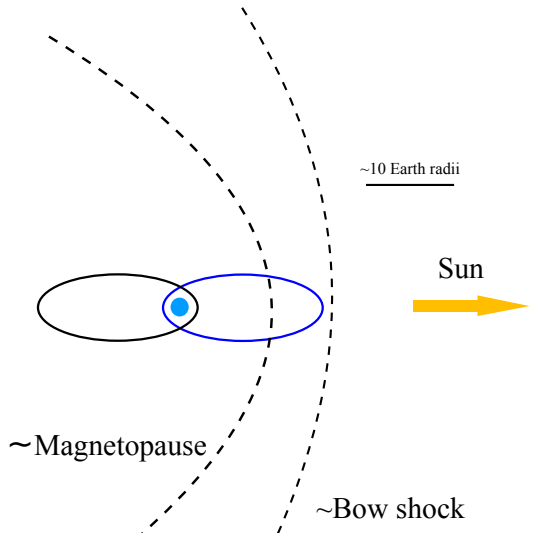


**Figure 3.4:** Schematic of XMM-*Newton*'s orbit about the Earth as viewed above the ecliptic plane. The approximate summer and winter configurations of the orbit are shown (blue and black solid lines respectively). Illustrative magnetopause and bow shock boundaries are shown by the black dashed lines.

winter solistic positions respectively. The maximum GSE-X apogee distance during the year 2001 occurred on the 13$^{th}$ of July. However, the maximum GSE-X apogee distance during the year 2008 occurred on the 20$^{th}$ of March. The differences here have implications for our work in Chapter 5.

## 3.6 Summary

SWCX is an important X-ray emission mechanism throughout the Solar System. We concentrate throughout this thesis on the study of SWCX emission occurring in the near vicinity of the Earth. We use the time variable nature of this emission as our marker for selecting affected XMM-*Newton* observations. This will be the focus of the next chapter.

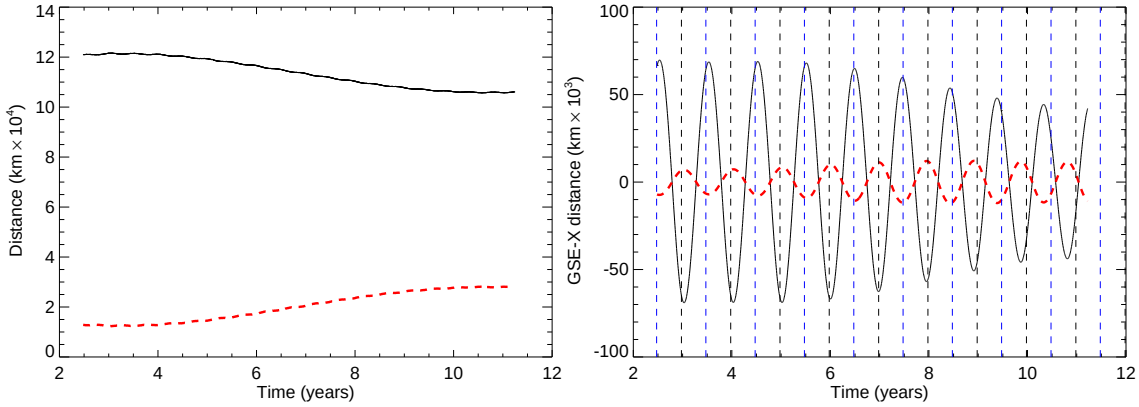


**Figure 3.5:** Left panel: distances to XMM-*Newton* at the positions of apogee (black, solid line) and perigee (red, dashed line). Right panel: distances to the GSE-X positions of apogee (black, solid line) and perigee (red, dashed line). We overplot the times of summer (blue, dashed) and winter solistices (black, dashed). The x-axis in both cases shows the time since the XMM-*Newton* reference time of 1998-01-01T00:00:00.

Chapter 4

# Searching for exospheric SWCX in the XMM-Newton archive

In this chapter we describe the data analysis steps taken to search for incidences of exospheric-SWCX enhancements during observations by XMM-*Newton*. This work has been presented in two papers; Carter & Sembay (2008), hereafter referred to as Paper I and Carter et al. (2011), hereafter referred to as Paper II. Paper I consisted of an initial study of a small selection of 169 XMM-*Newton* observations to establish a method to identify cases of time-variable exospheric-SWCX emission. This method was extended to the available archive in Paper II.

## 4.1 Data selection

All observational data used in this study are available through the XMM-*Newton* Science Archive (XSA) from where the Original Data Files (ODF) were extracted. Observations taken by the EPIC-MOS cameras (MOS1 and MOS2) using the full-frame mode only were

considered. The observations used provided an even sample across the mission and the event list data from the cameras could be combined if the same filter was used for both. Observations were considered up to and including revolution 1773 (August 2009).

## 4.2 Flare-filtering and point source removal

Individual observation event lists were created from the ODFs for each EPIC-MOS camera and filtered for soft-proton contamination using the publicly available Extended Source Analysis Software (ESAS)[1] package (*mos-filter* tool) and as described in Snowden et al. (2008). At the time of data processing, ESAS was only available for the EPIC-MOS cameras. The *mos-filter* tool incorporates calls to various XMM-*Newton* Science Analysis System[2] (SAS) tasks, initially building event lists from the ODFs. Once the event lists are built, the SAS task *evselect* is used to extract two lightcurves: one from inside the FOV and the other from the un-exposed corners of the detectors.

The next step sees the *mos-filter* Fortran sub-procedure *clean-rel* fit a Gaussian to a histogram of in-FOV count rates in a high energy band (2.5 to 12.0 keV). Time periods with count rates beyond a threshold of $\pm 1.5\sigma$ away from the mean value of this Gaussian were removed by applying a Good Time Interval (GTI) file to the event lists. Example Gaussian profiles for two different observations are shown in Figure 4.1. To establish this profile, the ESAS software determines the most likely value of the quiescent background rate, for example the modal value of the count rate histogram. A Gaussian profile is then fit to a small window of count rates either side of this value, as shown by the blue vertical lines of Figure 4.1. The mean and $\sigma$ of this Gaussian profile is determined. The red vertical lines indicate the limits taken for the GTI periods ($\pm 1.5\sigma$ from this mean). The GTI files created for each EPIC-MOS

[1] http://heasarc.gsfc.nasa.gov/docs/xmm/xmmhp_xmmesas.html
[2] http://xmm.esac.esa.int/external/xmm_data_analysis/

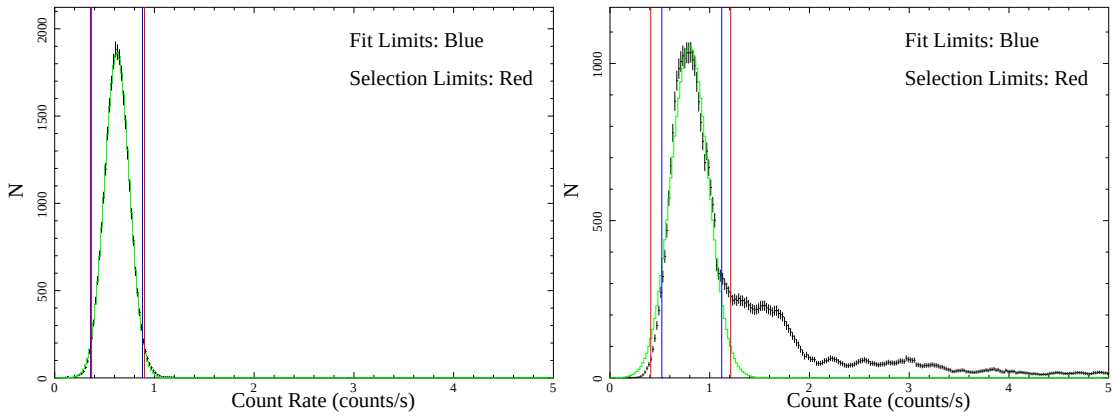


**Figure 4.1:** Example count rate histograms from the ESAS software where a Gaussian shaped curve is fitted to the histogram. The first panel shows a count rate histogram where the data and the Gaussian curve are almost coincident and little or no flaring has occurred, whereas the second panel shows flaring characteristics.

event list were combined together to form one EPIC-MOS GTI file and this file was reapplied to both the MOS1 and MOS2 event lists to provide simultaneous coverage during each observation. Resolved point sources (from lists created for the 2XMM catalogue (Watson et al., 2009) using a minimum likelihood threshold $\geq 6$), were removed from the FOV by extracting events in a circular region of 35 arcseconds radius about the source position. This extraction radius corresponds to a encircled energy fraction of approximately 85% at 1.5 keV on-axis. An example event file with and without the extracted events is shown in Figure 4.2. Those observations judged, after a visual inspection (and prior to creation of any spectra, see Chapter 6), to show residual source contamination (the wings of the point spread function of the EPIC-MOS camera being evident in an image of the event file) passed through an additional spatial filtering stage using a larger extraction region to further clean the dataset and minimise the risk of contamination from residual point sources in the filtered event file. We discuss further screening steps in more detail in Section 4.5.

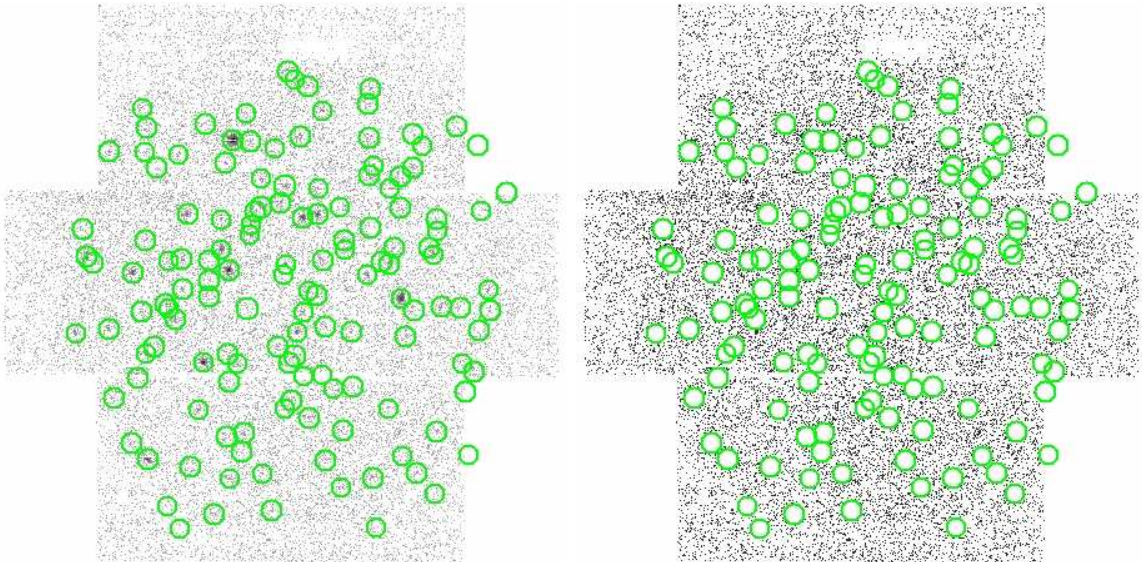

**Figure 4.2:** Left panel: example image constructed from flare-filtered MOS1 events, plotted in detector coordinates. Right panel: the same image but with resolved point sources extracted. The point source extraction regions are over-plotted (green circles) in each case.

## 4.3 Lightcurve creation

Two lightcurves with bin size of 1 ks were created for each observation from events within the full FOV (radius of 13.3 arcminutes). When both EPIC-MOS cameras were used during an observation and employed the same filter, events from both cameras were used to construct the lightcurves. The first lightcurve was chosen to represent the continuum, covering events with energies in the range 2.5 to 5.0 keV and which should be free of SWCX. The second lightcurve was extracted using events with energies in the range 0.5 to 0.7 keV to cover the strong SWCX emission from O VII and O VIII (the line-band lightcurve). This energy range incorporates emission energies from the O VII triplet and resonance lines which are dominated by the forbidden line transition at 0.56 keV. Lightcurves were then exposure-corrected for periods removed during the filtering steps. As the MOS1 and MOS2 event files for each observation, prior to the lightcurve creation, were filtered using a single GTI file which is not energy specific, the exposure-coverage for each bin was the same for the line-band and continuum lightcurves. Therefore the same exposure-correction factor for an individual bin

was applied to both lightcurves in this step. We keep bins of the lightcurve with at least 60% of the full exposure for that bin and reject the remaining bins. Lightcurves were rejected from further analysis, after all other GTI and bin-rejection procedures had been applied, that were less than 5 ks in duration. By increasing the strictness of the bin coverage thresholds, we reduced the incidence of type I errors (those incorrectly labelled detections), but ran the risk of increasing the number of cases that were incorrectly labelled as non-detections (i.e. not showing a deviance from the null hypothesis of a linear fit between the line and continuum band (type II errors). We scaled each lightcurve by its mean to produce adjusted lightcurves. The count rates for the line-band and the continuum band were then always of the same order which facilitated the identification of periods of enhancement in the line-band lightcurve. An example of the combined-MOS lightcurve adjustment process can be found in Figure 4.3 (panels top-left, top-right and bottom-left).

## 4.4 Testing for SWCX

We plotted a scatter plot between the two bands (using the adjusted line-band as the dependent variable), shown in Figure 4.3. A linear model fit to each scatter plot was computed using the IDL procedure, *linfit*, which minimises the $\chi^2$ statistic.

We computed the reduced-$\chi^2$ for the fit, hereafter referred to as $\chi^2_\mu$, by dividing the $\chi^2$ by the number of bins minus one, to account for the reduction in the number of degrees of freedom made by fitting a linear model to the data. A high $\chi^2_\mu$ indicates that a significant fraction of the points deviate significantly from the best-fit line. We expected these cases would be more likely to show variable SWCX-enhancement. In addition, we computed the $\chi^2$ values for each individual lightcurve in terms of the deviation from the mean of that lightcurve (Equation 4.1):

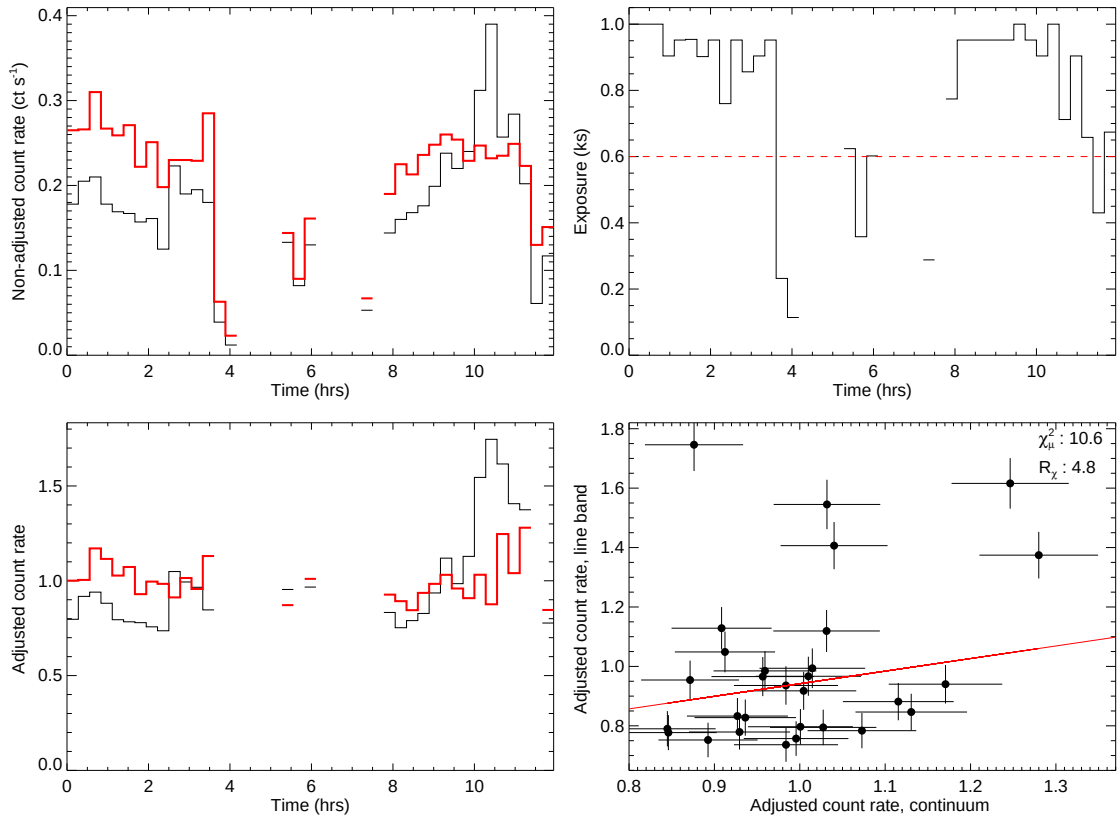


**Figure 4.3:** Example of the lightcurve correction procedure for observation with identifier 0150680101 (black - line-band, red - continuum for panels top-left and bottom-left). Top left: example lightcurves showing a peak in the line-band that is not reflected in the continuum. Top right: exposure coverage for each bin, the threshold at 60% is marked by the red dashed line. Bottom left: lightcurves after the adjustments for exposure correction and scaling by the mean. Bottom right: scatter plot between the adjusted lightcurves.

$$\chi^2 = \sum_{i=0}^{n-1} \frac{(rate_i - \mu)^2}{error_i^2} \tag{4.1}$$

where $\mu$ is the mean for that lightcurve and $rate_i$ and $error_i$ the lightcurve values and associated errors in each bin.

We calculated the ratio between the line-band and continuum $\chi^2$ values to add to our diagnostic (hereafter denoted as $R_\chi$).

3012 observations made up the final sample to be used for further analysis. The results from Paper I showed us that those observations exhibiting both high $\chi^2_\mu$ and high $R_\chi$ were most likely to show near-Earth time-variable SWCX signatures. Observations that fulfilled these criteria were considered for further analysis: spectrally, temporally and with regard to the orientation of XMM-*Newton*.

After ranking the observations, we were able to study those that exhibited the highest $\chi^2_\mu$ and $R_\chi$ in more detail on a case by case basis.

## 4.5 Further screening

All observations in our final sample, after any rejections as described below, were ranked by $\chi^2_\mu$. The two highest ranked observations were observations of comets. Although resolved point sources have been removed, cometary X-rays are diffuse and will likely be spread over a large fraction, if not all of the FOV. It was assumed that the dominant variations in the line-band lightcurve that result in such high ranking are due to SWCX emission occurring within the cometary coma and not to any emission occurring within the vicinity of the Earth. The cometary (and planetary) cases within the data set are discussed in Section 4.8.

Observations were examined for residual point or extended sources that may contribute to high variability in the line-band. Those observations where the wings of the PSF were clearly visible in an image of the event file, due to an extremely bright source most commonly on-axis, were not considered further to be have experienced any SWCX enhancement. Extended or diffuse residual sources that remain in the FOV will not affect this detection method providing no inherent variation occurs within these sources in either one of the bands, as expected for sources outside the Solar System. Cases were also examined for residual soft proton contamination. Although the files used in this analysis have been filtered for periods of soft proton flaring, residual contamination may remain. Excessive scatter due to residual soft proton contamination impedes the ability to identify periods of exospheric SWCX and will result in some type II errors in our sample. Also, exospheric SWCX can occur throughout the entirety of an observation with little or no variation in the line-band, resulting in these occurrences being passed over for consideration. Excessive and simultaneous variations in both the line-band and continuum will result in a high $\chi^2_\mu$ yet a low value of $R_\chi$. We concentrate our analysis therefore on cases that exhibit both high $\chi^2_\mu$ and high $R_\chi$.

For some observations with short lightcurves, it was impossible to identify any time-periods of boosted line-band emission (the putative SWCX enhancement periods). These observations were disregarded as SWCX-enhancement cases. Also, the method described in this work tested only for variable SWCX on short timescales. Spectral analysis of suspected SWCX cases was therefore only possible when a clear line-band enhancement period could be identified during the duration of the observation. Lightcurves and a scatter plot from an example observation that was rejected from further analysis are shown in Figure 4.4.

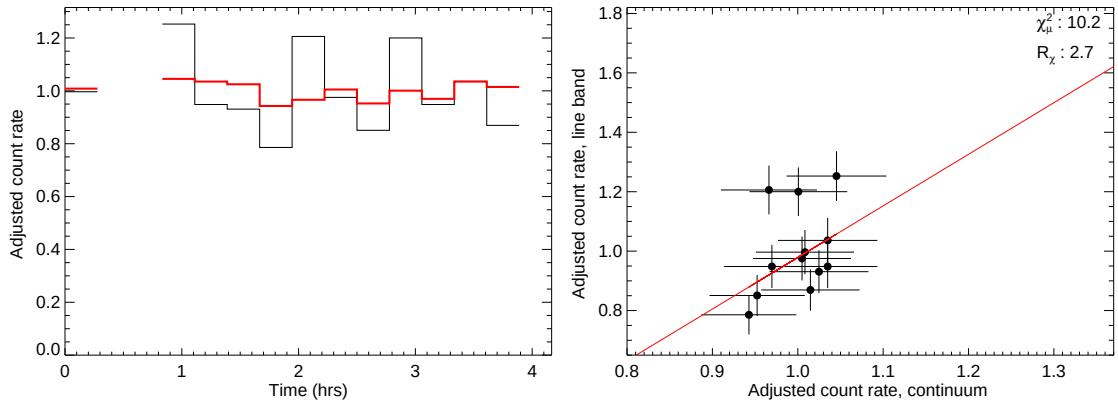


**Figure 4.4:** Adjusted lightcurve and scatter plot example for observation with identifier 0153350101 that was rejected from further analysis. Left: lightcurves after the adjustments for exposure correction and scaling by the mean (black - line-band, red - continuum). Right: scatter plot between the adjusted lightcurves.

## 4.6 SWCX dataset overview

We find 103 observations in our sample that show indications of a time-variable exospheric-SWCX enhancement, that are not excluded from consideration based on the reasons described above. These 103 observations comprise the set of observations hereafter referred to as the SWCX set. All of these cases had a $\chi^2_\mu$ value greater than or equal to 1.2 and a $R_\chi$ value of greater than or equal to 1.0. These limits were determined by a careful inspection of each observation's set of diagnostic files (such as in Figure 4.3), image of the event file and the Gaussian profile output from the ESAS software to establish that considerable residual soft proton or point source contamination had not occurred and that a SWCX enhancement time period in the line-band lightcurve could be identified. These SWCX set cases make up only $\sim$20% of all observations that have values of $\chi^2_\mu$ and $R_\chi$ above these thresholds, indicating that although the values of $\chi^2_\mu$ and $R_\chi$ are indicators of a SWCX-enhancement, considerable inspection of an observation on a case-by-case basis is still required. The majority of cases in the whole sample have a $R_\chi$ value less than 1, indicating that there is more variation seen in the continuum compared to the line-band. The continuum incorporates the break energy at $\sim$3.2 keV in the two-power law models of residual soft proton contamination (Kuntz &

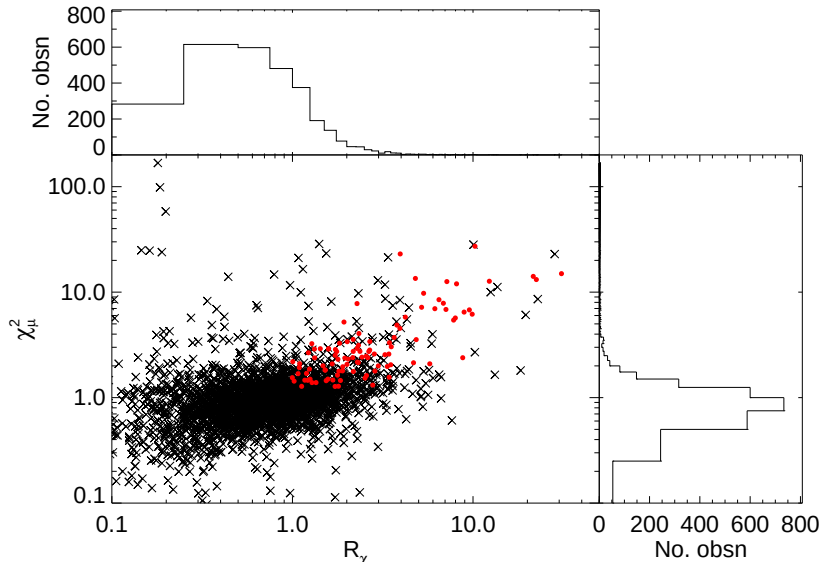


**Figure 4.5:** $\chi^2_\mu$ versus $R_\chi$. Red filled circles indicate those observations with time-variable SWCX signatures (the SWCX set). The remaining points are shown by the black crosses. Histograms of the $\chi^2_\mu$ and $R_\chi$ values are shown in the side panels (using a bin size of 0.25).

Snowden (2008), and described in Chapter 2). For higher intensity soft-proton flares, the slope of the power law becomes flatter. Therefore the higher energy and wider continuum will have a greater variance than the softer, narrower line-band due to the presence of unfiltered residual soft protons. The mean $\chi^2_\mu$ value is 1.77, signifying that the observed distribution is skewed towards higher $\chi^2_\mu$ values rather than distributed about 1, which would have been expected had there been no influence of a deviation (SWCX-enhancements) over the whole data sample.

A scatter plot of $\chi^2_\mu$ versus $R_\chi$, and histograms for each parameter, are given in Figure 4.5. Those observations exhibiting both high $\chi^2_\mu$ and high $R_\chi$ but that do not show clear SWCX signatures (i.e. an enhancement in the mean-adjusted line-band lightcurve compared to that of the continuum) are not considered as part of the SWCX set. These observations corresponded to observations with highly-variable soft proton flares.

The top 10 observations as ranked by $\chi^2_\mu$ are given in Table 4.1 (including comets but ex-

**Table 4.1:** Highest ranked observations by $\chi^2_\mu$ for the SWCX set observations or comets within the whole data set. Those observations with severe residual soft proton contamination have been excluded.

| Revn. | Obsn. | $\chi^2_\mu$ | Comment |
|---|---|---|---|
| 0369 | 0103461101 | 856.7 | Comet C2000 WM1 (LINEAR) |
| 0808 | 0164960101 | 226.6 | Comet C2001 Q4 (Neat) |
| 0342 | 0085150301 | 27.2 | Paper I & Carter et al. (2010) |
| 0209 | 0093552701 | 23.0 | Paper I |
| 1014 | 0305920601 | 15.0 | Paper I |
| 0690 | 0149630301 | 14.1 | Paper I |
| 0623 | 0150610101 | 13.5 | Paper II |
| 1177 | 0406950201 | 13.3 | Comet 73p |
| 0339 | 0054540501 | 13.2 | Paper II |
| 0422 | 0113050401 | 12.7 | Paper II |

cluding those observations that had been rejected from consideration). Three of these top ten result from cometary observations, four were identified in the work presented in Paper I and the remaining cases were presented in Paper II. Many of the highest ranked cases had previously been identified in the literature. All SWCX-set cases as ranked by $\chi^2_\mu$ are listed in the Appendix, Table A-1.

## 4.7 Multiple pointings of target fields

Multiple pointings towards the same target allow one to compare diffuse and extended emission spectral models that may exhibit spectral variations indicative of SWCX contamination. The long term enhancements of the ROSAT all-sky maps, which were subsequently attributed to SWCX, were first identified by comparisons between fields (Snowden et al., 1995). Kuntz & Snowden (2008) examined multiple XMM-*Newton* observations of the *Hubble* Deep Field, amongst other targets, and identified a proportion of their set affected to different degrees by SWCX emission. Bautz et al. (2009) inferred SWCX-enhancements in observations by *Suzaku* towards the cluster Abell 1795 after examination of a low-energy lightcurve revealed peaks coincident in time with enhancements in the solar wind proton flux as measured by

ACE. Henley & Shelton (2010) used a large set of XMM-*Newton* observations to compare intensities from O VII and O VIII lines from sets of observations with the same target pointings. They find no universal association between enhanced SWCX emission and the closeness of the the line-of-sight to the subsolar region of the magnetosheath. We do see a tendency for XMM-*Newton* to be clustered around the subsolar region for the SWCX cases and this is discussed in Section 5.1.

## 4.8 Comets and planets within the dataset

Several XMM-*Newton* observations of comets were included in the overall sample of 3012 observations. The $\chi^2_\mu$ and $R_\chi$ values for the comets are given in Table 4.2. The highest overall values of $\chi^2_\mu$ and $R_\chi$ occurred during observations of comets. Example line-band and continuum lightcurves from comet C2001 Q4 (Neat) (observation 0164960101) are shown in Figure 4.6, where the line-band lightcurve clearly dominates and is highly variable. Also, an earlier observation of the same comet exhibited very different values of $\chi^2_\mu$ and $R_\chi$. Although the solar wind proton flux from the upwind solar wind monitor ACE (level 2, combined instrument data set using the Solar Wind Electron Proton Alpha Monitor (SWEPAM), McComas et al. 1998), also shown in this graph, is steady and not remarkable in intensity, the comet will more likely be sampling solar wind that originates from a different location in the solar corona. The $O^{7+}$ to $O^{6+}$ ratio, as measured by ACE, is also shown in the figure, which shows a similarly unremarkable pattern. A more complete discussion of cometary X-ray emission is beyond the scope of this thesis.

We include within the SWCX set (103 cases) an observation of the planet Saturn, taken on $1^{st}$ October 2002. This observation has been comprehensively analysed by Branduardi-Raymont et al. (2010) who attribute the X-ray flux to emission from the planetary disk, produced by the scattering of solar X-rays and an additional fluorescence emission line of oxygen at

**Table 4.2:** XMM-*Newton* observations of comets within the whole data set.

| Revn. | Obsn. | Name | $\chi^2_\mu$ | $R_\chi$ |
|---|---|---|---|---|
| 0209 | 0103460901 | McNaught-Hartley | 1.5 | 1.0 |
| 0369 | 0103461101 | C2000 WM1 (LINEAR) | 856.7 | 299.9 |
| 0719 | 0161760101 | Comet 2p (Encke) | 2.0 | 1.5 |
| 0720 | 0113041301 | C2001 Q4 (Neat) | 1.2 | 0.9 |
| 0808 | 0164960101 | C2001 Q4 (Neat) | 226.6 | 349.77 |
| 1177 | 0406950201 | Comet 73p | 13.3 | 17.2 |

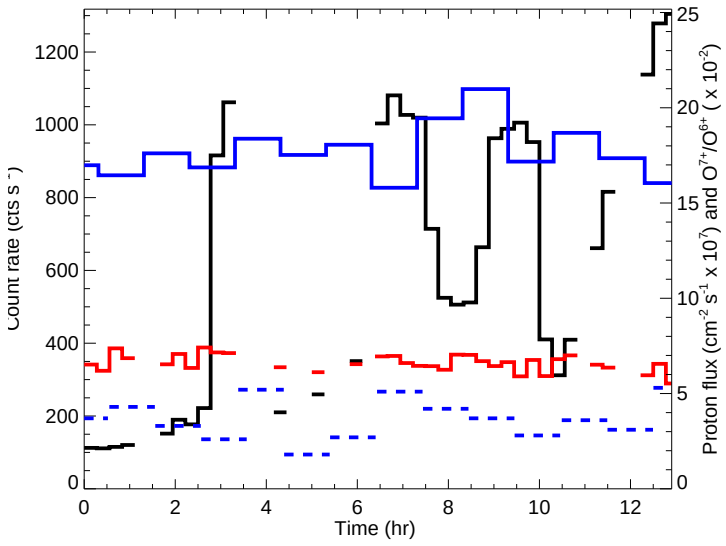


**Figure 4.6:** Lightcurves from comet C2001 Q4 (Neat) that resulted in the highest $\chi^2_\mu$ values (black - line-band, red - continuum band). The time axis is given in hours since the start of the XMM-*Newton* lightcurves. The solar wind proton flux as recorded by ACE (SWEPAM instrument) is given in blue. The $O^{7+}$ to $O^{6+}$ ratio is plotted using the proton flux axis and is shown by the blue dashed line.

$\sim$0.53 keV originating from the rings (also described in Section 3.4.2). This observation was previously studied by Ness et al. (2004) but was not investigated for any low-energy variability. We find a high $\chi^2_\mu$ (2.9) and $R_\chi$ (2.3) in our time variability test and a distinct step in the line-band lightcurve, indicative of a SWCX enhancement, after the same filtering steps as to all other data sets have been applied, including source exclusion to remove emission from the planet and planetary exosphere. The initial source exclusion radius equates to $\sim 3.7 R_{Saturn}$. Spectra from this observation were extracted from event files that had been additionally filtered with a larger extraction region of $\sim 10.6 R_{Saturn}$ (see Chapter 6). Even after this additional source extraction step the lightcurve production procedure yields metrics of $\chi^2_\mu$ and $R_\chi$ of 3.1 and 2.4 respectively. Two later observations of Saturn taken in 2005 were included within our sample but neither showed evidence of a SWCX enhancement. Therefore, we have no reason to reject this observation (from 2002) from the SWCX set. We were concerned that the planet's movement through and possibly out of the FOV may have caused the low-energy variability. However, the dominant movement is in right ascension with a maximum speed of 8 arcseconds per hour (Branduardi-Raymont et al., 2010), resulting in a shift of only 0.7 arcminutes over the course of the $\sim$18 ks exposure. In addition, resolved point sources have been removed from the FOV as for all other observations.

## 4.9 Summary

We have flare-filtered a large sample of data from the XSA, which was then additionally cleaned to remove resolved point sources in the FOV. A method was applied to identify those observations within the data sample that exhibit signatures of time-variable SWCX. This method identifies fluctuations in a low-energy band, not seen in comparison with a higher-energy band. The strongest indicators of time-variable SWCX originated from comets but these have been omitted from the final selected SWCX set. We also omit those SWCX

observations that have been comprehensively investigated in the literature yet show no temporal variability in our tests. This set of observations which we have used for further study throughout is hereafter known as the SWCX set and comprises 103 observations. The SWCX set observations are analysed in the following chapters.

Chapter 5

# SWCX set XMM-Newton orbital positions and relationship with the solar cycle

We discuss the overall characteristics of the SWCX set observations with respect to the positions of XMM-*Newton* in orbit about the Earth and consider the influence of the solar cycle on the incidence of detected exospheric-SWCX.

## 5.1 Orbital positions

In Figure 5.1 we plot both the total number of observations analysed for the whole data set and the fraction of these observations that belong to the SWCX set (the fractional values), versus the GSE-X position of XMM-*Newton* at the mid-point of each observation. We can see from this figure that XMM-*Newton* is preferentially found on the subsolar side of the Earth (sunward side of the magnetosheath) when SWCX enhancements occur, although there are also a non-negligible number of cases anti-sunward. Therefore, there is a high enough neutral density on the anti-sunward side of Earth for charge exchange to occur along lines-of-

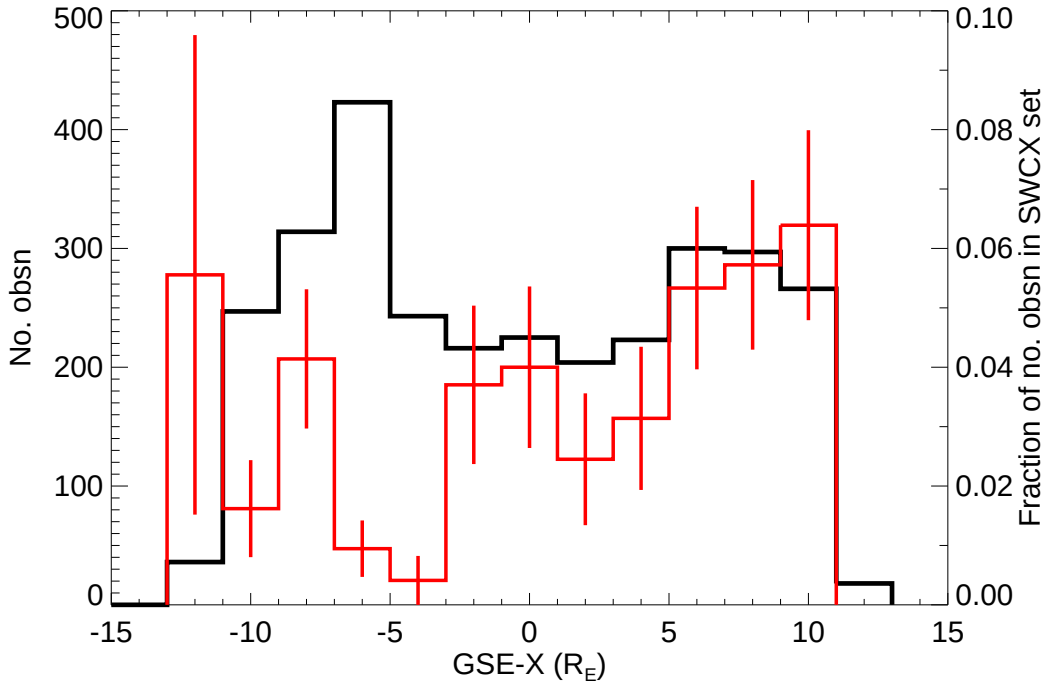


**Figure 5.1:** Total number of observations analysed (black) versus GSE-X position and the fraction of observations detected with exospheric SWCX enhancements (red). Poissonian errors on each fractional value are also shown (red vertical bars).

sight that originate in this region. Comparing the fractional values to a flat distribution based on the mean value, we calculated a reduced $\chi^2$ of 9.7 (with 12 degrees of freedom), implying that the distribution of fractional values observed is highly significant. The anti-sunward bin with the highest fraction of SWCX-set observations occurs where there are only a small number (36) of observations analysed (between -11 and -13 $R_E$). In addition, the peak of the fractional distribution, which occurs in a bin with a large number of observations analysed, occurs around the nominal magnetopause standoff distance at approximately 10 $R_E$. The XMM-*Newton* line-of-sight for these cases traversed the subsolar region, which is the region of maximum expected exospheric SWCX emissivity, according to the modelling work of Robertson et al. (2006) (and as shown in Chapter 3). As previously described in Section 3.5 the viewing of XMM-*Newton* is constrained by the fixed solar panels and limits imposed to avoid directly observing the Sun, Moon and Earth and the observatory is only able to view the sunward side of the magnetosheath at certain times of the year.

## 5.2 Relationship with the solar cycle

In the upper panel of Figure 5.2 we plot the solar sunspot number[1] from the latter half of Solar Cycle 23, which can be used as a measure of solar activity. A simple six-month split of the SWCX set observations showed that 64 SWCX cases occurred during period 1 (April until September inclusive) and 39 occurred during period 2 (October until March inclusive). However, a simple six month split does not account for the change in the orbit of XMM-*Newton* as described in Chapter 3. We plot a histogram of the number of SWCX cases per half year, to remove any bias resulting from the seasonal constraints on pointing angle experienced by XMM-*Newton*. Each histogram bin starts at the start of 'summer' or the start of 'winter'. We define the start of summer as the mid-way point between the previous minimum and maximum in the GSE-X coordinate of the apogee positions for that year, to account for the precession and the change of orbit as experienced by XMM-*Newton* and described in Section 3.5. The start of winter is defined similarly as the mid-way point between high summer (maximum in the GSE-X apogee coordinate) and the following mid-winter (minimum in the GSE-X apogee coordinate). These maxima and minima in GSE-X coincide with the transition from negative to positive GSE-Y coordinate values. The apogee and perigee maxima dates and times are given in Table 5.1. We only had access to orbit information from June 2000 up until March 2009. For the 1999 perigee value we assumed that no precession had taken place and fixed our first bin six months prior to the mid summer value of 2010. Similarly for the 2009 perigee value we have based the interval on the step in time between apogee and perigee for the years 2007 and 2008. Overall, the 'summer/winter' split is 59:44 accounting for precession. As expected for cases of exospheric SWCX, there are more cases at times of high solar activity around solar maximum than when approaching solar minimum. We investigate the relationship between the observed SWCX flux versus the solar wind proton flux in Section 6.4 as we consider this a better probe of the state of the solar wind state

[1] http://www.sidc.be/index.php

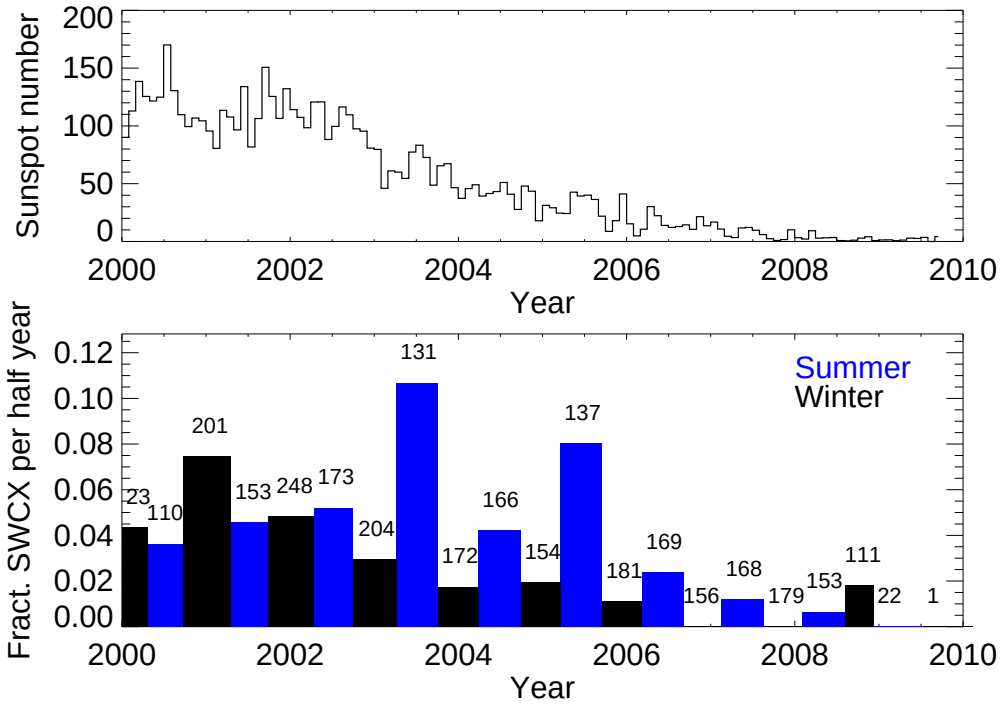


**Figure 5.2:** Top panel: sunspot number versus time. Bottom panel: the coloured histogram of the fraction of observations affected by exospheric SWCX is binned into 'summer' and 'winter' periods (blue - summer, black - winter). The total number of all observations for each period is noted above the bin.

and type of wind experienced in the vicinity of the Earth on a case-by-case basis. Also, for the cases from 2002 onwards and approaching solar minimum until 2009, we see a higher proportion of SWCX cases in the summer six-month period compared to the winter period for the same year, although this is barely discernible for the most recent years. This is not true however for 2009 and this trend should not be overstated due to the low number of cases in each bin.

## 5.3 Sky pointings and the helium focusing cone

As described in Chapter 3, the Solar System helium focusing cone is found downstream of the Sun's motion through the Local Interstellar Cloud. In Figure 5.3 we plot a trace of Earth's orbit in the region of the helium focusing cone and mark the positions at which observa-

**Table 5.1:** XMM-*Newton* orbit apogee and perigee GSE-X maxima dates (mid summer and mid winter). The GSE-Y coordinate at these times is zero.

| Year | Date apogee maximum | Date perigee maximum |
|---|---|---|
| 1999 | - | 2000-01-11T22:48:00 |
| 2000 | 2000-07-13T21:37:39 | 2000-12-31T09:14:06 |
| 2001 | 2001-07-13T22:23:21 | 2001-12-31T12:44:54 |
| 2002 | 2002-07-10T01:43:21 | 2002-12-31T14:26:15 |
| 2003 | 2003-07-06T02:33:37 | 2003-12-31T14:31:10 |
| 2004 | 2004-06-27T02:45:49 | 2004-12-24T14:48:59 |
| 2005 | 2005-06-17T03:16:43 | 2005-12-12T15:28:35 |
| 2006 | 2006-06-05T03:50:43 | 2006-11-28T16:06:03 |
| 2007 | 2007-05-18T04:34:48 | 2007-11-12T16:36:50 |
| 2008 | 2008-04-29T05:14:20 | 2008-10-20T17:19:49 |
| 2009 | 2009-04-10T07:00:11 | 2009-10-10T17:19:49 |

tions within the SWCX set occur. We also show the pointing directions of the observations. Very few observations occurred in the region of the helium focusing cone. We discuss these observations further in Chapter 8 Section 8.5, but to summarise here we find no evidence to suggest that temporal variability originating in the helium focusing cone significantly affected the SWCX set.

## 5.4 Summary

We have looked at the overall characteristics of the SWCX set in terms of XMM-*Newton* orbital positions. We have shown that SWCX cases preferentially occur when XMM-*Newton* has a line-of-sight that intersects the subsolar region of the Earth's magnetosheath and when solar activity is highest. In the next chapter we will produce spectra for each SWCX case and investigate the relationship between sample line ratios and between the observed flux and the solar wind at the time of the observations.

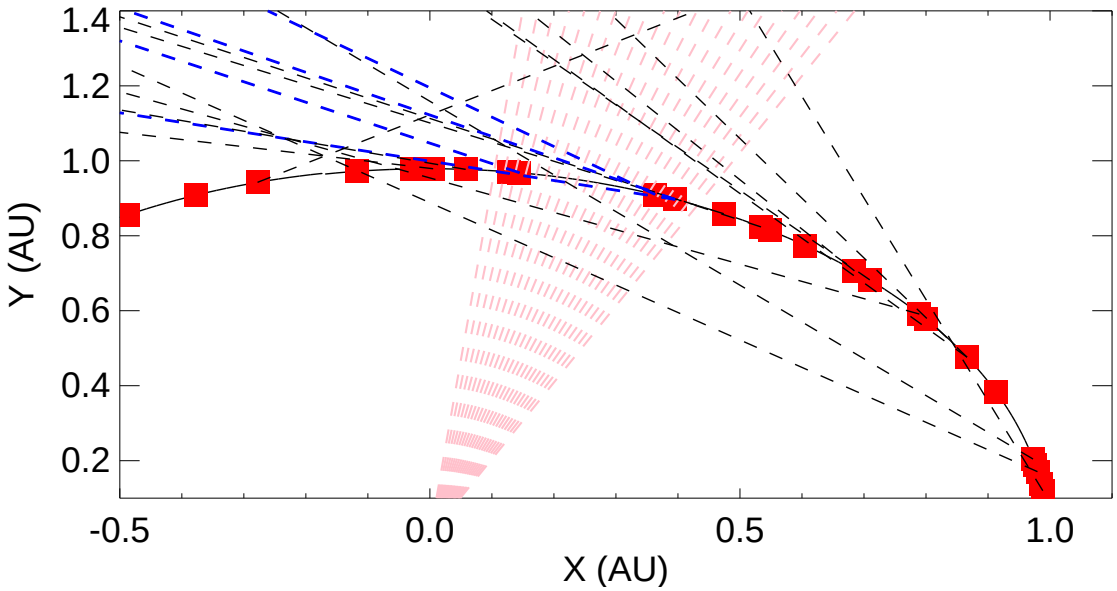


**Figure 5.3:** Plot in the Ecliptic plane showing the pointings directions of XMM-*Newton* for those SWCX set observations that occurred near the helium focusing cone. The position of Earth for these cases is shown by the red squares. The helium focusing cone area is marked by the area of pink dashed lines (10° in longitude either side of the pointing direction of (73.9°, -5.6°) in ecliptic longitude and latitude projected onto this plane. Only those pointing directions that intersect the helium focusing cone are plotted, given by the dashed lines (black, or blue for the cases when XMM-*Newton* is found inside the helium focusing cone).

Chapter 6

# Spectral analysis of the SWCX set

We continue our study by analysing the spectral signatures of the SWCX cases. We examine the implied fluxes of a standard model applied to each case, the line ratios between pairs of specific ion species and present a combined exospheric-SWCX spectrum.

## 6.1 Spectral extraction

XMM-*Newton* SAS software (version 9.0.0) was used to produce spectral products and instrument response files for all observations of the SWCX set. The SAS accesses instrument calibration data in so-called current calibration files (CCFs) which are generally updated separately from SAS release versions. In this work we used the public CCFs released as of February 2010.

For each exospheric-SWCX case we extracted spectra for the EPIC-MOS cameras for the suspected SWCX-affected period and for the suspected SWCX-free period from the event files that had previously been cleaned for high soft-proton contamination, as described in Chap-

ter 4. The SWCX-affected period was when the enhancement in the line-band lightcurve was judged (however not by a formal mathematical argument) to have occurred. The enhancement could have occurred at the beginning, middle or end of the observation. One case had two periods that contributed to the SWCX-affected spectrum, taken from both the beginning period and latter period of the observation. The remaining time periods in the observation made up the SWCX-free period. We used events from a circular extraction region, centred on detector coordinate positions (DETX, DETY = -50, -180), with an extraction radius of 16000 detector units or 13.3 arcminutes. We also applied the flag and pattern selection expression '#XMMEA_EM&&PATTERN<=12&&FLAG==0'. This pattern selection selects events within the whole valid X-ray pattern library for the EPIC-MOS and the flag selection removes events from or adjacent to noisy pixels and known bright columns. We produced instrumental spectral response files for each period. The instrument effective area files were calculated assuming the source flux is extended, filling the field of view and with no intrinsic spatial structure.

We knew from the work of Carter et al. (2010) (the subject of Chapter 7) that exospheric SWCX can occur throughout the entirety of an observation, although the line-band lightcurve may show an enhanced and a steady-state period. We used the spectra from the apparent SWCX-affected period as the source spectra and that from the apparent SWCX-free period as the background. This background-subtracted spectrum (hereafter referred to as the resultant spectrum) therefore provides a lower limit to the SWCX enhancement that has occurred during an observation. Providing the particle-induced background is reasonably constant over the duration of the observation (at most $\pm$10%, De Luca & Molendi 2004) this background component will be eliminated. An inspection of the resultant spectra was made for energies above 2.5 keV, to check for the presence of significant variable residual soft-proton contamination. Each SWCX-case showed a count rate statistically consistent with zero above this energy.

**Table 6.1:** Principal ion species emission lines used in the spectral model, plus any minor transitions emission line energies used.

| Ion | Energy (keV) | Minor energies (keV) |
|---|---|---|
| C V | 0.299 | 0.304, 0.308, 0.354, 0.379 |
| C VI | 0.367 | 0.436, 0.459, 0.471 |
| N VI | 0.420 | 0.426, 0.431, 0.523 |
| N VII | 0.500 | 0.593, 0.625, 0.640, 0.650 |
| O VII | 0.561 | 0.569, 0.574, 0.713, 0.666, 0.698, 0.723 |
| O VIII | 0.653 | 0.775, 0.817, 0.837, 0.849 |
| Ne X | 1.022 | |
| Mg XI | 1.330 | |
| Si XIV | 2.000 | |

## 6.2 Spectral model

We modelled the resultant spectrum for each SWCX case with a standard model of emission lines (with no absorption along the line-of-sight). The spectra from MOS1 and MOS2 were fitted simultaneously, although a global normalisation parameter for the MOS2 spectrum relative to the MOS1 was allowed to vary. The relative line strengths for a particular ion species below 1 keV, for example O VII (which involves seven separate transitions including the O VII triplet), were set using the velocity dependent cross-sections of compiled theoretical charge exchange collisions between highly charged ions and atomic hydrogen, as found in Bodewits et al. (2007). We assumed a solar wind speed of 400 $\mathrm{km\,s^{-1}}$ for these cross-sections. We also added emission lines from Ne X at 1.022 keV, Mg XI at 1.330 keV and Si XIV at 2 keV. There may be emission from other ion species present in the spectra, such as from highly charged iron or aluminium (as seen in Carter et al. (2010) and described in Chapter 7), but we wished to simplify the model applied to a general case and the dominant SWCX emission lines are found below 1 keV. We fixed the relative normalisations of the minor transitions to that of the principal transition for each ion species. The principal, dominant transition in the case of the helium-like C V, N VI and O VII is the forbidden line transition. The principal ion and minor transitions used in this modelling are listed in Table 6.1.

## 6.3 Whole band flux

We used Version 12.5.0 of the XSPEC X-ray spectral fitting package to perform this analysis. We fitted the model to each resultant spectrum by minimising the $\chi^2$ statistic. We calculated the modelled flux and 1-sigma errors on the flux between 0.25 and 2.5 keV for each EPIC-MOS instruments. The keyword giving the area collected in the spectral extraction (BACKSCAL) was converted into units of steradians and used to convert the individual flux values to units of $\mathrm{keV\,cm^{-2}\,s^{-1}\,sr^{-1}}$. Fluxes presented here onwards are for a combined error-weighted average EPIC-MOS flux. The error on the flux was calculated from the individual flux errors, combined in quadrature. A histogram of the total spectrally fitted flux for each of the SWCX set can be seen in Figure 6.1. The minimum flux we observed for a SWCX case was $2.2\,\mathrm{keV\,cm^{-2}\,s^{-1}\,sr^{-1}}$ (observation id. 0112490301) and the maximum $50.1\,\mathrm{keV\,cm^{-2}\,s^{-1}\,sr^{-1}}$ (observation id. 0085150301, Carter et al. 2010). The mean value of $15.4\,\mathrm{keV\,cm^{-2}\,s^{-1}\,sr^{-1}}$ is reasonably close to the value ($\sim$$8.8\,\mathrm{keV\,cm^{-2}\,s^{-1}\,sr^{-1}}$) under nominal solar wind conditions of Robertson & Cravens (2003b), given that the SWCX set sample contains results from many different input solar wind conditions and viewing orientations.

## 6.4 Line flux ratios

The relative strengths of the component lines to the SWCX spectral model varied considerably within the SWCX set. Individual line fluxes were calculated by finding the best fit model using all lines, as described above, then setting other line normalisations to zero in XSPEC. The flux for the individual ion species contribution was calculated in the range 0.25 to 2.5 keV.

High $O^{7+}$ to $O^{6+}$ and magnesium to oxygen ion ratios are used as indicators of the presence

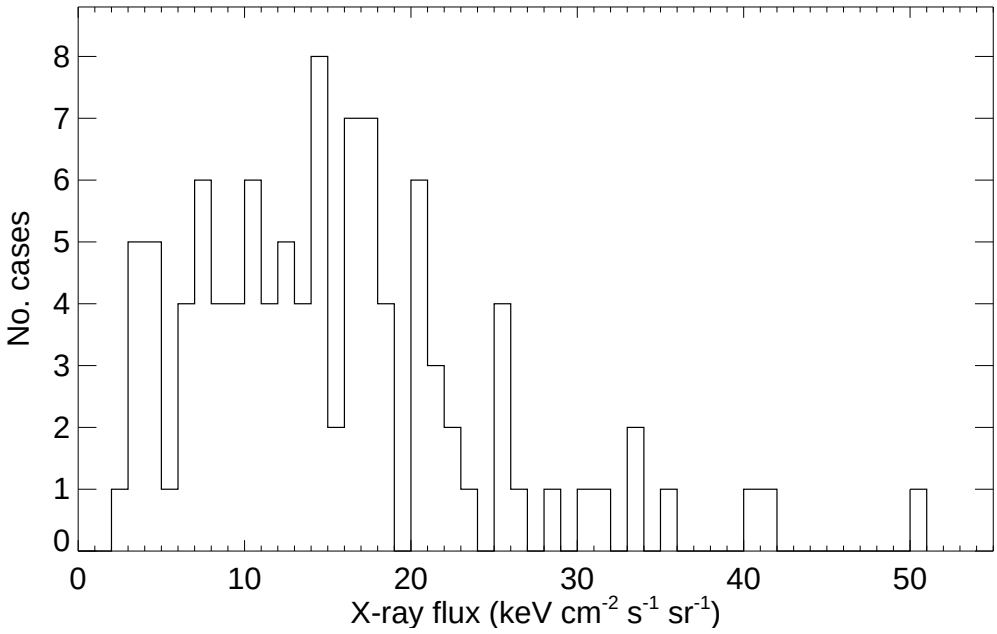


**Figure 6.1:** Histogram of total spectrally fitted flux between 0.25 and 2.5 keV for the SWCX set resultant spectra.

of CME plasma (Zhao et al., 2009; Richardson & Cane, 2004; Zurbuchen & Richardson, 2006). O VII line emission, resulting from an incoming solar wind $O^{7+}$ ion gaining an electron through charge exchange to become $O^{6+}$, is the dominant component to the SWCX emission in the majority of cases. In Figure 6.2 we plot the ratio of the fluxes of the lines Mg XI/O VII versus O VIII/O VII (using all those oxygen transitions available to us within our X-ray spectral band). To look for plasma signatures with the highest charge states we only plot those cases where the normalisation of the numerator in the ratio is well constrained. Three observations are constrained to have both a ratio of Mg XI/O VII $> 0.6$ and O VIII/O VII $> 1.0$. One of these (with identifier 0085150301) was an observation with emission assigned to a passing CME and described in Carter et al. (2010) and Chapter 7. These observations are listed in Table 6.2 and are therefore possible candidates when XMM-*Newton* may have observed CME plasma. We quote the lower limit to the ratio in the case where the O VII flux is badly constrained, i.e. very weak. In this table we also quote the mean value of the $O^{7+}$ to $O^{6+}$ ratio during the period of the observation, using values taken from the ACE SWICS instrument (Gloeckler et al., 1998). This data was only available in two of the cases in the

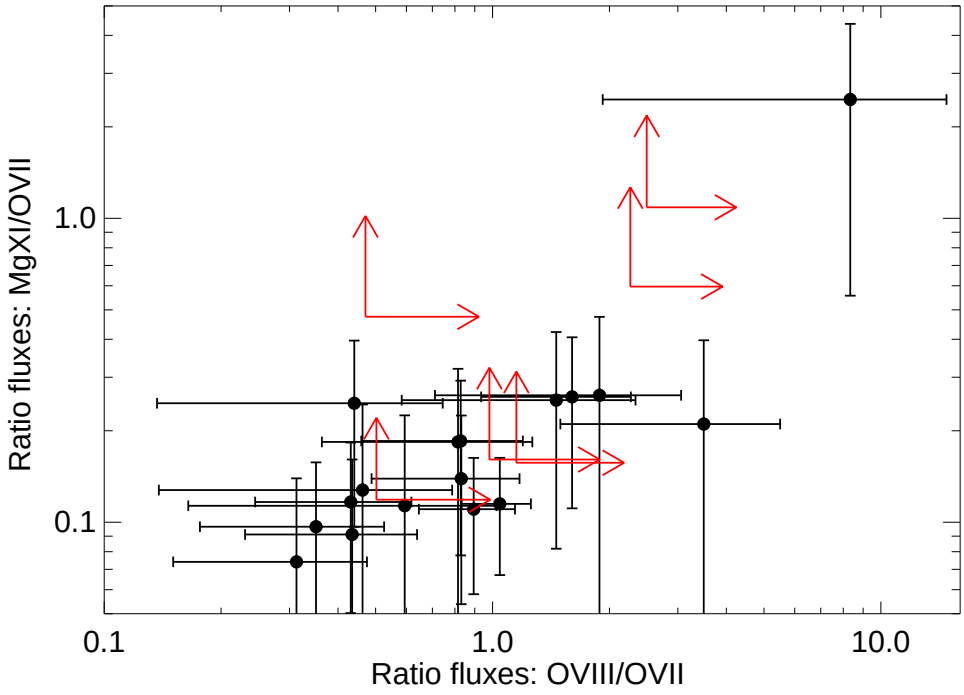


**Figure 6.2:** Plot of the flux ratios of Mg XI/O VII versus O VIII/O VII where available for the SWCX set. Where appropriate we mark the lower limits (red).

table. As ACE is found at Lagrangian point L1, we have time shifted the solar wind data to account for the travel time to Earth, based on the mean speed of the solar protons during the XMM-*Newton* observation and assuming a planar wavefront travelling on the Sun-Earth axis. Expected $O^{7+}/O^{6+}$ ratios for the slow and fast solar wind are 0.27 and 0.03 respectively (Schwadron & Cravens, 2000). Both of the observations with ACE SWICS data surpass both the nominal slow and fast values by a considerable margin and would suggest that ACE detected a CME plasma. Although the identification of CME plasma generally involves many more criteria to be satisfied, XMM-*Newton* could provide supplementary spectral evidence to studies employing in-situ dedicated solar wind monitors in the field of solar system space science.

Using the dominant transition energy for each set of lines that contribute to the O VII and O VIII flux values, we note a mean O VII flux of 6.1 LU and a mean O VIII flux of 4.0 LU. These values are comparable to those presented in the literature review of Chapter 3.

**Table 6.2:** SWCX set observations exhibiting the highest Mg XI/O VII and O VIII/O VII flux ratios, or the lower limit (95% confidence) to this ratio when O VII is badly constrained. We also note the ACE SWICS mean value of the $O^{7+}$ to $O^{6+}$ ion ratio when available, with the standard deviation of this ratio given as the error.

| Revn | Obsn | Mg XI/ O VII | O VIII/ O VII | Mean $O^{7+}/O^{6+}$ |
|---|---|---|---|---|
| 0342 | 0085150301 | 2.5±1.9 | 8.3±6.4 | 0.58±0.54 |
| 0494 | 0109120101 | ≥0.60 | ≥2.26 | 1.53±0.83 |
| 0747 | 0200730401 | ≥1.09 | ≥2.49 | ... |

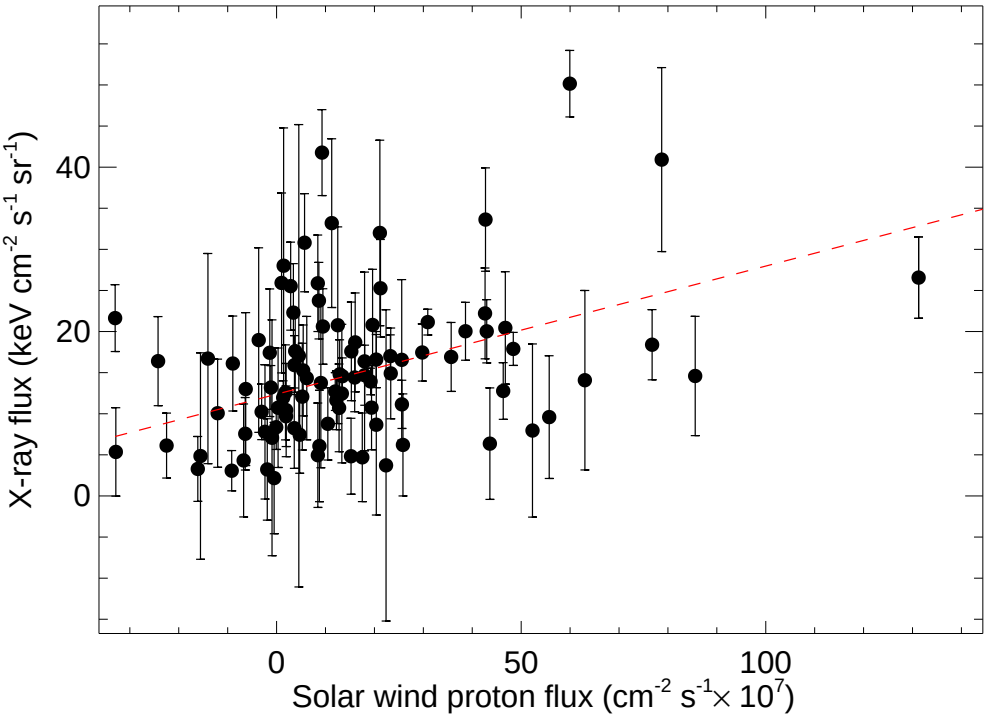


**Figure 6.3:** Observed flux versus mean solar wind proton flux. The red dotted line indicates a linear fit (minimising the $\chi^2$ statistic) to the data.

To test if any relationship exists between the flux of the SWCX lines and increased solar wind flux, we plot in Figure 6.3 the observed flux versus the difference in the mean solar wind proton flux (as measured by ACE when data was available) between the SWCX-affected and SWCX-free periods. We have again time-shifted the ACE data to account for the distance between L1 and the Earth. Although there is considerable scatter amongst these values, there is a positive correlation between line flux and solar wind proton flux. We include the linear fit, calculated by minimising the $\chi^2$ statistic, in the plot. This linear fit was added primarily to aid the eye however, the fit has a correlation coefficient of 0.35 but with a very low probability ($\sim$2%) of obtaining a test statistic at least as extreme as that observed here, reflecting the amount of scatter seen in the data. There are 73 out of 95 cases (the total number of cases when ACE data was available), that exhibited a positive resultant mean solar wind proton flux. Under the null hypothesis that the resultant mean solar wind proton flux is equally likely to be negative or positive, the probability of the observed outcome is only $\sim 7.3 \times 10^{-8}$. Therefore, an elevated solar wind proton flux, for our SWCX set, is a good indicator of the presence of a SWCX-enhancement, if not the level of this enhancement. This is in contrast with the results of Henley & Shelton (2010), whose SWCX cases were considered to be due to SWCX occurring within the heliosphere and therefore no correlation would be expected between an upstream solar wind monitor and any SWCX enhancement. Examples of proton lightcurves are given in Figure 6.4. Heliospheric SWCX is expected to vary on longer timescales than exospheric SWCX and therefore will be harder to identify by the technique described in this work. However, at certain times of the year XMM-*Newton* may have a line-of-sight that passes through the helium focusing cone, that could potentially produce a variable signal in the line-band that may be detectable by this technique (variations over a few hours, Koutroumpa et al., 2007). We discuss this possibility further in Section 8.5. We assume hereafter that the flux variations seen within our SWCX set are due to local X-ray emission in the vicinity of the Earth.

**Table 6.3:** Most prominent ion line fluxes for example cases. Fluxes are quoted in units of $\mathrm{keV\,cm^{-2}\,s^{-1}\,sr^{-1}}$. Upper limits (95% confidence) are given for very weak lines.

| Revn | Obsn | C VI | N VI | O VII | O VIII |
|---|---|---|---|---|---|
| 0623 | 0150610101 | 4.86±1.10 | 2.19±1.48 | 7.73±0.37 | 2.42±0.61 |
| 0339 | 0054540501 | 5.61±0.85 | ≤3.50 | 11.73±0.27 | 4.74±0.41 |
| 0422 | 0113050401 | 9.05±0.41 | ≤2.80 | 11.60±0.27 | 4.36±0.46 |

## 6.5 Example cases of SWCX enhancement

In this section we comment on three of the exospheric cases from Table 4.1. Individual fluxes for a selection of prominent lines are given for each in Table 6.3. Lightcurves for each, over-plotted with the solar proton flux as recorded by ACE, are given in Figure 6.4. The solar proton lightcurves have been adjusted for the distance between ACE and the Earth as before. We also plot a resultant spectrum for each observation by combining data from both EPIC-MOS cameras and over-plot the best fit model to the data as previously found for each case and as described in Section 6.1.

- observation 0150610101 (revolution 0623), see Figure 6.4 (top)

  The line-band lightcurve shows a period of enhanced count rate at the beginning of the observation. The ACE solar proton flux is raised at the beginning of the lightcurve and reduces as the lightcurve progresses. The resultant spectrum exhibits emission at O VII, O VIII, along with evidence of carbon emission below 0.5 keV. The flux observed between 0.25 and 2.5 keV was $20.6\,\mathrm{keV\,cm^{-2}\,s^{-1}\,sr^{-1}}$;

- observation 0054540501 (revolution 0339), see Figure 6.4 (middle)

  The line-band lightcurve shows an enhancement during the latter part of the observation, which is also observed in the ACE solar proton flux. The resultant spectrum exhibits emission in the oxygen band, along with evidence of carbon emission below 0.5 keV. The flux observed between 0.25 and 2.5 keV was $41.8\,\mathrm{keV\,cm^{-2}\,s^{-1}\,sr^{-1}}$;

- observation 0113050401 (revolution 0422), see Figure 6.4 (bottom)

  The line-band lightcurve shows a period of enhanced count rate at the beginning of the observation. A short enhancement period is seen in the ACE solar proton flux and the overall magnitude of this flux is much higher than the other two cases in this section. The flux observed between 0.25 and 2.5 keV was 25.9 keV $cm^{-2}$ $s^{-1}$ $sr^{-1}$.

## 6.6 Stacked spectra

We combined the SWCX spectra (SWCX-enhanced period) together for each EPIC-MOS instrument to produce one average time-variable SWCX spectrum for MOS1 and MOS2. We also combined the associated background spectra (SWCX-free period), ancillary and detector response files (*arf* and *rmf* files) for each MOS instrument. The resultant background-subtracted spectra are shown in Figure 6.5. We fit a model for the SWCX emission in the energy range 0.25 to 2.5 keV, as in Section 6.2 allowing a global normalisation for MOS2 relative to MOS1 to vary, the result of which is also shown on the plot. The residuals at $\sim$1.48 keV may be due to variations in the particle-induced aluminium fluorescence background line or to real charge-exchange emission from aluminium. There are also clear residuals at $\sim$0.9 keV which may be due to either Fe XIX or Ne IX or a blend of these lines. These additional lines were not included in the general model applied to the whole SWCX set. On adding a line at 0.91 keV (Ne IX) we see an increase in the model flux of 1.3% in the band 0.25 to 2.5 keV, so reason that the addition of this line to the standard model would have a minimal effect on the overall observed flux values quoted in this section.

We used the XSPEC *steppar* command to calculate confidence intervals on the normalisations of the O VII and O VIII major transitions (to which the other minor transitions for each species are tied). A contour plot with contours drawn at 68%, 90% and 99% confidence intervals is

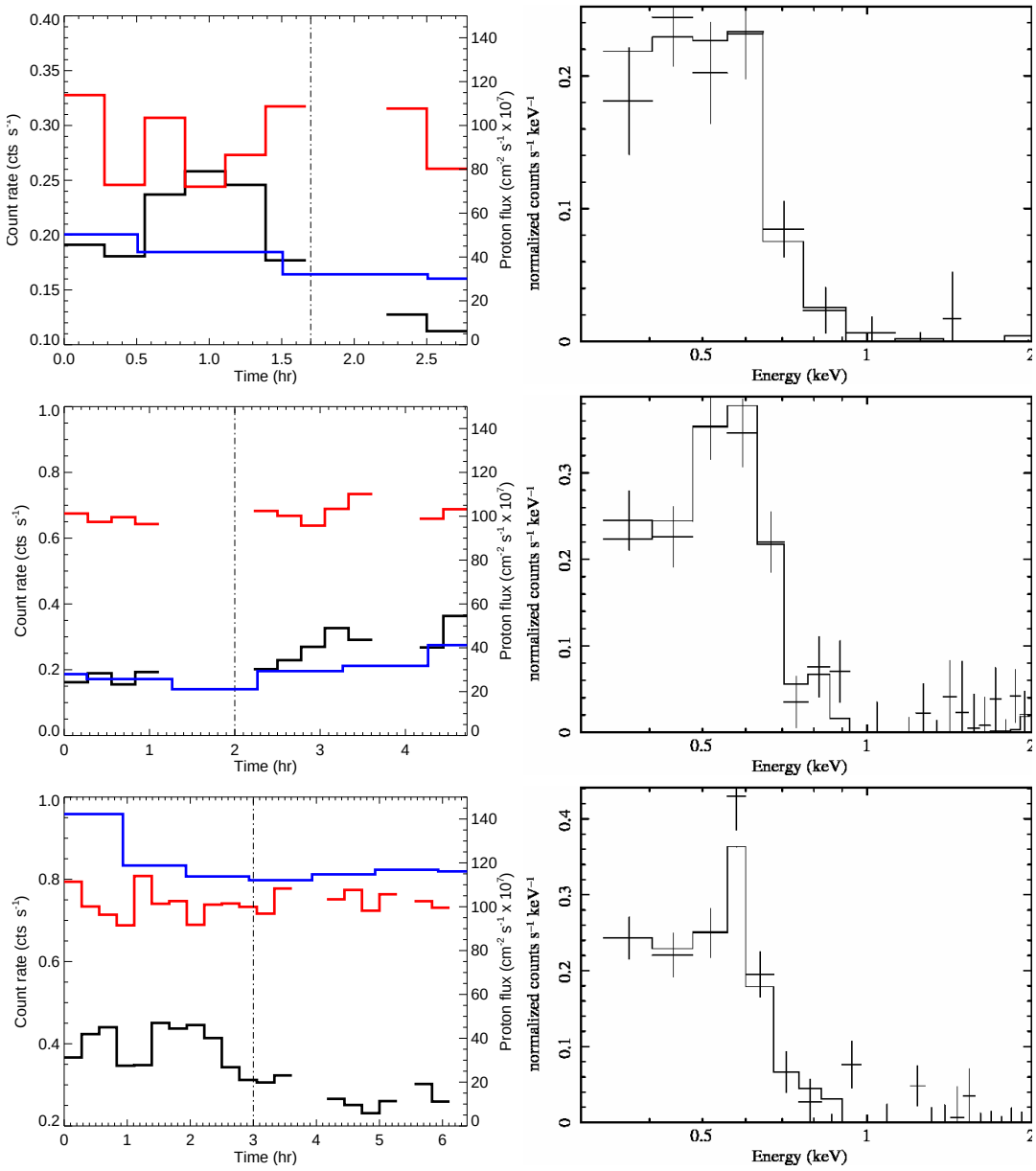


**Figure 6.4:** Example cases of SWCX enhancement, for observations with the identifiers 0150610101 (top tow), 0054540501 (middle row) and 0113050401 (bottom row). Each left-hand panel shows the line-band (black) and continuum band (red) non mean-adjusted lightcurves along with the solar proton flux (blue, right-hand y-axis). The split between the SWCX-free and SWCX-affected period is indicated by the dot-dashed vertical line. In the right-hand panels we show the combined EPIC-MOS resultant spectrum and the model fitted to the data for each case (solid line).

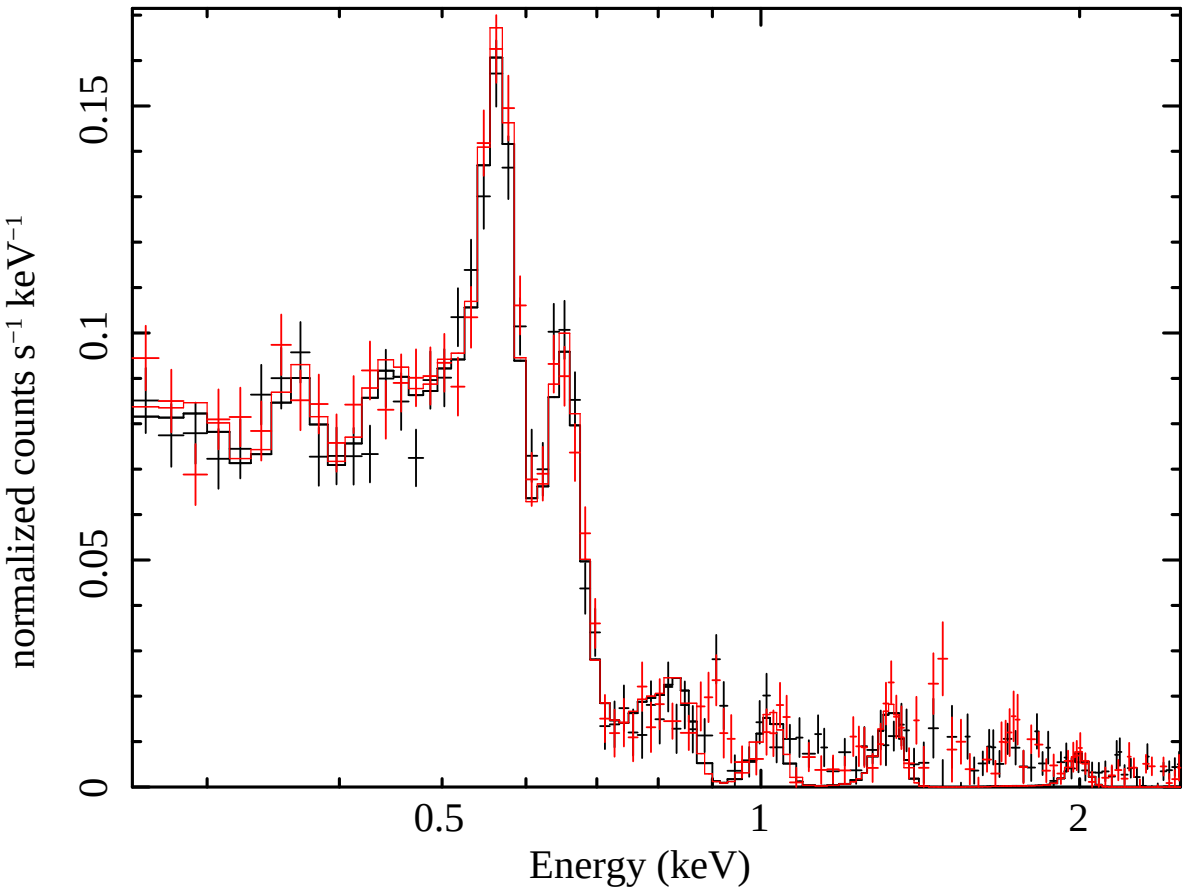


**Figure 6.5:** Stacked SWCX set spectra in the energy range 0.25 to 2.5 keV (the spectrum for MOS1 is shown by the black crosses, the spectrum for MOS2 is shown by the red crosses) and the model fitted to the data (continuous black line).

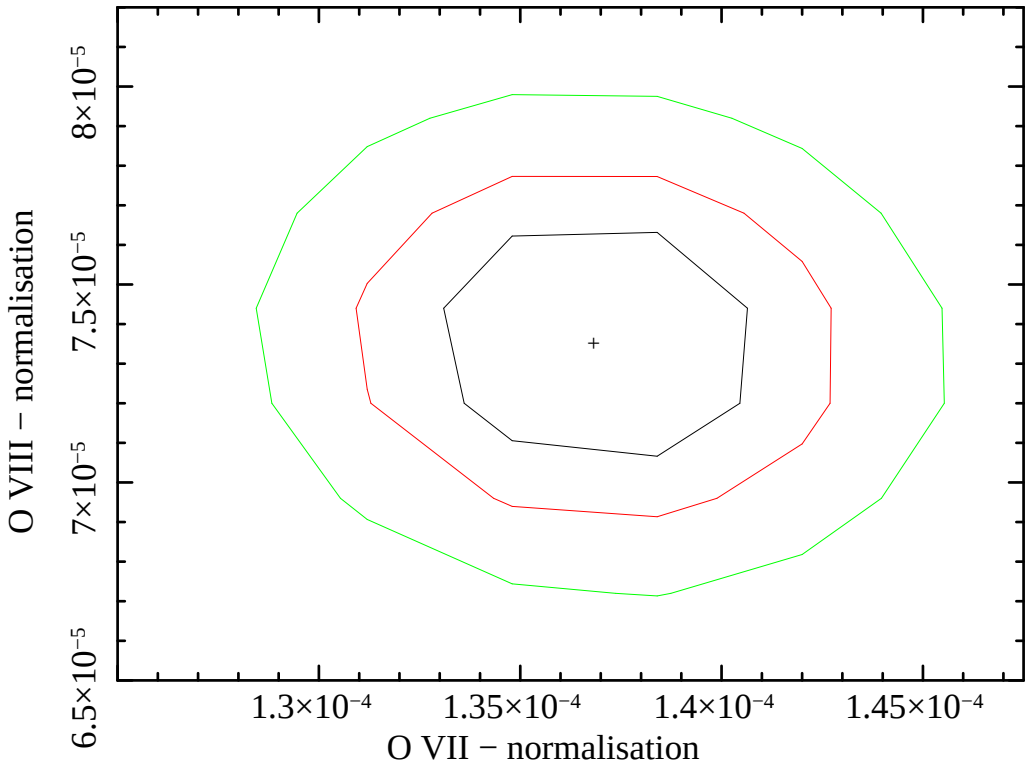


**Figure 6.6:** Contour plot between the O VII and O VIII normalisations (major transitions) for the stacked SWCX spectra (common to both MOS1 and MOS2).

shown in Figure 6.6. The O VII line has a flux of 7.6±0.3 LU, more than double that of the O VIII, line which has a flux of 3.0 ±0.1 LU. It should be noted that the ratio between the O VIII and O VII normalisations for any given observation does not accurately represent the abundance ratio of $O^{8+}$ to $O^{7+}$ found in the solar wind. $O^{8+}$ may charge exchange to produce $O^{7+}$ and then subsequently charge exchange again to $O^{6+}$. This may occur to different extents along the line-of-sight of the observer.

We looked in more detailed at the O VII helium-like triplet. We untied the normalisations of the intercombination (x, y, at 568.6 eV) and resonance lines (w, at 574.0 eV) from that of the forbidden line (z, at 561.1 eV) and fixed the energies. We then re-fit the spectrum in the energy range 0.5 to 0.8 keV. We used the *steppar* command to calculate confidence intervals on

the forbidden line normalisation and that of the resonance line. A contour plot with contours drawn at 68%, 90% and 99% confidence intervals is shown in Figure 6.7 (upper panel). We also show a similar plot for the forbidden line normalisation versus the intercombination line in Figure 6.7 (lower panel). The expected ratio between the resonance and forbidden line normalisations has not be given in the literature. The initial energy level of the resonance line can be populated by many different branching paths from higher order transitions which severely complicates any attempt to calculate this ratio. However, the expected ratio of the forbidden to intercombination lines, assuming an initial population of the triplet state $^3P$ and theoretical transition rates as described in Section 3.1, is 0.7:0.3. We over-plot the line representing the ratio on this second plot, given the normalisation found for the forbidden line. The forbidden line, within the uncertainties in the calibration, is stronger than the resonance and intercombination lines, as expected for a spectrum resulting from charge exchange.

## 6.7 Summary

After applying a standard model to spectra from each observation of the SWCX set, we see a wide range in the value of the total flux and considerable variation in the strengths of individual emission lines. Increases in the solar proton flux, as measured upstream of the Earth by dedicated solar wind monitors, is a reasonable indicator that increased SWCX X-ray flux can be expected. Ratios between certain lines may be useful additional information for solar wind studies for classifying incoming plasma types. For example, the identification of certain ion species within a SWCX spectrum may indicate that a CME has passed in the vicinity of the Earth. A spectrum constructed from a combination of SWCX-set spectra requires the forbidden-line transition of O VII to be the most prominent emission line of the O VII hydrogen-like triplet, as expected from theoretical modelling and laboratory experiments of charge exchange cross-sections.

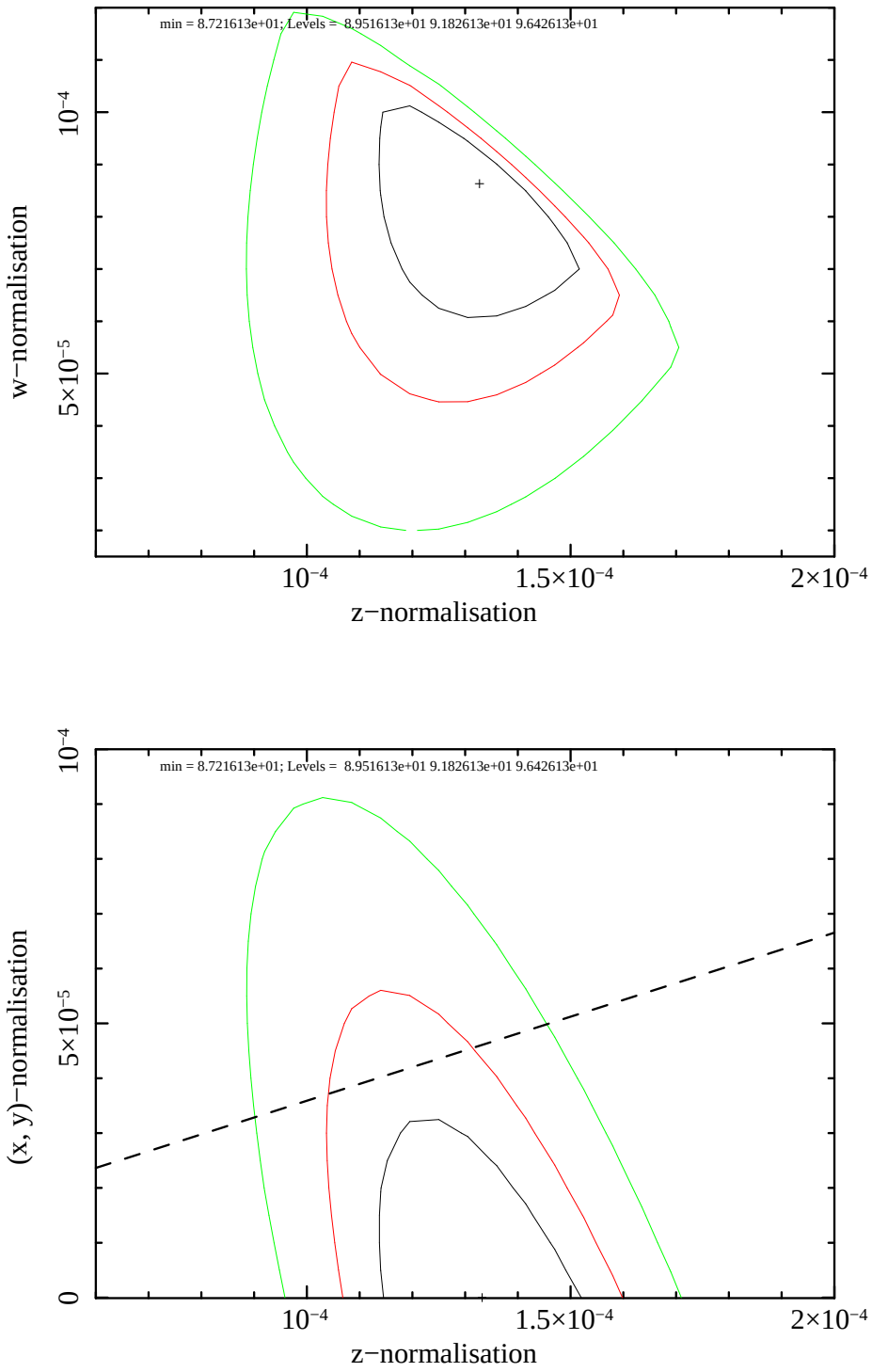


**Figure 6.7:** Upper panel: contour plot between the O VII resonance line and forbidden line normalisations. Lower panel: contour plot between the intercombination line and forbidden line normalisations. The theoretical ratio between the forbidden and intercombination lines is plotted with the dashed line.

Chapter 7

# A study of a Coronal Mass Ejection as seen by XMM-Newton

The SWCX case described in this chapter was first identified as a particularly noteworthy observation during the systematic search for SWCX emission undertaken in Paper I and described in Chapter 4. This SWCX case proved to be the most spectrally rich example of SWCX found within the initial Paper I sample and also the most spectrally rich example within the whole dataset, and its possible association with a known CME warranted a more detailed study. This work was presented in the paper Carter et al. (2010), in collaboration with two co-authors. This SWCX case occurred on the 21$^{st}$ of October 2001, recorded during an XMM-*Newton* observation of target 1Lynx.3A_SE (right ascension 08h 49m 06s and declination +44° 51' 24"). This is a field that contains no bright point or extended source emission. The Galactic column in the direction of this field is low ($2.79 \times 10^{20}$ cm$^{-2}$). Fortuitously there were two additional observations of the same target field taken around 6 days and 15 hours respectively previous to the SWCX event. These two observations had substantially overlapping fields of view; the pointing directions of these observations being offset by 1.4 and 2.9 arcminutes respectively which is small compared to the circular 30 arcmin-

utes field of view of XMM-*Newton*. The analysis of these three observations is described in this chapter, including analysis of data from the EPIC-pn camera. For this particular case it was decided to extend the analysis to the pn for detailed spectral analysis and given that all instrumental exposures were taken using the full-frame mode.

We present the analysis of this SWCX case and reason that the unusual X-ray signatures seen are due to a Coronal Mass Ejection (CME) that was recorded on $19^{th}$ of October 2001 by the Solar and Heliospheric Observatory (SOHO) (Domingo et al., 1995) and which subsequently passed by the Earth. CMEs involve an ejection of high density plasma with characteristics different to that of the ambient solar wind; for example unusually high Fe charge states or enhanced alpha particle to proton ratios (Zurbuchen & Richardson, 2006). CMEs may pass by the Earth, depending on their location of origin in the solar corona and passage through interplanetary space. The absolute frequency of CMEs increases around solar maximum, although at solar minimum, CMEs occur approximately weekly. The event under analysis in this section occurred close to solar maximum in 2001. We use additional data from both ACE and the *Wind* spacecraft to support our argument. We also analyse XMM-*Newton* observations before and after our case observation and the nearest *Chandra* observation in time to this period.

## 7.1 Target pointings

The observations and their start and stop times for the EPIC instruments are detailed in Table 7.1. The identifiers for these observations are 0085150101, 0085150201 and 0085150301. Henceforth they are referred to as Obs101, Obs201 and Obs301 (the SWCX event) respectively. Breaks during a single observation, noted using various exposure identifiers, are due to the instruments being switched to a safe, non-observational mode as a result of the extremely high radiation environment that the satellite encountered during this period. No other XMM-

**Table 7.1:** XMM-*Newton* observations from October 2001, towards Right Ascension and Declination (08h 49m 06s, +44° 51' 24"). We state the orbital revolution number (one orbit takes 48 hours), instrument and exposure identifiers as explained in the text. The start and stop times are given in the XMM-*Newton* time system (number of seconds since the start of 1999). All observations were taken with the medium filter and in full-frame mode.

| Obs id. | Rev | Inst | ExpID | Start ($\times 10^8$ s) | Stop ($\times 10^8$ s) |
|---|---|---|---|---|---|
| 0085150101 | 0339 | MOS1 | S002 | 1.195187 | 1.195674 |
| | | MOS2 | S003 | 1.195185 | 1.195674 |
| | | pn | S001 | 1.195211 | 1.195671 |
| 0085150201 | 0342 | MOS1 | S002 | 1.200241 | 1.200703 |
| | | | U002 | 1.200739 | 1.200743 |
| | | MOS2 | S003 | 1.200241 | 1.200704 |
| | | | U002 | 1.200742 | 1.200743 |
| | | pn | S001 | 1.200265 | 1.200746 |
| 0085150301 | 0342 | MOS1 | S002 | 1.200781 | 1.200800 |
| | | | U002 | 1.200837 | 1.200838 |
| | | | U003 | 1.200865 | 1.201288 |
| | | MOS2 | S003 | 1.200781 | 1.200801 |
| | | | U002 | 1.200837 | 1.200839 |
| | | | U003 | 1.200865 | 1.201288 |
| | | pn | S001 | 1.200805 | 1.201286 |

*Newton* observation was performed between Obs201 and Obs301.

All three observations underwent the lightcurve analysis described in Chapter 4. Obs101 and Obs201 showed no evidence for a variable SWCX component to the observed diffuse emission. This case of Obs301 exhibited the highest value of $\chi^2_\mu$ during the search through the XMM-*Newton* archive, excluding two observations of comets and as presented in Table 4.1. The diagnostic plots that were used to identify this case are shown in Figure 7.1. In this figure we show the steps applied to the lightcurves (as described in Chapter 4). The upper-left panel shows the original line-band and continuum lightcurves. The exposure coverage of each bin is shown in the upper-right panel. The lightcurves adjusted by their respective means are shown bottom-left and the scatter plot with the result of the linear fitting routine (red line) is given bottom-right.

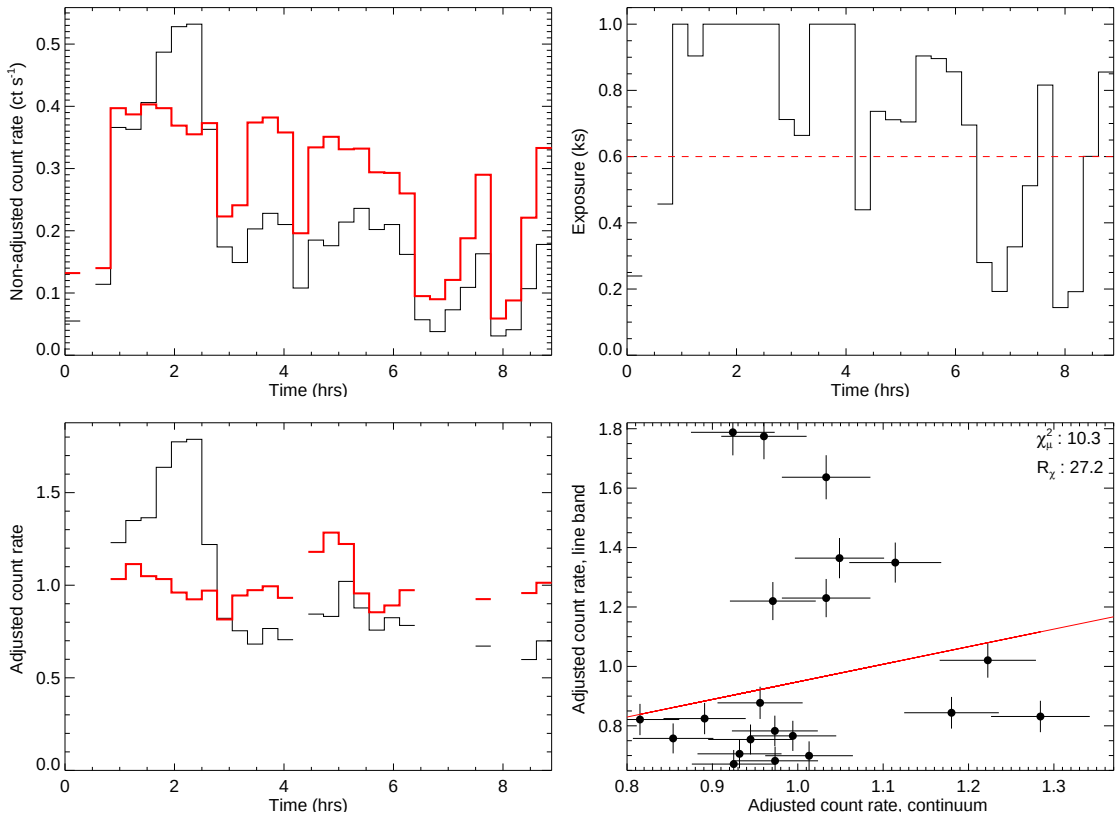


**Figure 7.1:** Diagnostic plots used to identify the archival case with the highest $\chi^2_\mu$ value. For the lightcurve plots, the line-band is plotted in black and the continuum in red. Top left: example lightcurves showing a peak in the line-band that is not reflected in the continuum. Top right: exposure coverage for each bin, the threshold at 60% is marked by the red dashed line. Bottom left: lightcurves after the adjustments for exposure correction and scaling by the mean. Bottom right: scatter plot between the adjusted lightcurves.

In addition, we searched for *Chandra* (Weisskopf et al., 2000) observations within the *Chandra* archive[1] during the period of the Obs301 event, but unfortunately there was no simultaneous coverage. The closest observation, (number *2365*, instrument ACIS-I, target 1RXSJ161411.3-630657), began towards the end of Obs201, but was stopped well before the start of Obs301 due to the high radiation environment also experienced by *Chandra* at the time. The next observation taken by *Chandra* did not occur until the $23^{rd}$ October, after Obs301 had been completed. The XMM-*Newton* observation immediately after Obs301 was very heavily radiation contaminated and extremely short so was excluded from further analysis. This was followed by several observations in a closed calibration mode (CALCLOSED). The observation after these CALCLOSED observations (observation 0083000101, target B3 0731+438) was also in full-frame mode for each of the EPIC instruments.

In Figure 7.2 we plot an illustration of the X-ray activity as seen by these observations. We have plotted the ratio of the diffuse "oxygen" line-band (0.5 to 0.7 keV) count rate to continuum band (2.5 to 5.0 keV) count rate, normalised by the mean of this ratio for each observation. All XMM-*Newton* data have been filtered as described in Chapter 4. For the *Chandra* observation we downloaded the ACIS *Level 2* event file and extracted the counts from a large region (radius 0.06 degrees) centred on chip 3. By inspection the *Chandra* target is an extended and presumably non-variable source. The XMM-*Newton* Obs301 observation is the only observation around this period with evidence for a variable diffuse signal in the low energy line-band that is not correlated with variations in the higher energy band (continuum).

Using the same time axis we also show the solar proton flux, as recorded by ACE at the sunward L1 Lagrangian point, approximately 200 earth radii ($R_E$) from the Earth. The data are Level 2 64 second-averaged products from the SWEPAM instrument from the ACE archive[2]. One can see a dramatic rise in the solar proton level between Obs201 and Obs301. It has

[1] http://cxc.harvard.edu/cda/
[2] http://www.srl.caltech.edu/ACE/ASC/

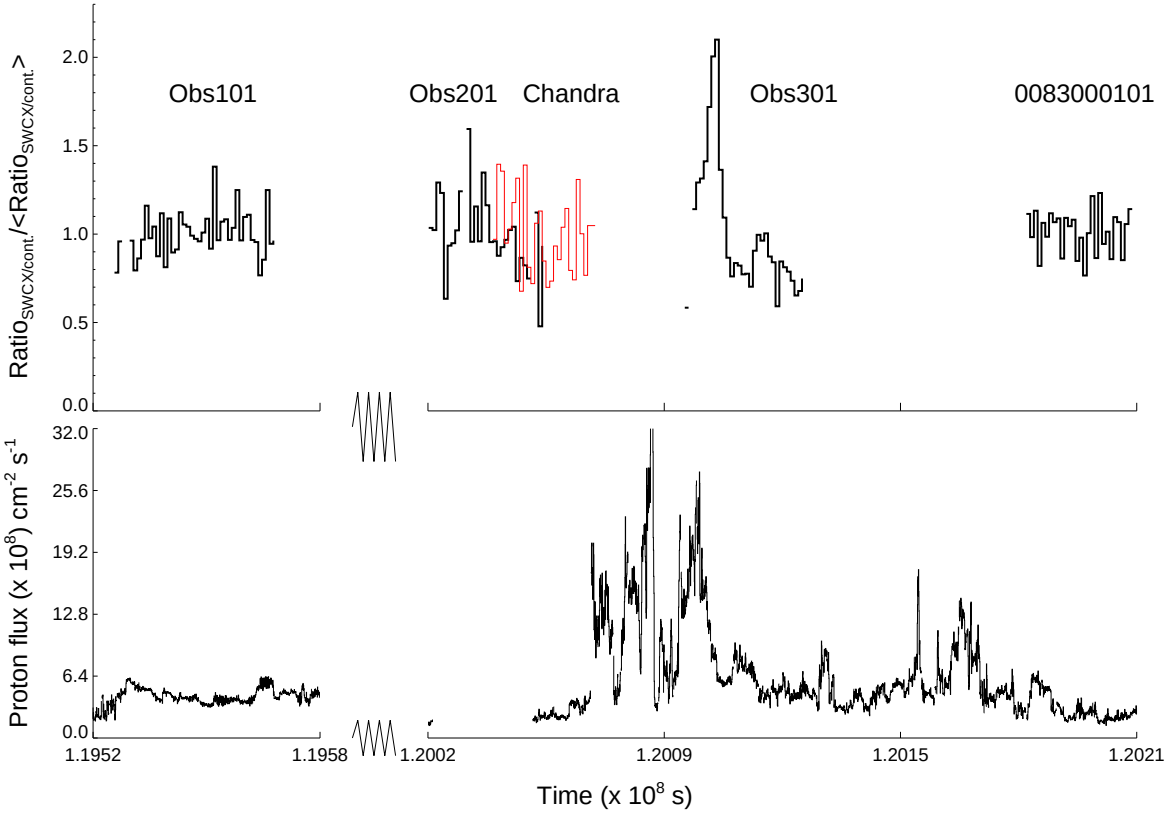


**Figure 7.2:** Upper panel: The ratio of the (0.5 to 0.7 keV, oxygen emission) line-band and (2.5 to 5.0 keV) continuum lightcurves, scaled to the mean of this ratio for each observation, for observations Obs101, Obs201, and Obs301 along with the next XMM-*Newton* imaging mode observation that was sufficiently long (>4 ks) to be processed (observation id. 0083000101). The same ratio scaling is used for the *Chandra* data, shown in red. Lower panel: The solar wind proton flux, taken from the ACE SWEPAM instrument.

been shown by Wang et al. (2005) (and later discussed in Section 7.6) that the rise in activity recorded by ACE at this epoch was due to the $19^{th}$ October 2001 CME. A rise in the XMM-*Newton* ratio is seen shortly afterwards.

In the following analysis we concentrate our X-ray analysis on the two XMM-*Newton* observations, Obs101 and Obs301. Obs101 (the longer of the two previous observations) is useful because it allows us to unambiguously determine the non-variable diffuse X-ray background in the direction of Obs301.

## 7.2 Extraction of spectral products

XMM-*Newton* SAS software (version 8.0.0) was used to process the raw data into calibrated event lists and extract lightcurves, spectral products and instrument response files. The instrument effective area files were calculated assuming the source flux is extended with no intrinsic spatial structure. For this analysis we used the latest public CCFs released as of July 2009.

When creating products from the calibrated event files we applied the following filter expressions in the nomenclature of the SAS; (PATTERN<=12)&&(#XMMEA_EM) for the MOS and (PATTERN==0)&&(FLAG==0) for the pn. The specified PATTERN filter selects events within the whole X-ray pattern library for the MOS and mono-pixels only for the pn; as our focus is on detecting line emission below 2 keV, this restriction optimises the energy resolution of the pn with little loss of sensitivity in the energy range of interest. For these event class selections, the energy resolution of the pn is $\sim 70$ eV (FWHM) at 1 keV compared with $\sim 60$ eV in the MOS. The filter #XMMEA_EM removes events from the MOS that are from regions of known bright pixels or columns or near CCD boundaries (which tend to be noisy). The equivalent flag for the pn, #XMMEA_EP, did not remove some residual noisy pixels, but

these were removed when we used the more conservative FLAG==0. This flag also masks out events from regions adjacent to noisy pixels.

In addition we selected only events within a radius of 11.7 arcminutes, centred on a common sky position such that the extraction region of all three cameras was covered by active silicon, barring inter-CCD gaps.

## 7.3 Spectral modelling

A spectral analysis of the SWCX emission component in Obs301 requires us to identify and account for each of the sources of X-rays that contribute to the combined signal across the field of view. A detailed description of the various major components which constitute the XMM-*Newton* EPIC background was given in Chapter 2. In the following sections we describe how each of these components, plus the contribution from resolved point sources, is either subtracted from our data, or modelled within our spectral fitting. Both Obs101 and Obs301 are considered in this section. We used Version 12.5.0 of the XSPEC X-ray spectral fitting package to perform this analysis.

### 7.3.1 Residual resolved sources

Using the source count rates within the source lists, we estimate that the total residual resolved source count rate (0.2 to 2.0 keV) in the pn after cleaning would be around 0.04 ct $s^{-1}$ in Obs101. The background-subtracted count rate in the same energy band after source removal was 0.75 ct $s^{-1}$, hence, residual sources contribute approximately 5% of the observed diffuse flux in this observation. In Obs301 the diffuse flux count rate is 1.8 ct $s^{-1}$ and the residual contribution from resolved point sources is at around 2%. Figure 7.3 shows the

cleaned images from each camera from Obs301, with the positions of the point sources and spectral extraction region marked, in the energy range 0.3 to 2.0 keV. There are 62 sources which overlap the source extraction region.

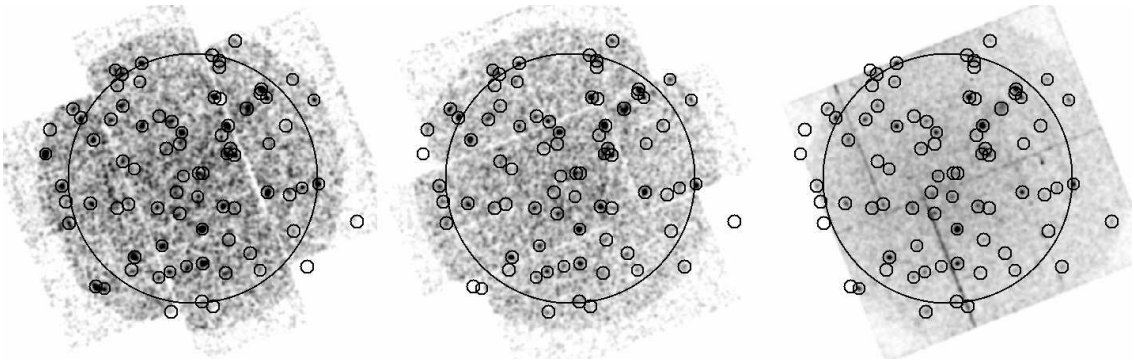

**Figure 7.3:** Images from each of the EPIC cameras for Obs301 (left to right); MOS1, MOS2 and pn, in the energy range 0.3 to 2.0 keV. The small black circles indicate the point sources removed from analysis, and the large black circle indicates the spatial extraction region used for spectral analysis.

### 7.3.2 Soft protons

As described in Section 2.1.1, solar protons may be accelerated by reconnection events in the vicinity of the Earth (Lumb et al., 2002). They are funnelled by the telescope mirrors onto the detectors where they are absorbed; the signals produced by individual events are indistinguishable from X-rays. Figure 7.4 shows the Obs301 2.5 to 8.5 keV lightcurves of the three EPIC cameras (after point-source removal) binned in 100 s intervals. The dataset is extremely contaminated by soft proton flares and shows data gaps in the MOS when the instrument was switched to a safe mode. The pn instrument takes longer to set up for a given observation therefore the pn lightcurve starts about 40 minutes after the MOS.

Data cleaning schemes for flares include excluding bins whose count rate in a high energy band exceeds a set threshold or excluding bins which are more than a set value of sigma from the mean value of the lightcurve. The latter method is that employed by the publicly available ESAS package, as described in Snowden et al. (2008) and used in Chapter 4. At

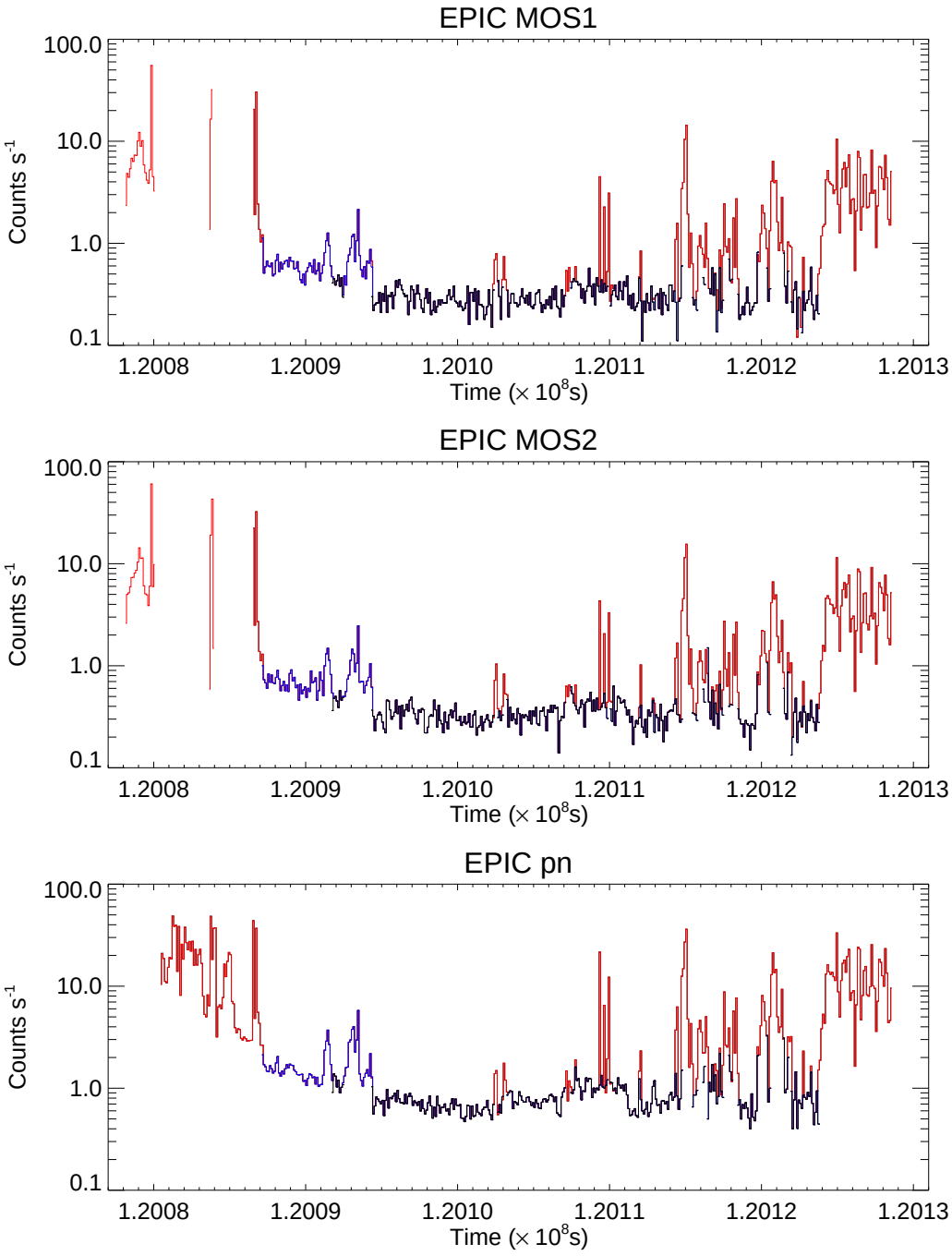


**Figure 7.4:** The 2.5 to 8.5 keV EPIC lightcurves of the diffuse signal from Obs301, incorporating all exposures. The variance in the signal is due to soft proton contamination. Bins marked in red indicate where data have been excluded from further analysis. Bins marked in black are the cleanest data used for spectral fitting of the integrated spectra. Bins in blue are used in addition for analysis of the lightcurve.

the time of processing the data the ESAS package was only directly applicable to the MOS data, however, we used the package to derive Good Time Interval (GTI) files for MOS1 and MOS2 and then merged them into a single file which proved to be sufficiently accurate in identifying periods of proton flaring in the pn data.

The data bins accepted by the single GTI file are shown in Figure 7.4 in black. We have used this data selection for the integrated spectra as described in Section 7.3.6. We also included the data for the period marked in blue in our analysis of the SWCX lightcurve because we wished to try and establish the start of the period of SWCX enhancement.

Soft protons can have a low temporal variance which is often difficult to detect via an analysis of the lightcurve, although in this case it can be seen that there appears to be a slowly varying signal in the residual GTI periods. This was confirmed as being due to soft protons via our spectral analysis.

These soft-proton events produce a featureless *power law* spectrum unmodified by the detector response. There is generally a correlation between spectral hardness and intensity and the spectral slope can show a break with a steepening at higher energies. The component can be modelled within a typical XSPEC analysis session by folding a power law (or broken power law) through a diagonal response matrix (i.e. one constructed to have a response value of 1.0 on the diagonal elements and zero elsewhere). XSPEC Version 12 has the functionality to enable several model spectra to be convolved with distinct responses and then added together into a combined model which can be compared with the data. This combined model refers to the model of the diffuse X-ray emission, which incorporates various background components convolved with the instrument response and the soft proton model convolved with the diagonal response.

### 7.3.3 Cosmic-ray particle background (CPB)

High energy cosmic rays produce background either directly within the CCDs or via fluorescence within the spacecraft material surrounding the detectors (see Section 2.1.2). The CPB contribution to a given observation can best be estimated by deriving the spectrum from EPIC data taken when the instruments are in the FWC configuration (i.e the filter wheel is closed and not open to the sky). In this configuration the observed signal consists of the CPB plus detector noise (see Section 7.3.4). The XMM-*Newton* BGWG maintain co-added event files of FWC data (total exposures of around 700 ksec in each MOS and 300 ksec in the pn) on their public web site (as described in Chapter 2).

The intensity of the fluorescence lines resulting from the CPB varies across the field of view of each instrument, therefore, it is necessary to extract the spectra from the identical regions to those that define the source spectrum. The spectra extracted from the FWC data sets constituted the background files in our XSPEC fits.

It is not unusual for the derived CPB spectrum to require some small amount of re-scaling for a given observation. This can be done by comparing the observed high energy count rate in the source and CPB spectra above an energy where the contribution from components other than the CPB in the source spectrum is expected to be negligible. Naturally, the source dataset must be clean of soft proton contamination before a simple scaling of the CPB can be made. As this was the case in Obs101 and as our model of the diffuse X-ray sky predicted a relatively negligible contribution to the observed count rate in the energy range 7.75 to 12.0 keV, we used this band in all three EPIC instruments to derive scaling factors for the CPB of 1.26, 1.11 and 1.08 respectively in the pn, MOS1 and MOS2 (i.e. the observed FWC CPB count rate was greater by these factors than observed in our source observation). Such factors are not uncommon (De Luca & Molendi, 2004).

Because our SWCX dominated observation, Obs301, was contaminated by residual soft protons throughout the observation and therefore had a strong contribution from this component at high energies, we were unable to apply the same procedure as for Obs101 to subtract the CPB. We assumed therefore that the scaling factors for the CPB derived from Obs101 would be appropriate for this observation; a reasonable assumption given that the observations are only 6 days apart.

### 7.3.4 Detector noise

Detector noise is one low-energy component of the signal within FWC datasets (see Section 7.3.3 and Chapter 2) and it is fairly straightforward to subtract from the total signal. This component is approximately of constant count rate throughout a given observation. Certain defective areas are recognised by the SAS and events from these regions are flagged (see Section 7.2), enabling them to be excluded or included depending on the requirements of the analysis.

There are other components, however, that are not so amenable to subtraction via event flagging. CCD5 of the MOS1 detector showed an elevated background across the whole chip characterised by a continuum of spurious events with energies up to $\sim 1$ keV. This CCD was in the anomalous state, as described in Section 2.1.3. Our solution was simply to remove this CCD from our analysis. This type of noise signal is variable from observation to observation and other CCDs can also show a similar behaviour with around $\sim 20\%$ of observations affected at some level (Kuntz & Snowden (2008) and described in Chapter 2). The physical cause of the noise is unknown at present.

### 7.3.5 Sky background model

Obs101 allowed us to independently derive the contribution from the diffuse Galactic and extragalactic emission components in the direction of Obs301. The target area has a galactic longitude and latitude of (176°, 40°) so is well away from the plane of the Galaxy and Galactic centre. Having removed the resolved point sources and flare cleaned the data (as described in Chapter 4), Obs101 appeared by inspection to contain no evidence for significant residual soft protons or a time varying SWCX component. We therefore assumed that the resultant diffuse emission comes from non-varying sources and that the spectrum and intensity of this component could be fixed and applied to observation Obs301.

Following previous authors (e.g. Galeazzi et al. 2007) we have modelled the Obs101 diffuse photon emission with a three-component description. The first component is a constant un-absorbed plasma representing emission from the Local Hot Bubble and a possible contribution from SWCX emission at the boundary of the heliosphere (Robertson & Cravens, 2003a; Koutroumpa et al., 2007). Any contribution from the heliospheric SWCX we assume to be essentially constant over the 6 days between the observations. The second component is an absorbed plasma representing emission from the Galactic halo. We used the APEC (Smith et al., 2001) model within XSPEC to model the plasma components although the commonly used alternative Raymond-Smith and Mekal models gave a statistically similar result in the former and marginally worse in the latter, see Table 7.2. The third component, also absorbed by the same line-of-sight material, is a power law representing the unresolved extragalactic X-ray background from point sources. For the absorption, we have used the *phabs* model within XSPEC. The element abundances in the absorption and emission models used were those set by the *wilm* table (Wilms et al., 2000) and the cross-sections based on Balucinska-Church & McCammon (1992) and Yan et al. (1998). The value of $N_H$ was fixed at the Galactic line-of-sight value of $2.79 \times 10^{20}$ cm$^{-2}$ and derived using the nH tool available

**Table 7.2:** Plasma emission models tried as components to the model applied to Obs101, with the associated reduced-$\chi^2$ values of the fit.

| Model | Reduced $\chi^2$ / Degrees of Freedom |
|---|---|
| APEC | 1.11 / 1775 |
| Mekal | 1.49 / 1769 |
| Raymond-Smith | 1.16 / 1772 |

from the HEASARC web site [3].

We first independently fit the model to each of the CPB background-subtracted Obs101 spectra from the pn, MOS1 and MOS2. However, after several analysis iterations we found that we could achieve an acceptable fit to the data by jointly fitting the model to all three EPIC instruments allowing only the global normalisation of the entire model to vary between the cameras. Table 7.3 lists the derived model parameters and component fluxes. The fluxes from each camera are consistent with each other at the 90% confidence level, although the MOS returns values $\sim 20\%$ lower than the pn.

Figure 7.5 shows the data compared to the best-fit model in each of the three cameras. When fitting the data we excluded the energy range 1.35 to 1.9 keV because, as can been seen in the figure, the strong instrumental Al $K_\alpha$ and Si $K_\alpha$ lines can produce large residuals at these energies after background subtraction. There is also a broad residual in the pn fit at 0.45 keV whose strength is not sensitive to the particulars of which abundance table or plasma model within XSPEC is selected. MOS1 has a similar, although narrower feature, whereas MOS2 does not. The strength of the feature is not sufficient to have a significant bearing on our analysis of the SWCX signal within Obs301.

[3] http://heasarc.gsfc.nasa.gov

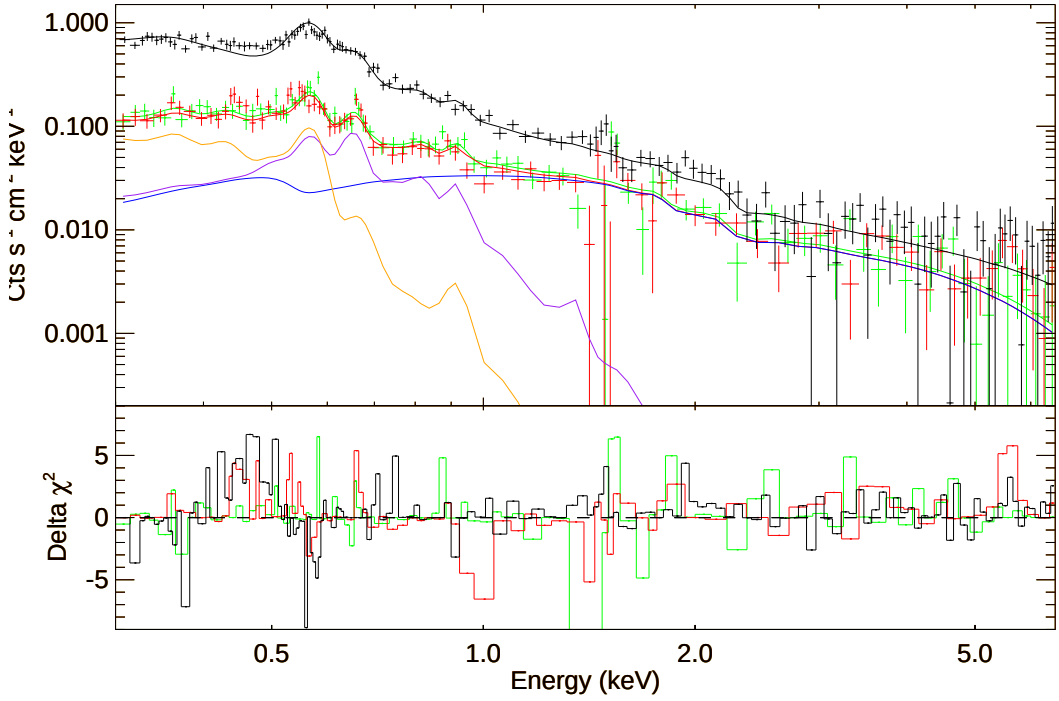


**Figure 7.5:** Background-subtracted pn (black), MOS1 (red) and MOS2 (green) spectra from Obs101 compared with a model of the diffuse sky emission. Also shown are the three components of the model, the un-absorbed plasma (orange), the absorbed plasma (purple) and absorbed power law continuum (blue). For clarity, only the individual model components for MOS1 are shown. The lower panel shows the deviation of the data from the model.

**Table 7.3:** Sky model parameters in the direction of Obs301 derived from an analysis of Obs101. Quoted errors are 90% confidence for one interesting parameter. Fluxes are observed values in the energy range 0.2 to 10 keV in units of $10^{-8}$ ergs cm$^{-2}$ s$^{-1}$ sr$^{-1}$.

| Diffuse Sky Background Model | | |
|---|---|---|
| Reduced $\chi^2$ / Degrees of Freedom | | 0.99 / 1008 |
| Component | Parameter/Flux | Value (Error) |
| Unabs. Plasma | Temperature (keV) | 0.11 (0.01) |
| | MOS1 Flux | 2.04 (0.18) |
| | MOS2 Flux | 1.99 (0.18) |
| | pn Flux | 2.42 (0.20) |
| Abs. Plasma | Temperature (keV) | 0.23 (0.02) |
| | MOS1 Flux | 1.23 (0.18) |
| | MOS2 Flux | 1.12 (0.18) |
| | pn Flux | 1.46 (0.21) |
| Abs. CXRB | Photon Index | 1.44 (0.12) |
| | MOS1 Flux | 5.31 (0.56) |
| | MOS2 Flux | 5.18 (0.55) |
| | pn Flux | 6.29 (0.63) |

### 7.3.6 SWCX model

The lightcurve of Obs301 in Figure 7.2 suggests the soft band flux has a *flare* and a *quiescent* period. Background-subtracted spectra integrated over these intervals (extracted from the soft proton flare-cleaned data) are shown in Figure 7.6. In addition we show the diffuse sky model folded through the instrument response and the strong residual soft proton component. The soft protons are modelled with a single power law spectrum fit by initially restricting the spectral fit to the range 2.5 to 6.5 keV. The extrapolation of the power law shows that the soft proton component is comparable to or weaker than the non-variable diffuse sky component below $\sim 1$ keV, and may be weaker still because, as previously discussed, soft protons often display a spectral break. For this reason, the strength of the residual SWCX component at low energies may be underestimated by a few percent.

It is evident from Figure 7.6 that *both* the flare and quiescent periods show an excess flux

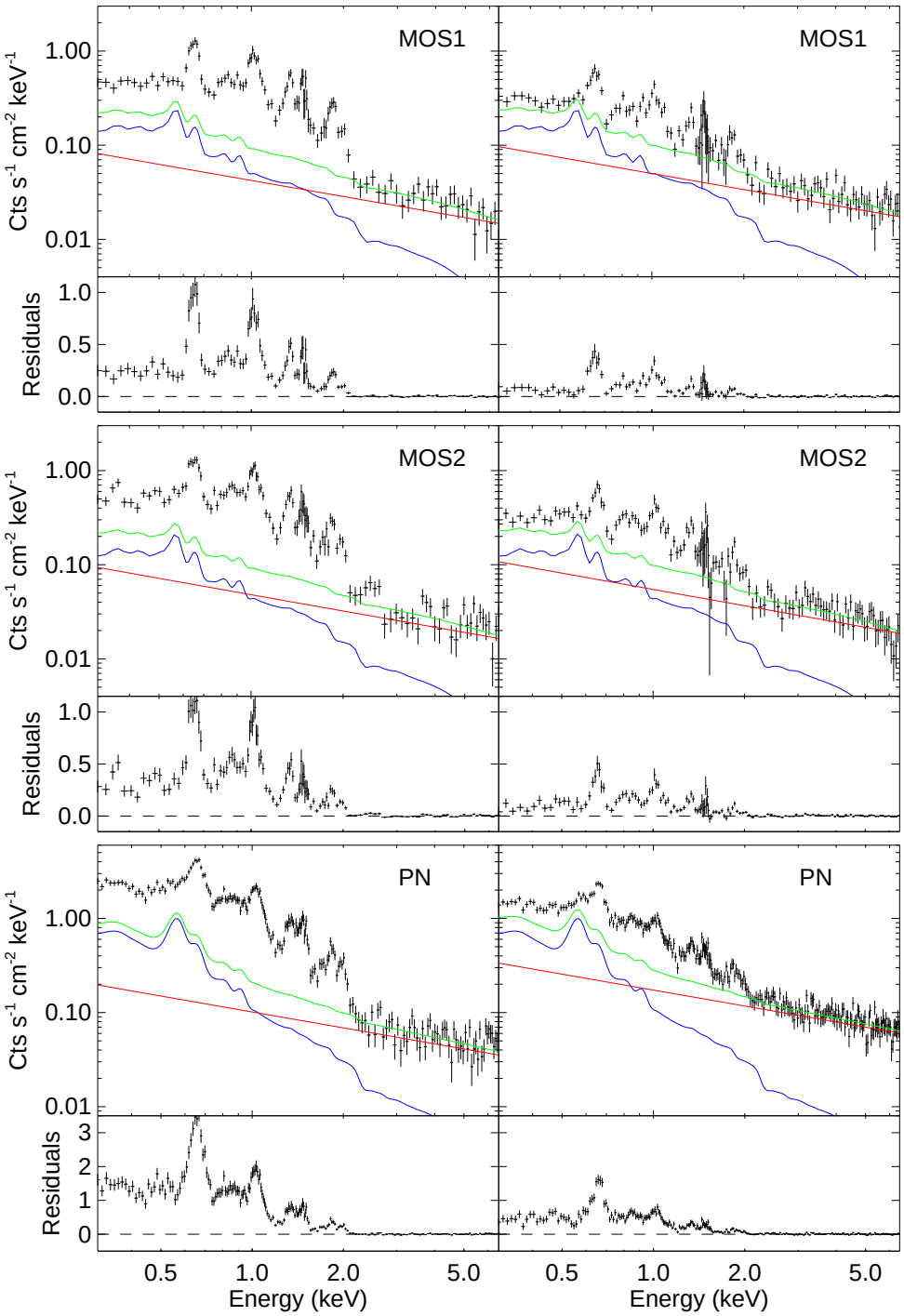


**Figure 7.6:** Obs301 background-subtracted spectra integrated from T = $1.200918 \times 10^8$ s to $1.201035 \times 10^8$ s (left panels) and from T = $1.201035 \times 10^8$ s to $1.201230 \times 10^8$ s (right panels). Contributions are shown from soft protons (red), the non-variable diffuse sky background (blue), and these components combined (green). The variable excess flux, seen in the lower residuals panels, is due to SWCX.

above the combined diffuse sky flux and soft proton contribution which is spectrally distinct from these components. The excess clearly contains emission lines and is variable which are both signatures of SWCX. The most prominent lines are at 0.65 keV and 1.02 keV which we identify with O VIII and Ne X. Laboratory measurements and theoretical calculations of SWCX emission (e.g. Wargelin et al. 2008) indicate that emission spectra will contain multiple lines from a variety of ions and their transitions, most of which will be unresolved in the EPIC instruments, given the limits of the energy resolution of the detectors.

Our spectral model of the SWCX excess was built up from a series of zero-width Gaussian lines with energies fixed at known X-ray emission transitions from likely solar wind ions. For C V, C VI, N VI, N VII, O VII and O VIII we have used the theoretical model as presented in Bodewits et al. (2007) (Table 2), who has calculated the relative emission cross-sections of these bare and H-like ions (their state before electron capture) in collision with atomic hydrogen for a variety of solar wind velocities. We have used the tabulated values for a velocity of 600 $\mathrm{km\,s^{-1}}$ which is close to the velocity measured by ACE at this epoch. Our model fitting allowed the six normalisations of the principal transition from each of these ions to be free, but constrained the normalisations of the weaker transitions to the ratios predicted by the Bodewits' model. In all, these ions contributed 33 lines between 0.299 and 0.849 keV.

At higher energies we have taken a more empirical approach by adding sufficient lines at known transition energies to characterise the bulk of the residual excess emission. This will be an incomplete list due to the multiple transitions expected from Fe for example. Table 7.4 lists the principal transitions we have included in the SWCX model.

We have fit our combined model (containing the SWCX, sky background and soft proton components) jointly to the integrated spectra from each of the EPIC cameras. The free parameters in the fit are the normalisations of the principal ions in the SWCX model plus global normalisations applied to the individual MOS spectra (the pn global normalisation was fixed

at 1.0).

In Table 7.4 we list the flux of the O VIII line at 0.65 keV and the ratio of the fluxes for each of the other ions to O VIII, and the total flux of the SWCX model. Individual line fluxes were calculated by finding the best fit global model, then setting all other line normalisations to zero. As with our analysis of the diffuse sky background in Obs101, the broad-band MOS fluxes are lower than that measured by the pn by a similar factor. In a study of the inter-calibration of point sources from the 2XMM catalogue, Mateos et al. (2009) found the reverse trend; on average the MOS cameras register a higher flux than the pn by 7-9% below 4.5 keV. We can only attribute the difference to some unknown calibration uncertainty in the calculation of the effective area for point sources compared with an extended region.

## 7.4 Spectral variability

Figure 7.7 shows the best fit SWCX spectral model (plus the non-variable diffuse sky and variable soft proton components combined) to the background-subtracted and flare-cleaned pn spectrum. The non-Gaussian shape of the pn detector response (the MOS is similar; the Gaussian shape is distorted by a low-energy shoulder) is evident from the principal O VIII line. The residual at $\sim 1.4$ keV may be due to incomplete background subtraction at the energy of the strong Al $K_\alpha$ instrumental line.

The temporal variation in the SWCX emission has been mapped by extracting spectra in eight 2 ks intervals followed by five 4 ks intervals. This covers the soft proton flare-cleaned period plus the additional proceeding segment as shown in Figure 7.4 (marked in blue). For each interval, we show in Figure 7.8 the fitted fluxes of the O VIII (0.653 keV) line and the ratio of the fluxes of O VII (0.561 keV), Ne X (1.022 keV), Mg XI (1.329 keV) and Si XIV (2.000 keV) to O VIII. There is little evidence for a significant compositional change throughout the

**Table 7.4:** Measured fluxes in the SWCX spectral model. We list only the principal transitions (C, N and O) plus the additional selected transitions (Ne, Mg, Si and Fe). The emission line at 1.10 keV maybe due to Ne IX or highly-charged iron. The value for O VIII is the measured flux, quoted in units of $10^{-8}$ ergs cm$^{-2}$ s$^{-1}$ sr$^{-1}$. Other values are the ratio of the measured flux for that ion to O VIII and the total SWCX flux.

| Ion | Principal Energy (keV) | Ion Ratio / O VIII Flux |
|---|---|---|
| C V | 0.299 | 0.50(0.16) |
| C VI | 0.367 | 0.28(0.08) |
| N VI | 0.420 | 0.06(0.05) |
| N VII | 0.500 | 0.19(0.03) |
| O VII | 0.561 | 0.12(0.03) |
| O VIII | 0.653 | 2.70(0.09) |
| Fe XVII | 0.73 | 0.13(0.01) |
| Fe XVII | 0.82 | 0.05(0.02) |
| Fe XVIII | 0.87 | 0.10(0.03) |
| Fe XIX/Ne IX | 0.92 | 0.14(0.03) |
| Fe XX | 0.96 | 0.09(0.02) |
| Ne X | 1.022 | 0.46(0.02) |
| Fe??/Ne IX | 1.10 | 0.20(0.01) |
| Fe XX/Ne X | 1.22 | 0.08(0.01) |
| Mg XI | 1.33 | 0.28(0.01) |
| Mg XII | 1.47 | 0.29(0.02) |
| Mg XI | 1.60 | 0.06(0.01) |
| Al XIII | 1.73 | 0.08(0.01) |
| Si XIII | 1.85 | 0.30(0.02) |
| Si XIV | 2.00 | 0.15(0.02) |
| Total SWCX (pn normalisation = 1.0) | | 12.58 (0.20) |
| MOS1 Normalisation | | 0.80 (0.02) |
| MOS2 Normalisation | | 0.92 (0.02) |
| Reduced $\chi^2$ / Degrees of Freedom | | 1.17 / 1546 |

observation with the possible exception of the second and third bins where the flux ratios of the heavier ions are somewhat higher compared to the average.

Ion compositional data (level 2, hourly averaged) from the SWICS/SWIMS instrument on board ACE are sparse for the period of interest. XMM-*Newton* therefore is able in this case to provide supplementary abundance information where ACE, for data quality reasons, cannot.

## 7.5 Basic emissivity modelling

The expected X-ray emissivity of SWCX emission from the solar wind interaction with the magnetosheath can be estimated from the integrated emission along the line of sight for the observer. The expected emissivity ($P_\chi$) can be expressed as in Equation 7.1 (from Cravens 2000).

$$P_\chi = \alpha \eta_{sw} \eta_n \langle g \rangle \ \left[ eV cm^{-3} s^{-1} \right] \tag{7.1}$$

Where $\alpha$ is a scale factor dependent on various aspects of the charge exchange such as the interaction cross-section and the abundances of the solar wind ions, $\eta_{sw}$ is the density of the solar wind protons, $\eta_n$ is the density of the neutral species and $\langle g \rangle$ is their relative velocity.

The flux (F) is given by integrating along a particular line of sight, shown in Equation 7.2.

$$F = \frac{1}{4\pi} \int_0^\infty P_\chi ds \ \left[ eV \ cm^{-2} s^{-1} sr^{-1} \right] \tag{7.2}$$

To assist in our analysis for this section, we took data from the Solar Wind Experiment (SWE) instrument (Ogilvie et al., 1995) on board the spacecraft *Wind* and data as measured by the

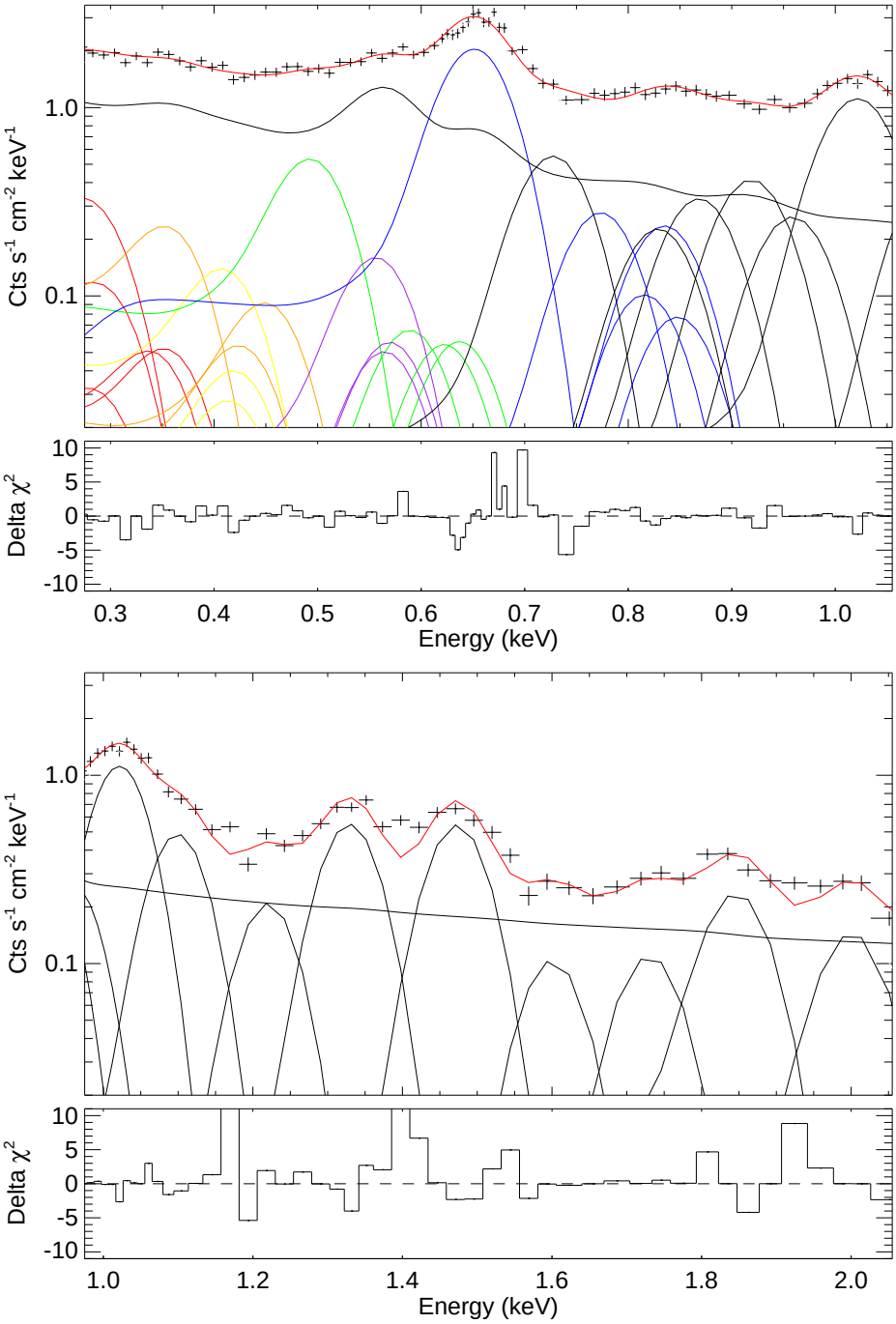


**Figure 7.7:** The SWCX spectral model fitted to the integrated background-subtracted and flare-cleaned pn spectrum of Obs301. Top panel: the spectrum from 0.275 to 1.055 keV. Bottom panel: the spectrum from 0.975 to 2.055 keV. The sum of the non-variable sky and variable soft proton components is the continuous line in black. Individual lines are colour coded; C V (red), C VI (orange), N VI (yellow), N VII (green), O VII (purple) and O VIII (blue). Heavier elements are shown in black.

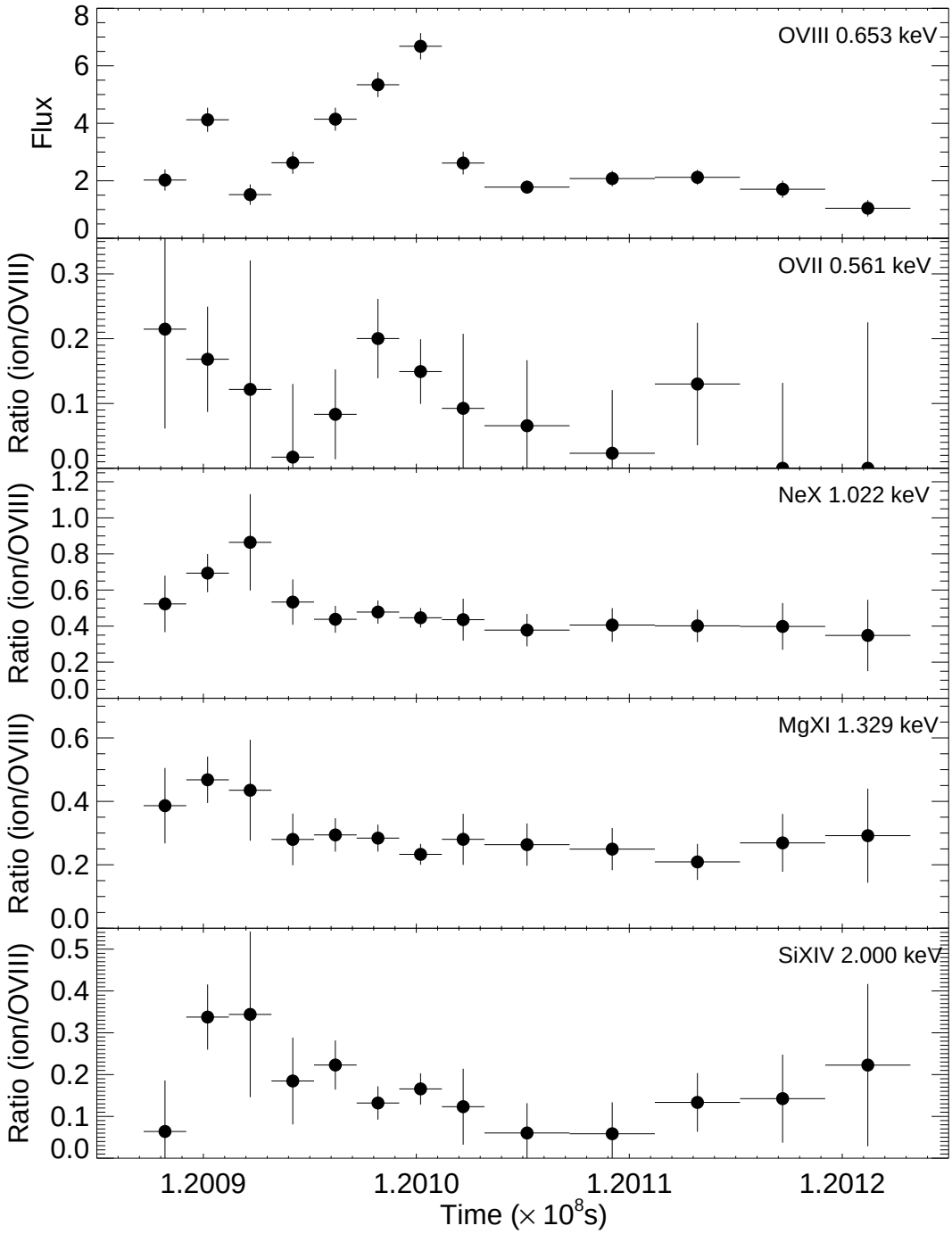


**Figure 7.8:** Lightcurves of selected ions from Obs301. The top panel is the O VIII flux in units of $10^{-8}\,\mathrm{ergs\,cm^{-2}\,s^{-1}\,sr^{-1}}$. Lower panels are the ratio of the flux of the selected ion to O VIII.

SWEPAM instrument of ACE.

In Figure 7.9, we plot the trace of XMM-*Newton*'s path, the magnetopause and bowshock boundaries and the line-of-sight at three points during Obs301. The line of sight pointed through the flanks of the magnetosheath throughout the observation. XMM-*Newton* crossed the bow shock boundary as it moved along its orbit, and as the boundary position changes in response to conditions in the solar wind. The magnetopause and bow shock locations may vary dramatically, especially under extreme solar wind conditions as we see in this case. We used the model of Shue et al. (1998), which takes the strength of one component of the magnetic field ($B_z$) and the proton dynamic pressure as input, to calculate the location of the magnetopause. The position of the bowshock standoff distance (the distance from the Earth to the bowshock on the Earth-Sun line) is calculated using the solar wind dynamic pressure (Khan & Cowley, 1999), and its shape is approximated using a simple parabola (eccentricity 0.81). We plot the positions of XMM-*Newton* as it moves from $T = 1.200805 \times 10^8$ s to $T = 1.2009 \times 10^8$ s (first panel), through $T = 1.2010 \times 10^8$ s (second panel) until $T = 1.2012 \times 10^8$ s (third panel). The magnetopause and bowshock positions are plotted for the end of each period. XMM-*Newton* remains outside the magnetopause for the entirety of the observation, but is not always found outside the bowshock. Therefore the line-of-sight through the magnetosheath region is short, but not zero, at various times during Obs301.

During Obs301 the average solar proton density (level 2, hourly averaged data from ACE), was measured as $13\,\mathrm{cm}^{-3}$ and had an average speed of $647\,\mathrm{km\,s}^{-1}$. Exospheric neutral hydrogen densities fall off as $\mathrm{R_E}^{-3}$ and are normalised to a value of $25\,\mathrm{cm}^{-3}$ at a distance of $10\,\mathrm{R_E}$ (Hodges, 1994; Cravens et al., 2001). Using Equation 7.2 and the solar wind parameters above, we wished to estimate the expected X-ray emission seen by XMM-*Newton* at its average distance from Earth of $13.8\,\mathrm{R_E}$, integrating out to $100\,\mathrm{R_E}$. By this method we compare the scale of the emission as recorded by XMM-*Newton* to a non-time resolved order of magnitude estimation for the expected X-ray emission.

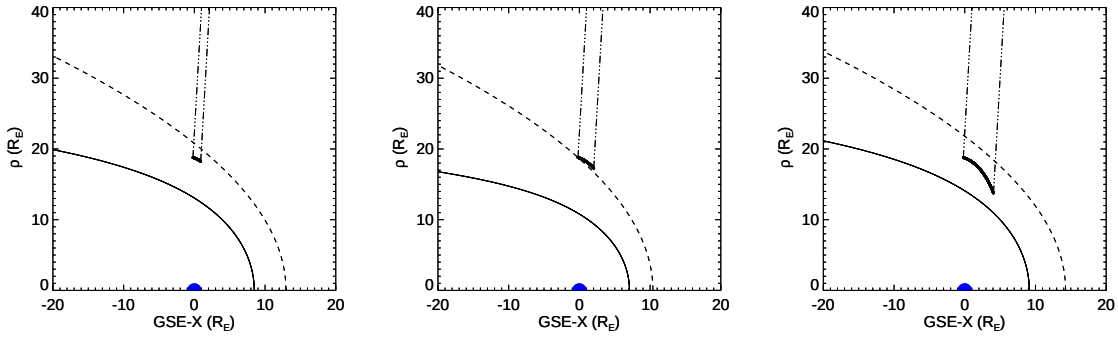


**Figure 7.9:** Position of XMM-*Newton* at three different points during Obs301, at the beginning, middle and end points of the observations for the first to third panels respectively. The position is plotted in GSE-coordinates as $\rho$ (defined as $\sqrt{\text{GSE-Y}^2 + \text{GSE-Z}^2}$) against GSE-X. The line-of-sights towards the target field are shown with the dot-dash line. The solid and dashed lines give the locations of the magnetopause and bowshock at the end of each period.

The solar wind slows down and its density increases inside the magnetosheath (as described in Chapter 3). In this estimation, we base the starting point at the *average* distance of XMM-*Newton* from Earth, so that the line-of-sight through the magnetosheath region is short compared to the remaining line-of-sight out to a maximum of 100 $R_E$. We approximate a line-of-sight of 2.2 $R_E$ from the average position of XMM-*Newton* to the bow shock boundary, with the remainder of the line-of-sight intersecting unperturbed solar wind. To approximate these changes, we scaled hydrodynamical models of Spreiter et al. (1966) (Kuntz, private communication) to the magnetopause standoff distance of 8 $R_E$ and extract factors for adjusting the solar wind parameters at the relevant position within the magnetosheath. We increase the solar wind density by a factor of 3.5 and reduce the solar wind speed by a factor of 0.8 within the magnetosheath region only, and leave it undisturbed outside the bow shock.

The value of $\alpha$ is dependent on the abundances of the ion species contributing to the charge exchange process, along with the cross-section and energy of each interaction in the energy band of interest. For this estimation we consider only contributions from the O VII and O VIII. SWCX emission is directly proportional to $\alpha$, which is in turn proportional to the abundance of the ion species in question. We use the ratio of O VII to O VIII flux from our previous

spectral analysis, the cross-sections found in Bodewits et al. (2007) (assuming a solar wind with velocity $600\,\mathrm{km\,s^{-1}}$) and an oxygen to hydrogen ratio of 1/1780 as given in Schwadron & Cravens (2000) to derive an O VII to O VIII abundance ratio of 0.085:0.915. We then calculate $\alpha$ for these two ion species to be $2.3\times10^{-15}\,\mathrm{eV\,cm^2}$. Although the solar wind speeds during Obs301 are more common of a fast solar wind state, CMEs are enriched with high oxygen charge states and other minor ions (Richardson & Cane, 2004). Equation 7.3 shows how the values of $\alpha$ for a particular transition (oxygen or otherwise) are calculated:

$$\alpha_{\mathrm{X^{q+}}} = \sigma E \left[\frac{\mathrm{X^{q+}}}{\mathrm{O}}\right]\left[\frac{\mathrm{O}}{\mathrm{H}}\right] \quad \left[\mathrm{eV\,cm^2}\right] \tag{7.3}$$

where $\sigma$ is the transition cross-section, $E$ the energy of the emission for this transition and X the ion of charge state $\mathrm{q^+}$. The total $\alpha$ is given by the sum of all $\alpha_{\mathrm{X^{q+}}}$ values contributing to the emission.

The total expected (oxygen band) X-ray emission along the line of sight and for average solar wind conditions was estimated to be $9.5\,\mathrm{keV}\,(1.5\times10^{-8}\,\mathrm{ergs})\,\mathrm{cm^{-2}\,s^{-1}\,sr^{-1}}$. The contribution from inside the magnetosheath is estimated to be $4.8\,\mathrm{keV}\,(7.6\times10^{-9}\,\mathrm{ergs})\,\mathrm{cm^{-2}\,s^{-1}\,sr^{-1}}$ which represents approximately 50% of the total. From our spectral analysis, we observe a flux of $\sim 18.9\,\mathrm{keV}\,(\sim 3.02\times10^{-8}\,\mathrm{ergs})\,\mathrm{cm^{-2}\,s^{-1}\,sr^{-1}}$ from the O VII and O VIII emission lines, approximately 2 times greater than we estimate, but which is consistent given the various assumptions as detailed above. For example, the density of the plasma outside the bow shock may be even higher than the values used in this calculation, due to turbulent processes, localised density enhancements and/or the anisotropic distribution of neutral atoms in the vicinity of the Earth (Hodges, 1994).

Higher levels of geocoronal SWCX emission would have been expected had XMM-*Newton* been observing a target that required a pointing vector that intercepted the area of highest X-

ray emission, namely around the subsolar point (defined as the position of the magnetopause on the sunward side of the Earth-Sun line, Robertson & Cravens 2003a; Robertson et al. 2006). The solar wind flux during Obs301 was so high that the magnetopause was pushed close to the Earth as a result of the balance between the pressure of the solar wind and that of the Earth's magnetic field. Therefore, only a very small proportion of the line-of-sight of XMM-*Newton* intersected the magnetosheath region, for a large proportion of the observation. The remainder of the line-of-sight intersected undisturbed solar plasma. There was a sufficient density of neutral donor atoms outside of the bow shock, interacting with a particularly dense solar plasma, that a significant contribution to the SWCX signal originated from this region, even though beyond the bow shock the solar wind has not been slowed considerably or the density increased as it would have been within the magnetosheath. The SWCX emission in this case was emitted from both before and just beyond the bow shock boundary. Clearly in cases where XMM-*Newton* does not have an optimal view through the magnetosheath there is still the possibility of detecting SWCX emission from the local region.

## 7.6 Upstream density pulse

In Figure 7.10 we plot the ACE and *Wind* proton density lightcurves. We include on the plot the combined XMM-*Newton* EPIC instrument flare-filtered lightcurve, between 0.5 and 0.7 keV. The EPIC lightcurve shows the same general temporal behaviour as the enhancements in solar proton density measured by both ACE and *Wind*.

The offset in time between the signals at ACE and *Wind* is explained by the separation between the solar wind monitoring spacecraft. We are unable to determine the moment when the signal first crossed into the field of view of XMM-*Newton*, as the XMM-*Newton* data had to be heavily filtered for soft proton contamination at the beginning of the observation.

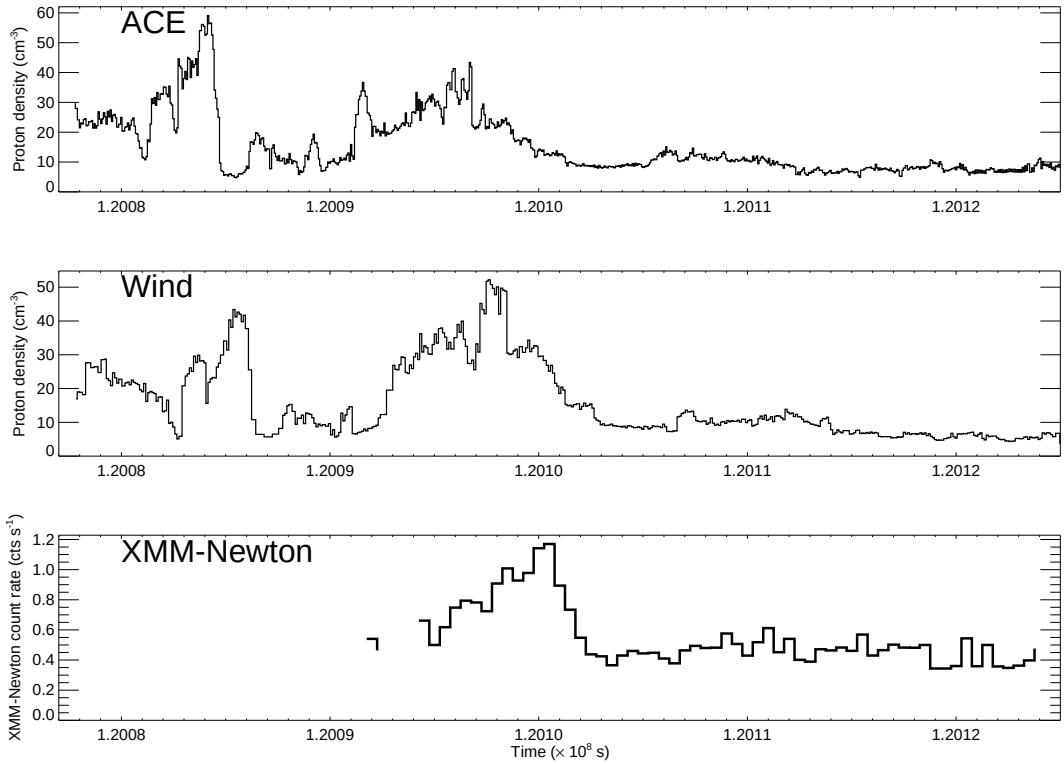


**Figure 7.10:** ACE and *Wind* solar wind proton densities plus XMM-*Newton* combined EPIC instrument (0.5 to 0.7 keV, oxygen emission line-band) lightcurve (panels top to bottom) prior to and during Obs301. The XMM-*Newton* lightcurve has been flare-filtered using the method described in the text.

The shape of the lightcurve seen by *Wind* is not exactly the same as that seen by ACE, so we infer that some evolution of the CME may be occurring or that there are local inhomogeneities within the CME wavefront although the bulk movement is fairly constant. The shape of the XMM-*Newton* lightcurve suggests some level of averaging along the XMM-*Newton* line-of-sight and so a delay calculated between the lightcurve from *Wind* and that from XMM-*Newton* is of limited use as it will be distorted by this averaging. It must also be kept in mind that the proton density is only a proxy for the ion density of the solar wind. From the positions of the spacecraft we are able to ascertain that the CME wavefront extends at least $25\,R_E$ in the GSE-Y direction. We have shown that SWCX emission is non-zero throughout the XMM-*Newton* observation, however we assume that the major bulk of the CME has passed by a time at $T = 1.2012 \times 10^8$ s. If we take the start of the CME wavefront to be at approximately $T = 1.20085 \times 10^8$ s travelling at an average speed of $647\,km\,s^{-1}$, the CME extends a minimum of $3500\,R_E$ in the GSE-X direction.

As the solar proton density lightcurves from both ACE and *Wind* showed the same shape we conclude that the same density enhancement was received at both these solar wind monitors and subsequently XMM-*Newton*. We assume a planar wavefront for the enhancement, which is a reasonable assumption at a distance of 1 AU for a CME (Zurbuchen & Richardson, 2006). Following a similar analysis to that of Collier et al. (2005) and Collier et al. (1998) the orientation of the passing wavefront could be derived using the delay between the signal received at ACE and that received by *Wind*.

Using a discrete correlation function algorithm (Edelson & Krolik, 1988) applied to the ACE and *Wind* proton density lightcurves (Figure 7.10), we calculate the delay between the signal received at the first and then by the second spacecraft. This method normalises the two lightcurves by subtracting the mean from each and dividing by the standard deviation, resulting in lightcurves $l_1$ and $l_2$ (with errors $e_1$ and $e_2$ and standard deviations $\sigma_1$ and $\sigma_2$). Then for each pair of points we calculated the un-binned discrete correlation (Equation 7.4):

$$u_{i,j} = \frac{l_{1,i} \times l_{2,j}}{\sqrt{(\sigma_1^2 - e_{1,i}^2) \times (\sigma_2^2 - e_{2,j}^2)}} \tag{7.4}$$

The time difference or lag ($\tau$) between each pair of points is calculated. We bin up the values $u$ for each value of $\tau$, sum all the values in each bin and normalise by the number $n$ in that bin, to calculate the discrete correlation function $dcf(\tau)$ (Equation 7.5):

$$dcf(\tau) = \frac{\sum^{n} u(\tau)}{n} \tag{7.5}$$

The maximum of the resulting $dcf(\tau)$ distribution gives the delay between the signal in the two lightcurves.

Based on the period of the solar proton density enhancement between $T = 1.2009 \times 10^8$ s and $T = 1.2011 \times 10^8$ s, we find a delay of 26$\pm$1 minutes from ACE to *Wind*. The two spacecraft are separated by $d_{par}$ along the Earth-Sun line and by $d_{per}$ perpendicular to this line. For a wavefront travelling along the Earth-Sun line for a distance $d_{par}$ at the average speed (v) mentioned above, this results in a simple delay time ($\tau_{con}$) of 29 minutes from ACE to *Wind*.

If the wavefront passing from the first spacecraft (ACE) to the second (*Wind*) was planar, then given the speed and the delay observed between the signals ($\delta\tau_{obs}$), the distance (d$'$) between them would simply be (Equation 7.6):

$$\mathrm{d}' = v \times \delta\tau_{obs} \tag{7.6}$$

This is less than the $d_{par}$, therefore the wavefront is tilted at an angle ($\theta$) so that the signal reaches the second spacecraft before the simple case of a planar wavefront moving along the

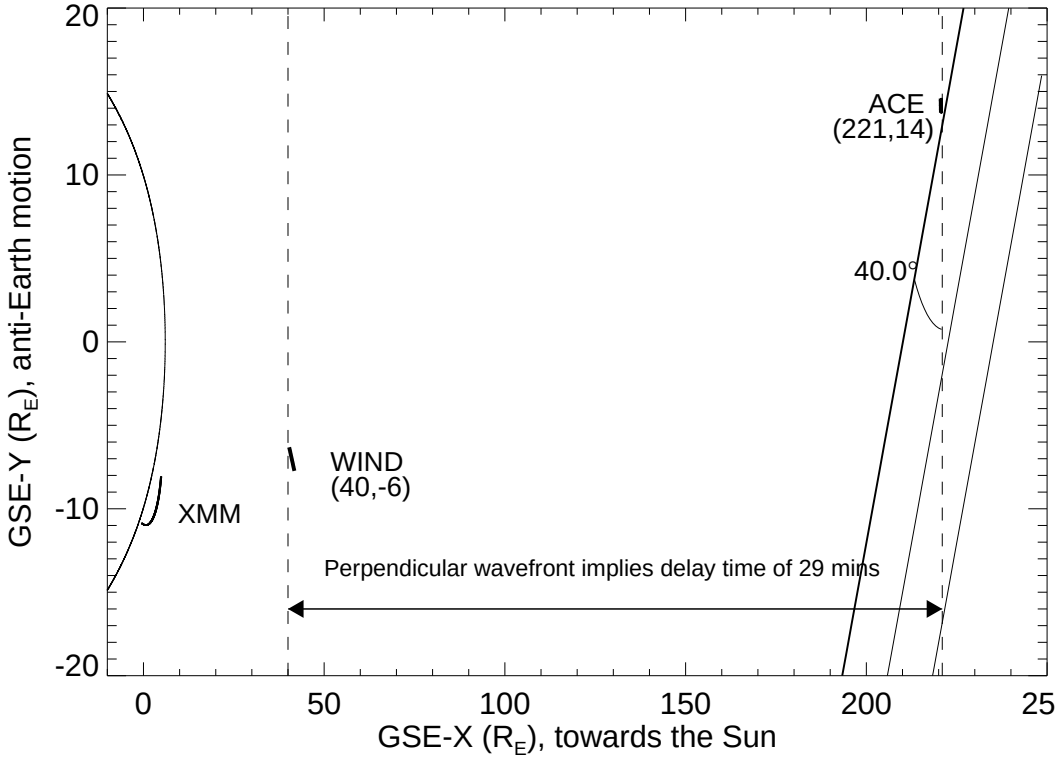


**Figure 7.11:** XMM-*Newton*, ACE and *Wind* positions at the time of Obs301, in GSE-coordinates in the ecliptic plane. Spacecraft positions in brackets are given in units of $R_E$. The position of the magnetopause, as calculated using the Shue et al. (1998) model, is shown for the start of Obs301. The dashed lines are used to aid visualisation and the wavefront is represented by the tilted solid lines.

Earth-Sun line (Equation 7.7).

$$\tan\theta = \frac{d_{par} - d'}{d_{per}} \tag{7.7}$$

We calculate that a tilted wave front at approximately 40 degrees would have passed in the vicinity of the Earth and XMM-*Newton*. In Figure 7.11 we plot the position of ACE, *Wind* and XMM-*Newton* at $T = 1.2009 \times 10^8$ s of Obs301.

## 7.7 Summary

We consider the possibility that the SWCX enhancement of Obs301 is linked to the CME event of the 19th October 2001 (Wang et al., 2005). The delay between the occurrence of the CME at the solar corona and its arrival near Earth would be approximately two and a half days. Increased solar proton fluxes were registered by both ACE and *Wind* and therefore this plasma cloud would have passed in the immediate vicinity of the Earth. It is not always the case that enhancements in solar proton fluxes, and any accompanying highly charged ions, are registered by increased incidents of soft proton flaring or SWCX enhancements by XMM-*Newton*. However, the arrival of the peak of the low energy enhancement as seen by XMM-*Newton* is consistent with the delay expected as the feature passes in sequence from ACE to *Wind*, on to a region intersected by the line-of-sight of XMM-*Newton*.

We have shown that line emission from O VIII is very prominent and dominates that of O VII, contrary to signatures of heliospheric SWCX (Koutroumpa et al., 2009b). We have also shown in our spectral analysis that the observed flux from SWCX emission is much greater than that from a simple estimate of the expected emission, based on the abundances of a slow solar wind. Also, mid-energy emission lines in the regime 0.70 to 2.00 keV infer the presence of highly charged states of iron, as is often seen in a CME (Zurbuchen & Richardson, 2006; Zhao et al., 2007). We see no significant compositional changes in the line emission over the duration of the XMM-*Newton* observation. In addition, we have observed emission at 2.00 keV from highly charged states of silicon, implying a very high temperature plasma. A CME, rather than a steady state solar wind, would explain the large enhancements, flux observed and the richness of the spectrum as seen by XMM-*Newton*. This case is the richest spectrally of those examined in both Paper I and Paper II.

CMEs have been used to explain the results of other X-ray observations in the literature pertaining to the diffuse X-ray background. Henley & Shelton (2008) invoked a CME to

explain differences between results obtained from XMM-*Newton* and *Suzaku*, when determining Halo and Local Bubble X-ray spectra. They also observed emission from Mg XI and Ne IX, although emission lines from oxygen were less significant. They attribute this emission to a possible localised enhancement in solar wind density crossing the line-of-sight of XMM-*Newton*. Smith et al. (2005) attributed the anomalously high level of O VIII seen in their observation of a nearby molecular cloud to SWCX, and noted this was unlikely to be due to SWCX from a steady-state solar wind. Instead they conclude that their enhancement was due to charge exchange from a CME and the interstellar medium, probably at a distance of a few AU from the Sun, due to the depletion of neutral gas available for charge exchange near the Sun. We eliminate the possibility that the emission seen in Obs301 is due to SWCX occurring at the heliospheric boundary or at a large distance from Earth. Short-term variations can occur for heliospheric SWCX, especially if observing along the helium focusing cone (Robertson & Cravens 2003a,b), but the pointing of XMM-*Newton*, which does not intersect the region of peak emission from this area, argues against this case. In addition, the abundant emission line spectrum and the variations in the fluxes of the major ions in the spectrum which reflect the variations in solar proton flux support a geocoronal occurrence of SWCX. We conclude that the SWCX interaction we have observed occurs between ions from a CME and neutrals in the exosphere of the Earth, at a relatively close distance to the Earth, but not confined to the magnetosheath within the bow shock.

Although data regarding the ion states of the solar wind for the period of Obs301 from the solar wind monitors ACE and *Wind* are sparse, we have been able to identify ions from a rich set of emission lines from a passing CME. Not all CMEs detected by ACE will be detected by *Wind*, or indeed intersect the line-of-sight of XMM-*Newton*. XMM-*Newton* was not optimised to study the magnetosheath or near Earth regions. However, we have shown that XMM-*Newton* can be used to provide additional compositional information of the solar wind plasma, especially for the highest charge state ions, to that obtained by upstream solar wind monitors, providing the observing geometries and inclinations of the incoming wave

fronts are favourable.

Chapter 8

# Modelling of SWCX emission

The expected X-ray emissivity of SWCX emission from the solar wind interaction with the magnetosheath can be estimated from the integrated emission along the line-of-sight for the observer. We have developed a model, applicable to local interplanetary space, to calculate this emission. In this chapter, we model the expected exospheric-SWCX X-ray emission for each of the observations of the SWCX set. The work here results from a modification to the model described in Section 7.5. The expected X-ray emission in this adapted model is time dependent and as previously, depends on upstream solar wind parameters as measured by the solar wind monitor ACE.

We only calculate the expected exospheric-SWCX emission and have not attempted to include any contribution from further into the heliosphere, as to increase the integration length would lead to greater uncertainty in the underlying parameters of the solar wind on large spatial scales. We assume that the solar wind parameters used in the model are approximately constant (excluding the magnetosheath region) along the line-of-sight. The emissivity expected (Cravens, 2000) is given by Equation 7.1 as previously described in our study of a passing CME.

For each observation under study in the SWCX set, we wish to test whether any relationship exists between the total SWCX flux seen and the theoretical integrated X-ray emission along the line-of-sight (see Equation 7.2).

We take data describing the conditions in the solar wind from ACE (*Level 2* processed data, merged instrument data using hourly averages) at the time of each observation. We needed to apply a delay to the signal received, to account for the separation between ACE and the Earth. This delay will be time variable and will depend on the speed and orientation of the solar wind. However, as a first approximation, we have taken the average solar proton speed of the data and assumed a planar wavefront travelling anti-sunward perpendicular to the GSE-X axis. We calculate and apply to the delay required for the wavefront to travel from ACE to the Earth. This is a reasonable assumption given that the majority of the SWCX emission will originate from close to the Earth and given the 1 ks integration time of the X-ray lightcurve.

Throughout this work we assume a geocentric solar-ecliptic coordinate system (GSE), where positive X is directed from the Earth to the Sun, positive Y opposes planetary motion and positive Z is parallel to the direction towards the north ecliptic pole, as described in previous chapters.

## 8.1 Construction of the model

For each time bin of an observation (1 ks binning):

- We extract the solar wind bulk proton velocity ($u_{sw}$) and temperature ($T$) from the ACE data, and for these parameters we calculate a thermal velocity and average speed, using Equations 8.1 and 8.2:

$$v_{th} = \sqrt{3k_bT} \tag{8.1}$$

$$\langle g \rangle = \sqrt{v_{th}^2 + u_{sw}^2} \tag{8.2}$$

- We estimate the position of the magnetopause, based on the model of Shue et al. (1998). To do this we use information regarding the strength and direction of the interplanetary magnetic field ($B_z$ component, given in units nT) and the dynamic pressure ($D_p$, given in units nPa). The standoff position ($M_{so}$) of the magnetopause and flaring factor $f$ are shown in Equations 8.3 and 8.4. The distance ($r$) to the magnetopause is then given by Equation 8.5, where $\theta$ is the solar zenith angle. We assume that the magnetopause shape is symmetrical about the GSE-X axis and place the magnetopause standoff distance along this axis.

$$M_{so} = \{10.22 + 1.29 tanh\,[0.184(B_z + 8.14)]\}(D_p)^{-\frac{1}{6.6}} \tag{8.3}$$

$$f = (0.58 - 0.007B_z)\,[1 + 0.024ln(D_p)] \tag{8.4}$$

$$r = M_{so}\left(\frac{2}{1 + cos\theta}\right)^f \tag{8.5}$$

- Using the magnetopause location as a guide, we approximate the position of the bow shock. We base the shape on a simple parabola and calculate the bow shock standoff distance ($B_{so}$) using the solar wind pressure (calculated from the parameters of the solar wind density $\eta_{sw}$ and speed $u_{sw}$) and the relationship in Khan & Cowley (1999), expressed in Equation 8.6. The magnetopause and bowshock together define the magnetosheath region.

$$B_{so} = \frac{162}{(\eta_{sw} u_{sw}^2)^{\frac{1}{6}}} \tag{8.6}$$

- We create an Earth-centric square image for use in subsequent steps. The side length of the image is $200\,R_E$. This image is divided into cells, with side length $0.5\,R_E$ ($\sim$3150 km). The magnetosheath shape is projected onto this image. We are able to use an image rather than a cube due to the assumption made previously regarding the symmetry of the magnetosheath shape about the GSE-X axis.

- We find the neutral density of hydrogen atoms for each cell. We use the Østgaard et al. (2003) model for neutral hydrogen density profiles around the Earth, but limit this to a minimum density of $0.4\,\mathrm{cm}^{-3}$ (Fahr 1971, approximate neutral hydrogen density for upwind of the interstellar hydrogen flow). The Østgaard et al. (2003) model of the neutral hydrogen density is valid above $3.5\,\mathrm{R_E}$, which is sufficiently close to the Earth for our modelling efforts, due to the restrictions on the viewing angle of XMM-*Newton* as described in previous chapters. Although the neutral hydrogen model was developed from night-side data taken by the IMAGE satellite, we assume this profile is radially symmetric and take parameter values for a solar zenith angle of 90°. The radial profile of the neutral density used is shown in Figure 8.1. In this figure we also plot the Hodges (1994) profile, which has been approximated by a simple $r^{-3}$ relationship, also limited by the same minimum density value. The neutral density profiles about the Earth are described in more detail in Section 3.3.

- We determine the line-of-sight of the XMM-*Newton* pointing through the grid by extracting the relevant information from the ODF and converting the positions and target pointing direction to the GSE coordinate system.

- We find the velocity and density of the solar wind for each cell, (Spreiter et al. 1966, K.D. Kuntz private communication). As the solar wind passes the bowshock and enters

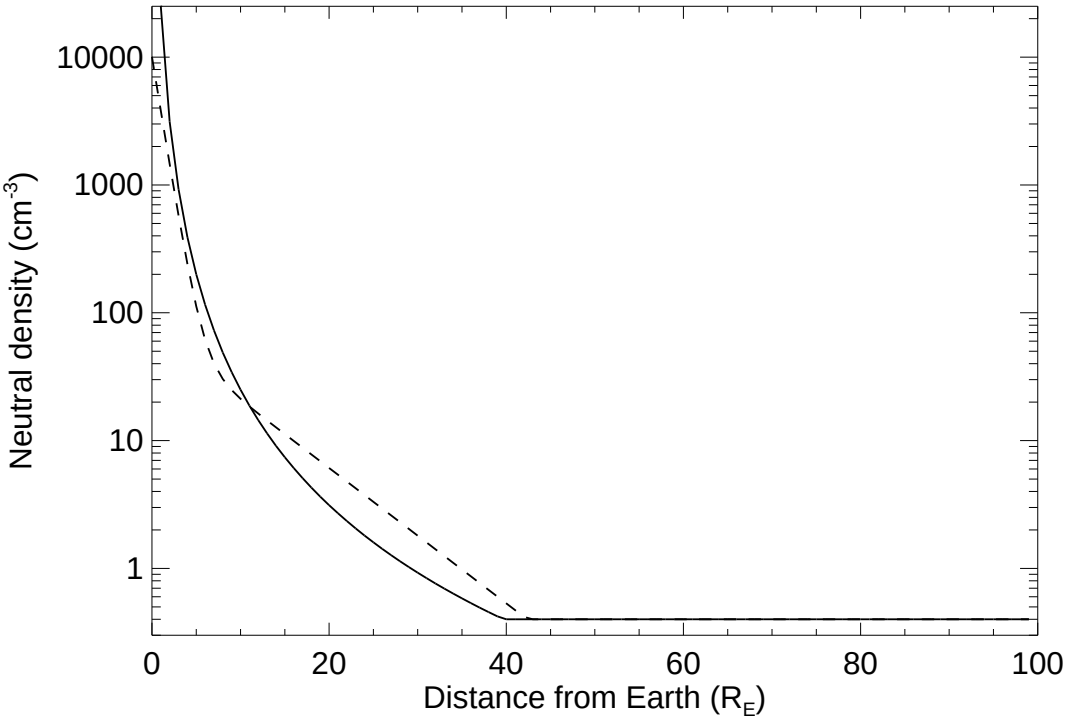


**Figure 8.1:** Exospheric neutral hydrogen density profiles, using an adapted Hodges (1994) (solid line) and a Østgaard et al. (2003) (dashed line) model.

the magnetopause its density increases (by about a factor of four in the subsolar region, as compared to the unperturbed value), and the velocity drops to about one tenth.

- The value of $\alpha$ is dependent on the abundances of the ion species contributing to the charge exchange process, along with the cross-section and energy of each interaction with the neutral donor in the energy band of interest. The neutral donor is hydrogen in the geocoronal case. The relative abundances found in the solar wind vary considerably with solar wind state. As described in Chapter 3, the composition of the solar wind generally follows abundances seen in the photosphere, but can vary by up to a factor of about 2 (fast wind) or 4 (slow wind) for elements with first ionisation potential (FIP) below the Lyman-$\alpha$ limit of 10.2 eV (Richardson & Cane, 2004, and references therein). However, we use the slow solar wind abundances for an ion species with respect to oxygen, as listed in Schwadron & Cravens (2000). We use an oxygen to hydrogen ratio of 1/1780 for solar wind speeds of $\leq 650\,\mathrm{km\,s^{-1}}$ or 1/1550 for speeds

above this threshold. For this modelling we consider contributions to the emission from the principal and minor transitions as described in Chapter 6. Cross-sections for charge exchange transitions are dependent on solar wind speed. We calculate an $\alpha$ map with the same dimensions and binning as that of the Earth grid and populate this map with values of $\alpha$ depending on the speed of the solar wind, unperturbed outside of the magnetosheath or perturbed inside the magnetosheath as described above. The value of $\alpha$ can be calculated using Equation 7.3 as shown in Chapter 7.

- We multiply the solar wind velocity, solar wind density and neutral hydrogen density together for each of the cells in the line-of-sight and multiply this value by the efficiency factor $\alpha$ for each cell. This is the emissivity of each cell.
- We sum all cells in the line-of-sight, accounting for the number of cells included in the integral, to give the value of the emissivity metric, approximating Equation 7.2.

There are some known limitations to this model, such as:

- There are no magnetosheath cusps (increased density or modifications to the velocity of the solar wind specific to these regions) included in the Spreiter approximation
- The neutral hydrogen has been modelled as spherically symmetrical about the Earth. However, there may be density enhancements or depletions in regions of the exosphere.
- The abundances of the solar wind are not constant, but will change for example with the phase of the solar cycle or the injection of plasma from a CME.
- The magnetopause and bow shock standoff distances have been assumed to be on the GSE-X axis, this may not often be the case.
- The interstellar neutral density may be significantly different from that of the approximate limiting density applied in this model.

We also consider an adapted model, whereby the $\alpha$ calculated is dependent on the relative abundances of $O^{6+}$ and $O^{7+}$. We use the ratio of these ionisation states, taken from the ACE merged, hourly-averaged data sets to re-calculate the abundance of $O^{7+}$ assuming the initial $O^{6+}$ and $O^{7+}$ abundances as found in Schwadron & Cravens (2000). We then re-calculate the value $\alpha$ and the subsequent line-of-sight flux. These results will be referred to as the Model-2 results and will be discussed alongside the results of the fixed $\alpha$ model (as described above) later in this chapter.

A schematic of an example line-of-sight of XMM-*Newton* through the magnetosheath and to illustrate the steps above is shown in Figure 8.2.

## 8.2 General model results

Modelled lightcurves were produced for each SWCX case when there were data available from ACE. We split the modelled emission based on the time periods used for the creation of the spectra in Chapter 5. The resultant flux is the difference between the mean modelled flux during the SWCX-affected and the SWCX-free periods. A histogram of the modelled fluxes is given in Figure 8.3 (top panel), along with a scatter plot showing the observed flux versus the modelled resultant flux for each exospheric-SWCX case (bottom panel). There is a very weak, but positive correlation between the modelled and observed flux, with a correlation coefficient of 0.27. However, 76 out of 95 cases (that complete the modelling procedure), have a positive modelled flux. Under the null hypothesis that the modelled flux is equally likely to be negative or positive, the probability of the observed outcome is $\sim 1.5 \times 10^{-9}$. Negative modelled fluxes happen when the SWCX-affected period, as determined using an enhancement seen in the observed line-band lightcurve, occurred in the opposite period to the maximum expected modelled flux. The enhancement in the observed line-band lightcurve occurred sufficiently far away in time from any peak seen in the modelled X-ray

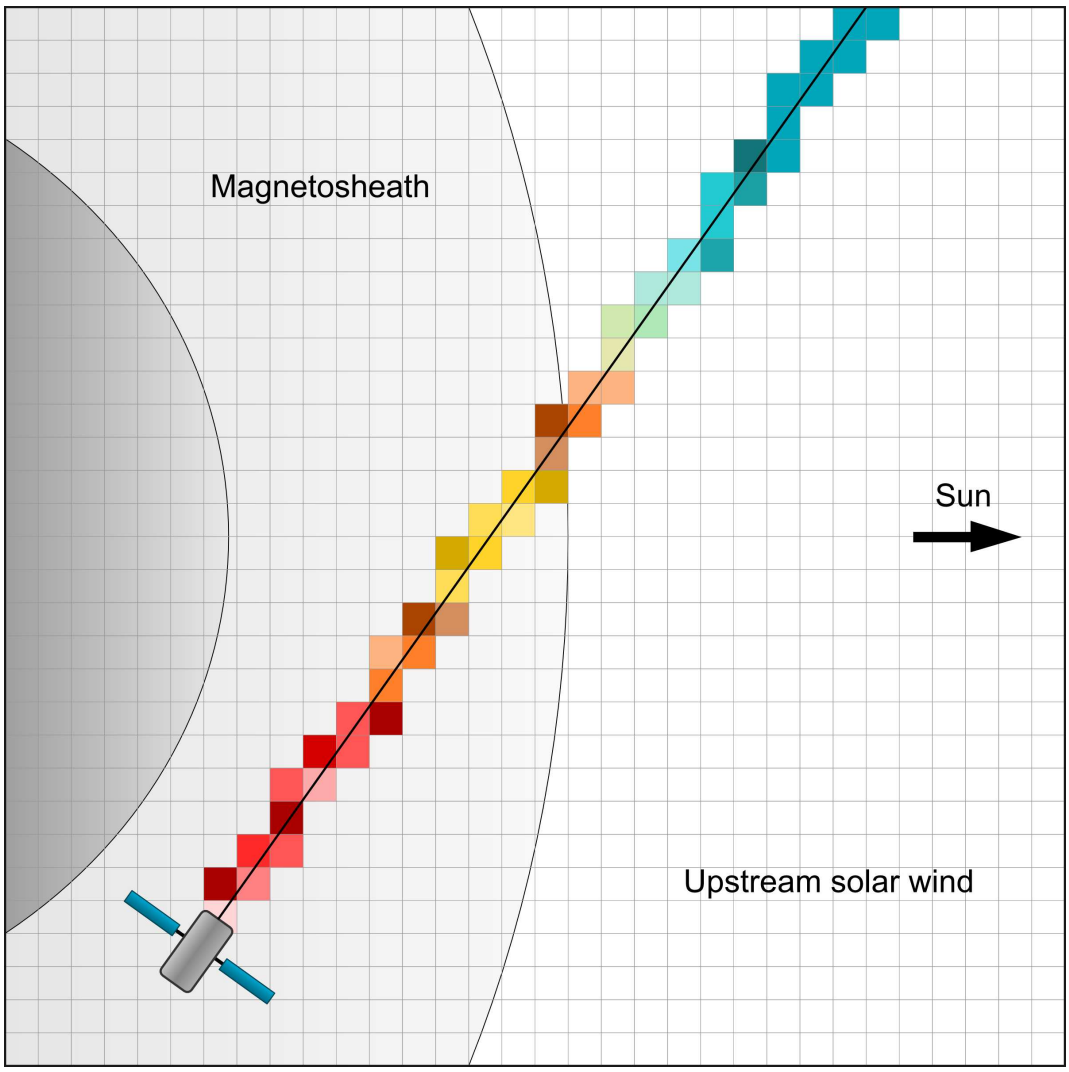


**Figure 8.2:** Schematic of the model, showing an example line-of-sight pointing through a magnetosheath of shape determined by the solar wind conditions at the time of the XMM-*Newton* observation. The position of XMM-*Newton* is marked by the satellite symbol. The colours in the cells intersected by the line-of-sight are coloured to approximate the magnitude of expected emissivity in those cells (e.g. yellow for the highest emissivity, red for intermediate emissivity and blue for the lowest emissivity).

flux lightcurve.

In Figure 8.4 (left-column) we show modelled lightcurves for the three top new cases of Table 4.1. Contributions from the model were only taken for the periods where there were counts in the XMM-*Newton* lightcurves (periods not removed during the filtering process). Example lightcurves of cases where the resultant modelled flux is negative are given in the first two panels of the second column of Figure 8.4. We also plot a modelled lightcurve when SWCX was not detected (below the thresholds for $\chi^2_\mu$ and $R_\chi$) in the bottom-right panel of the same figure. In this case the line-band lightcurve does not vary significantly. The modelled emission in this case is small compared to the SWCX cases presented in the other examples.

## 8.3 Comparison of modelled and observed lightcurves

We wished to test how well the individual modelled flux lightcurve tracked that of the line-band lightcurve for each observation. We also wanted to determine the most dominant parameter in the modelling of the expected emission. To do this we applied principal component analysis to the model versus the line-band lightcurve and the model versus the solar wind flux. We calculate the correlation matrix between a linear fit to the relationship between each pair of values, for each exospheric-SWCX case. We calculate the correlation rather than the covariance matrix as the scale ranges of the data differ by a large amount and so by using the correlation coefficients we standardise the data. We use the primary eigenvalue of this matrix to calculate the percentage contribution along the assumed linear relationship between these lightcurves. Histograms of these percentage contributions can be seen in Figure 8.5. The histogram (left) shows that the X-ray lightcurve is generally correlated with the modelled lightcurve, as the first principal component percentages are high (with a mean of 73.7%). The histogram (right) also shows high first principal component percentages (with a mean of 73.6%), which suggests that in the vast majority of cases the model is dominated by the in-

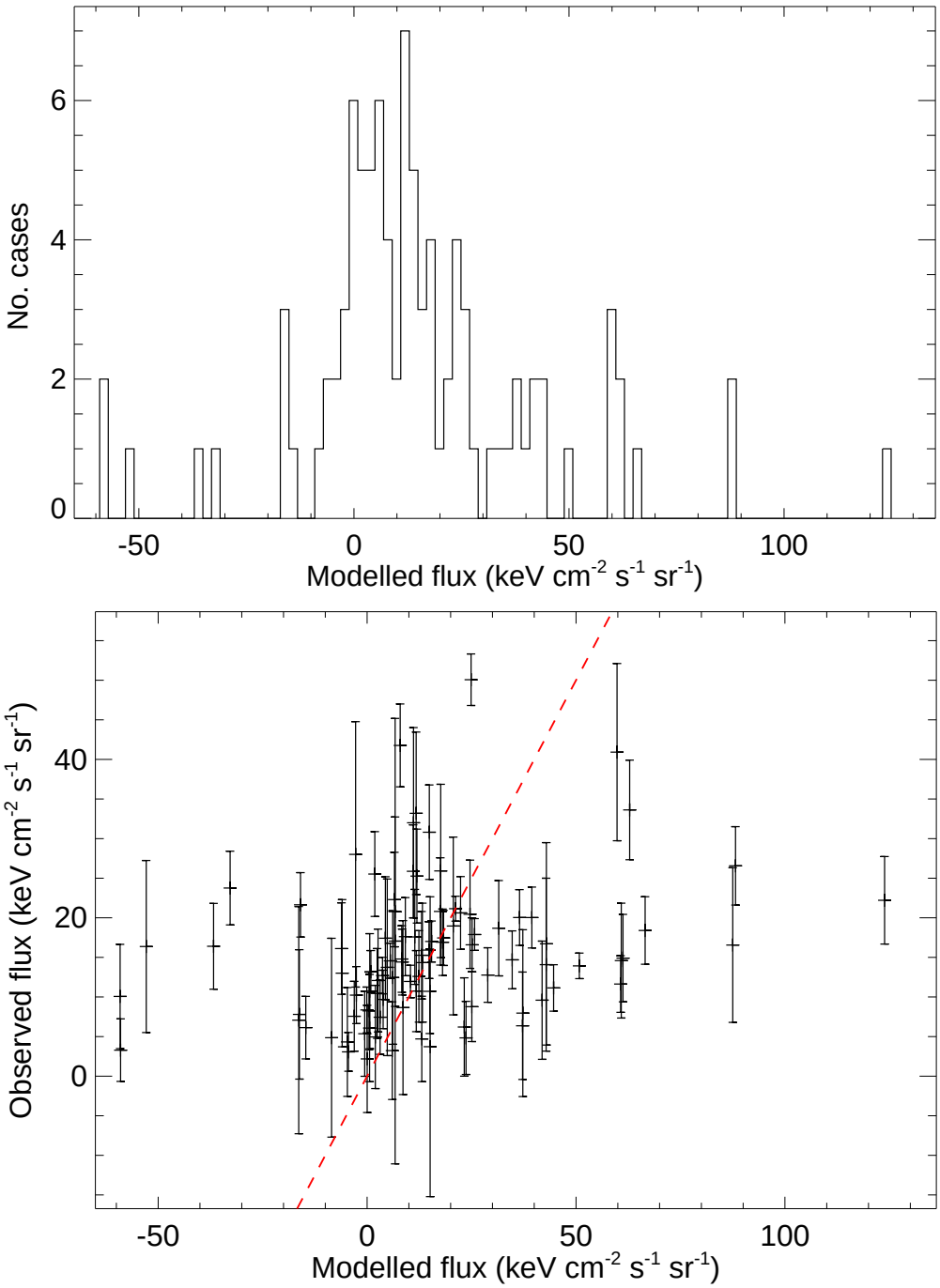


**Figure 8.3:** Top: histogram of the modelled fluxes. Bottom: observed flux (0.25 to 2.5 keV) versus the modelled flux for the SWCX set. A line (dashed, red) of gradient unity has been added to the graph to aid the eye.

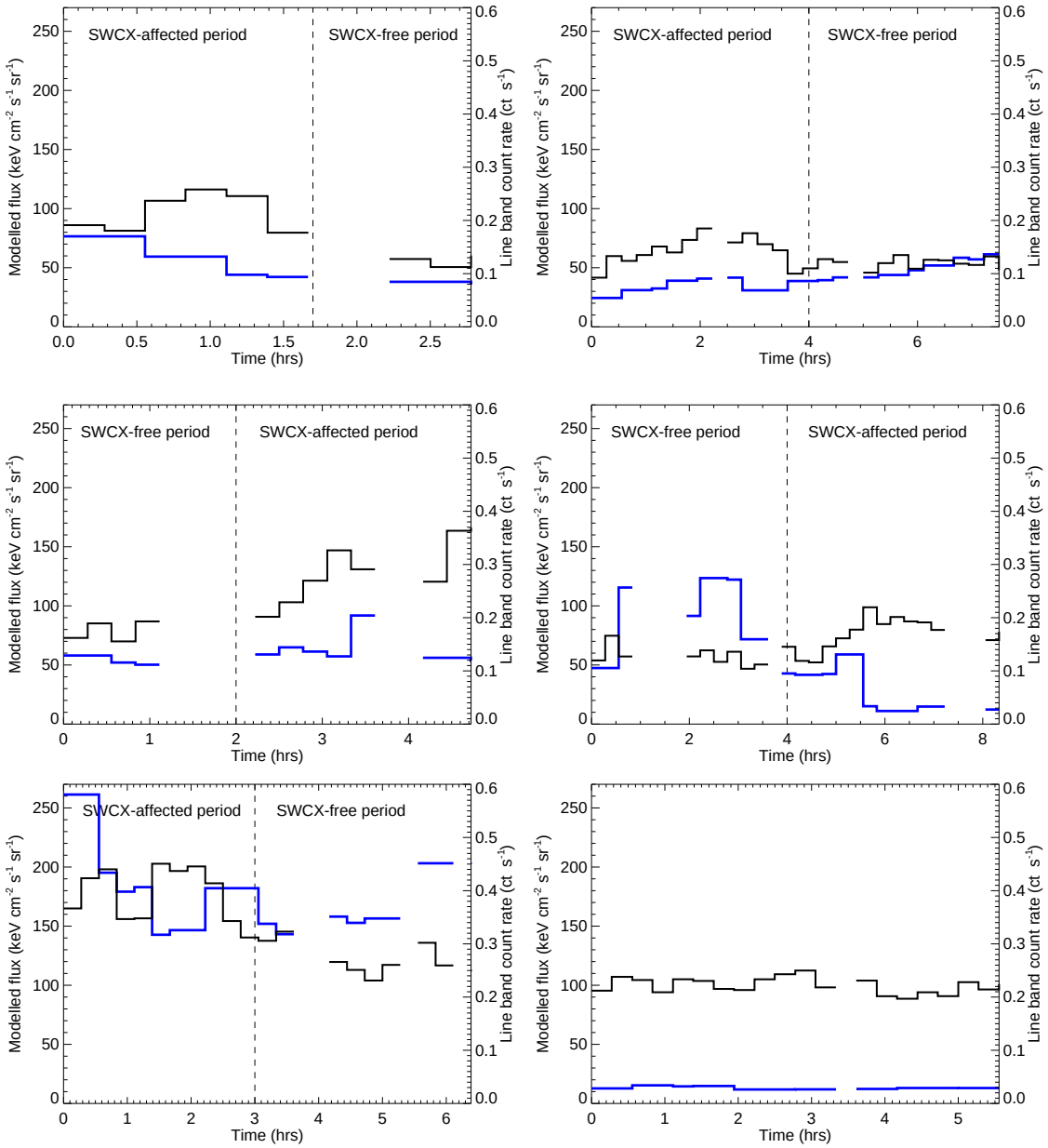


**Figure 8.4:** Example modelled (blue, in keV cm$^{-2}$ s$^{-1}$ sr$^{-1}$, left-hand y-axis) and XMM-*Newton* line-band (black, ct s$^{-1}$, right-hand y-axis) lightcurves. Observations with identifiers 0150610101 (top-left), 0054540501 (middle-left), 0113050401 (bottom-left) show the model lightcurve generally following the shape of the XMM-*Newton* lightcurve. Observations with identifiers 0141150101 (top-right) and 0150320201 (middle-right) show the modelled lightcurve peak in a different period to the XMM-*Newton* lightcurve and 0301410601 (bottom-right) is an example from an observation without a SWCX enhancement. Five panels show the split between the SWCX-affected and SWCX-free periods (vertical dashed line).

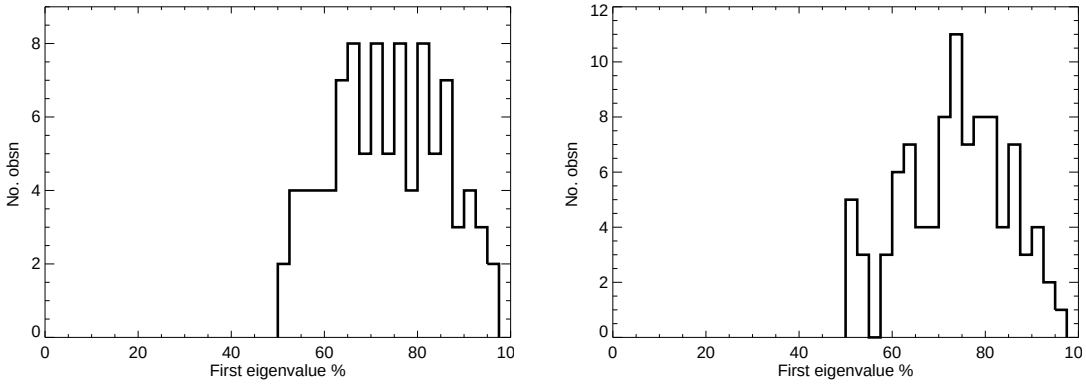


**Figure 8.5:** Histograms of the first eigenvalue's percentage contribution to the total, for the modelled emission versus the XMM-*Newton* line-band lightcurve (left) and versus solar wind flux (right).

coming solar wind flux. The lowest eigenvalue when comparing the modelled emission to the line-band lightcurve occurred for the observation with the identification number 0101440401. Modelled and line-band lightcurves for this case are shown in Figure 8.6. We also plot the component lightcurves that make up the total modelled lightcurve from within the magnetosheath and from beyond the bow shock. The contributions from the magnetosheath region in this case dominates the modelled lightcurve. XMM-*Newton* is found anti-sunward of Earth during this observation and so the line-of-sight of XMM-*Newton* passed through the flanks of the magnetosheath. This region is less well defined in our model due to the approximations of the shape of the bowshock boundary and the extrapolation of the values used to perturb both the solar wind density and velocity in this region. The overall modelled emission was very low for this case, compared with the top-row cases of Figure 8.4.

## 8.4 Line-of-sight through the magnetosheath

In Figure 8.7 (top panel) we plot the modelled resultant flux versus the average length of the line-of-sight through the magnetosheath (between the magnetopause and the bow shock), during an observation. In Figure 8.7 (bottom panel) we present the observed flux versus the average length of the line-of-sight through the magnetosheath. There is no discernible

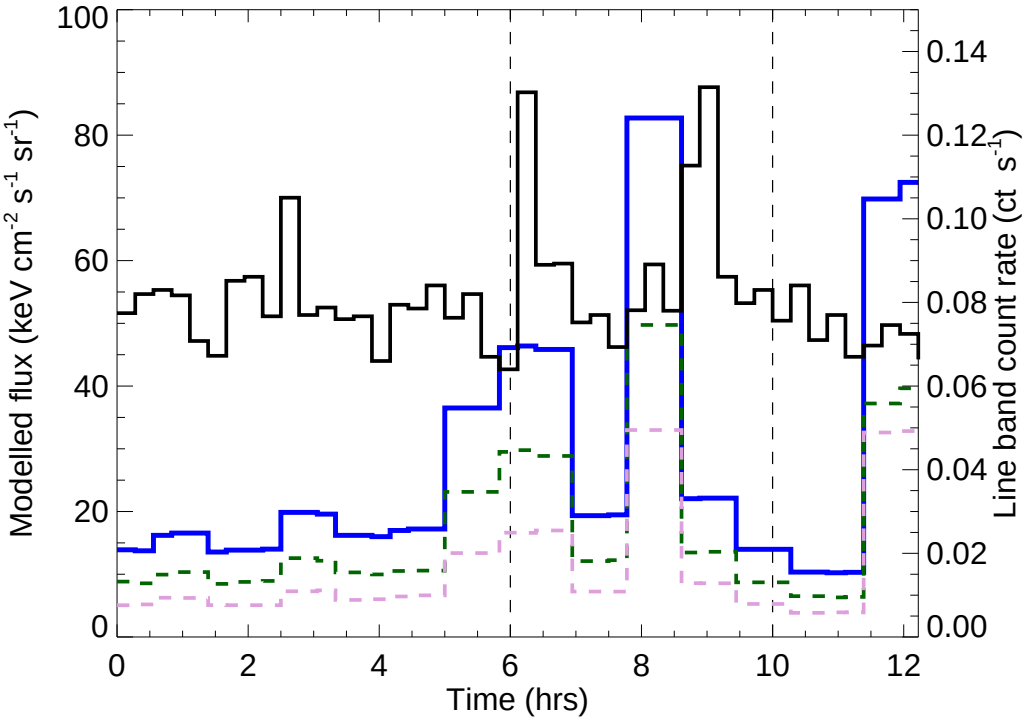


**Figure 8.6:** Example modelled lightcurve (blue, left-hand y-axis) with the XMM-*Newton* line-band (black, right-hand y-axis), for the case where the first eigenvalue percentage contribution was the lowest when comparing the modelled and XMM-*Newton* lightcurves. The contribution to the modelled lightcurve from the magnetosheath (green-dashed) and region past the bow shock (plum-dashed) are also shown. The SWCX-affected period was taken between the vertical dashed lines.

general relationship between the modelled or the observed flux with the length of line-of-sight through the magnetosheath.

## 8.5 Fractional difference

We investigate when the model and observed fluxes are discrepant by calculating the fractional difference between the observed and modelled fluxes ((observed-modelled)/observed flux). In Figure 8.8 (top panel) we plot this fractional difference versus the maximum solar wind flux during each observation, along with a histogram of the fractional difference values. The mean of these fractional differences was +0.17 and the modal bin of the histogram was for values between 0 and 1. A large proportion (approximately 60%) of the modelled cases had a fractional difference between -1 and 1. The most discrepant cases occurred when the solar wind flux was low (compared to the maximum solar wind flux of these exospheric-SWCX cases). The solar wind plasma flow around the Earth's magnetosheath in these cases has been badly described by the model.

The observation with the largest absolute fractional difference had identifier 0041750101. This case was similar to cases (bottom-left and bottom-right) of Figure 8.4 when the modelled lightcurve peaked in the alternative (SWCX-free) period to the enhancement in the observed line-band lightcurve (SWCX-affected).

We also wished to consider whether the fractional difference was due to some underlying emission with temporal variability occurring in near-heliospheric space, in particular to that of the helium focusing cone (Weller & Meier, 1974). We consider cases within the SWCX set that occur within 10° of the cone's direction (73.9° ecliptic longitude and $-5.6°$ ecliptic latitude, Witte et al. 1996). As the integration length for the model is relatively short compared to the spatial extent of the helium focusing cone and size of Earth's orbit, only

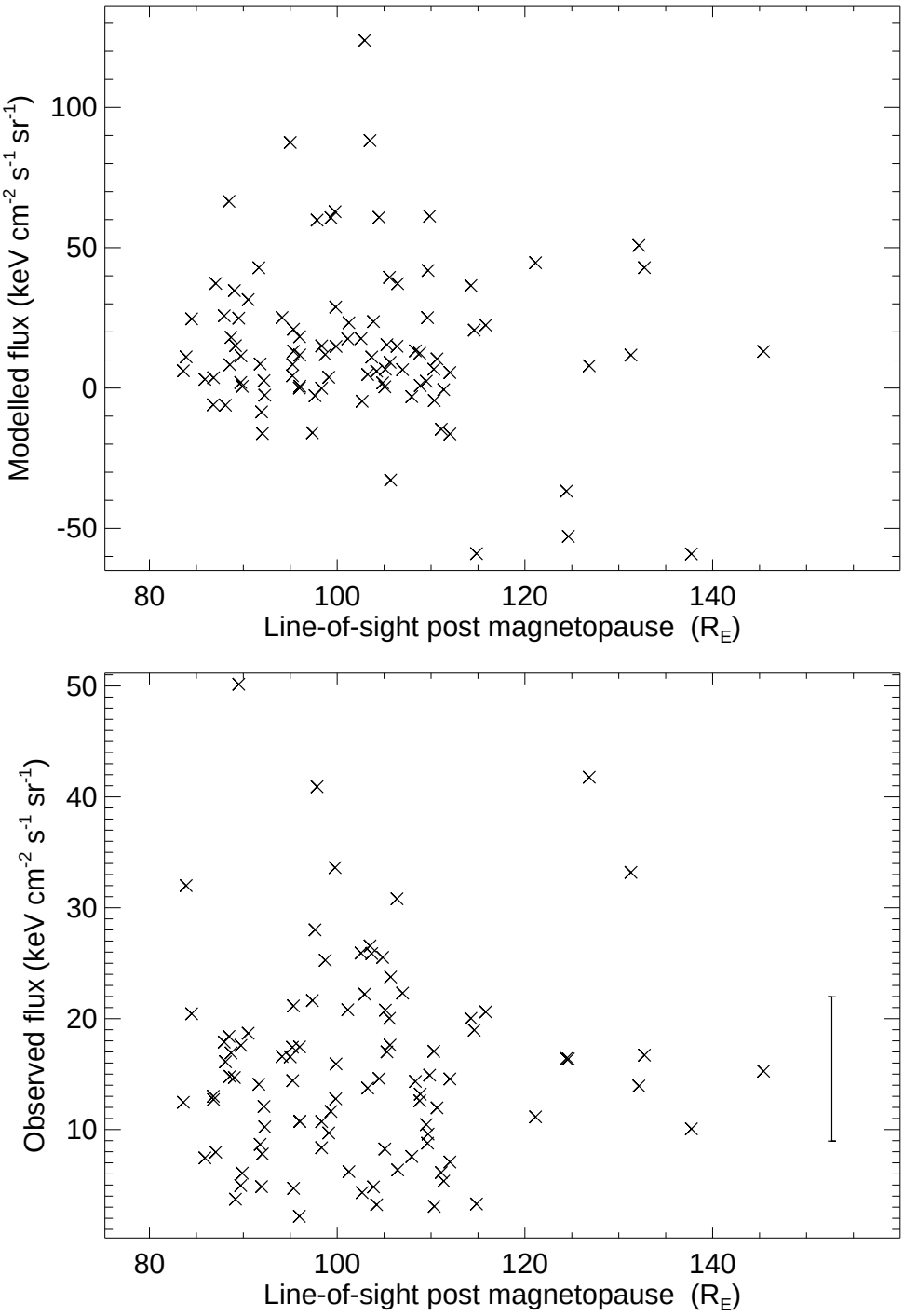


**Figure 8.7:** Line-of-sight length through the magnetosheath versus the modelled flux for the SWCX set (top panel) and the observed flux for the SWCX set (bottom panel). A mean error on the observed flux bar is given to the right of the bottom plot.

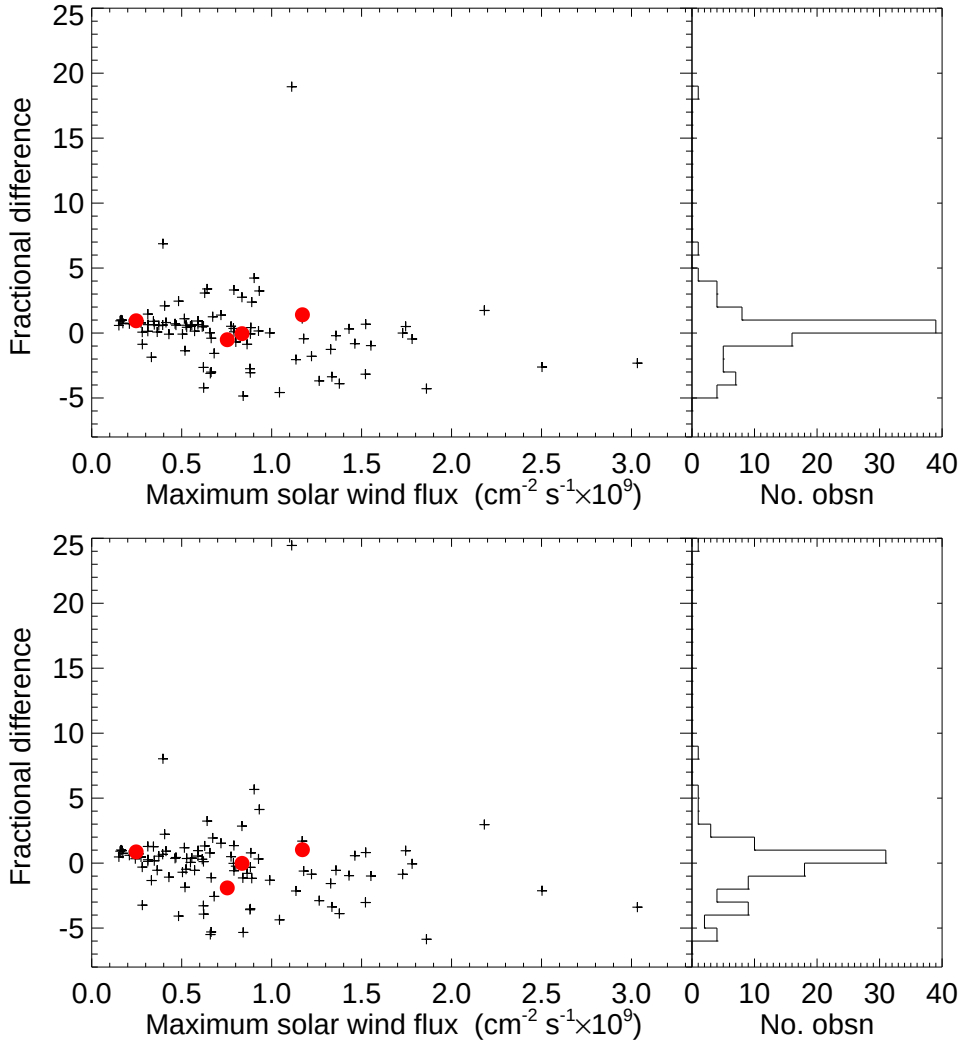


**Figure 8.8:** Fractional difference between (top panel) the observed and modelled flux and (bottom panel) the observed and Model-2 flux, versus the maximum solar wind flux. Also included in each panel is a histogram of the fractional differences. Cases where XMM-*Newton* is found within the helium focusing cone are marked in red.

those observations taken when XMM-*Newton* is within this region are of importance. We find 4 cases within this region. These cases are marked in red on Figure 8.8. A statistical analysis, repeatedly drawing 4 random cases from the SWCX set, indicates that we obtain an average fractional difference for the 4 random cases to be greater than that of the 4 helium focusing cone cases 28% of the time. We therefore have no evidence to suggest that temporal variability originating in the helium focusing cone is a significant component of the observed-to-modelled flux discrepancy.

We also compute the fractional differences between the observed and modelled flux values for the Model-2 results. These are shown in Figure 8.8 (bottom panel). The peak of the distribution lies in the same bin as that of Figure 8.8 (top panel), although there is a greater variance seen in the differences. We conclude that for the SWCX set cases, no benefit has arisen by using a compositionally-variable dependent model as opposed to the simple compositionally-static version of the model. We continue our discussion based on the simple model results only.

We split the fractional difference values into two sets; for cases where this value is $<$ -1.5 or $>$ 1.5 (bad), or any other value (good). In Figure 8.9 we plot histograms of the mid-observation position of XMM-*Newton* (in GSE coordinates, GSE-X, Y and Z) for each observation for the good and bad sets. We performed a Kolmogorov-Smirnov test on the three pairs of good and bad sets. The probabilities that the good and bad sets are drawn from the same sample distribution were 0.22, 0.002 and 0.79 for GSE-X, GSE-Y and GSE-Z respectively, indicating that for the GSE-Y coordinates, the good and bad sets are statistically different. The good set for the GSE-Y positions are skewed towards negative values and there are relatively more observations in the bad set in the positive direction. We repeat the test using mid-observation position of XMM-*Newton* expressed in Geocentric Solar Magnetospheric (GSM) coordinates. These differ from the GSE coordinates as the GSM-Y axis is perpendicular to the Earth's magnetic dipole (the X-axis is unchanged). The Kolmogorov-Smirnov

test results were 0.22, 0.004 and 0.28 for the GSM-X, GSM-Y and GSM-Z respectively. The Y-coordinate result remains significant. Therefore we postulate that the model is better at describing the conditions seen by XMM-*Newton* when the Y-coordinate is negative.

The simplifications used in this model to describe the flanks of the magnetosheath in terms of shape, solar wind density and velocity may mean that the model is less robust in the positive Y-coordinate region. We assumed cylindrical symmetry about the GSE-X axis, however, the magnetosheath will be non-symmetrical in shape, suffering for example magnetosheath erosion along one side of the magnetopause (along the dusk side, Owen et al. 2008), a full discussion of which is beyond the scope of this thesis. The incoming solar wind is expected from the GSE-Y positive direction, determined by the flow of the solar wind along the Parker Spiral as it emanates from the Sun. It is in this region that we expect the greatest differences in shape from the simplified magnetosheath we have used in our modelling steps and it is here that we see the largest absolute fractional differences between the observed and modelled fluxes. It is clear that although the model can estimate the observed flux within a factor of $\sim 2$ in approximately 50% cases, there are still many occurrences when the local physical conditions combine so that the simple model does not explain the observed flux adequately.

## 8.6 Summary

We have produced a time-resolved model to estimate exospheric-SWCX emission for individual pointings of XMM-*Newton*. We base the modelled emission on upstream solar wind parameters and approximate the neutral hydrogen density about the Earth using a simple radially symmetrical profile. A large proportion of the SWCX cases showed an observed-to-modelled fractional difference within the range (-1 to 1). Considerable uncertainties may arise from the assumptions taken regarding the propagation of the solar wind, the magnetosheath shape and perturbations of the solar wind within the magnetosheath region. There

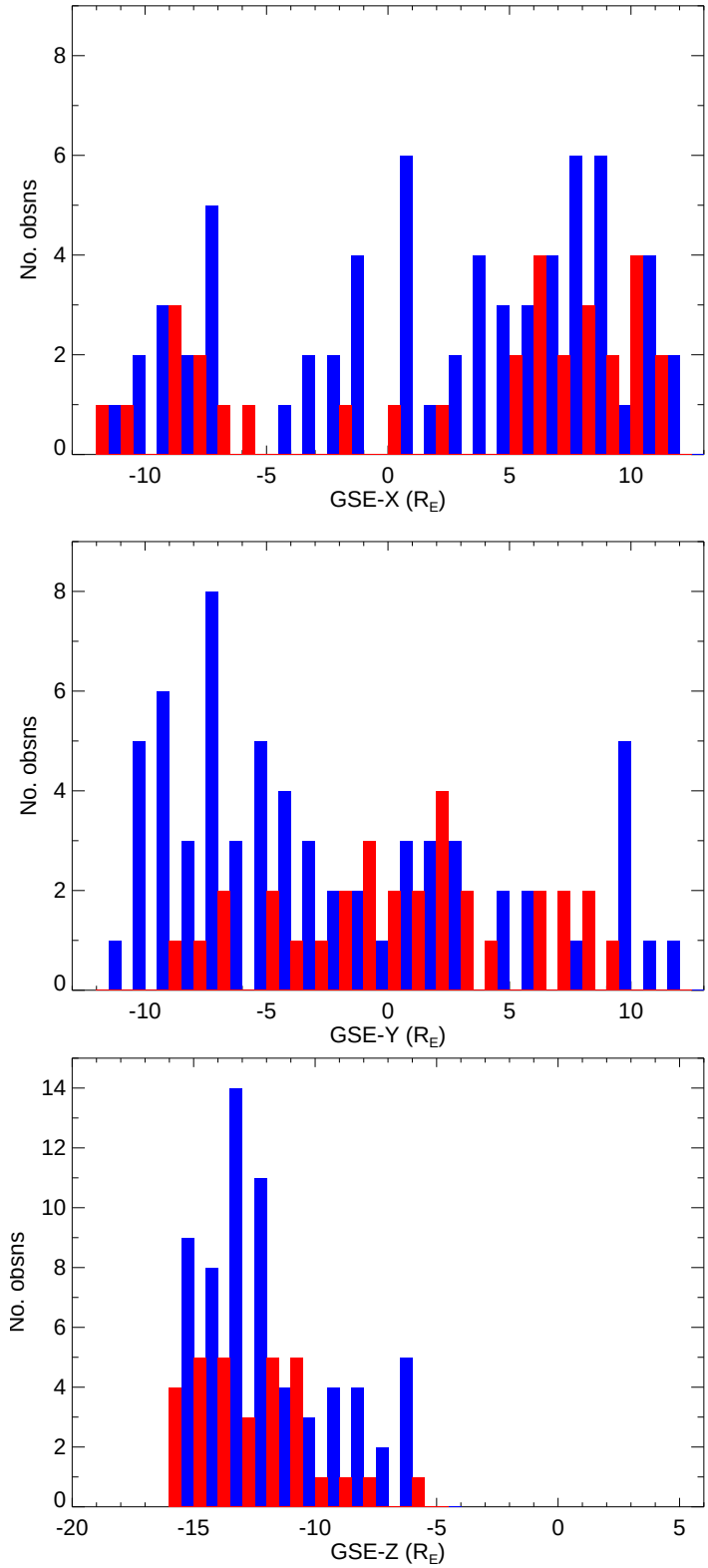


**Figure 8.9:** Histograms of mid-observation (top) GSE-X, (middle) GSE-Y and (bottom) GSE-Z XMM-*Newton* positions for good (blue) and bad (red) fractional differences between the observed and modelled fluxes. The histogram bins have been offset from one another in the plot, for ease of viewing.

is some suggestion that greater model-to-observed flux discrepancies arise in the positive GSE-Y direction which may indicate erosion of the dusk-side magnetosheath.

Chapter 9

# Future missions to observe exospheric SWCX

Growing interest in the charge exchange emission process as a contributor to the total emitted radiation of astronomical targets has led to a sharp increase in the number of publications over the past decade (Dennerl, 2010). This has included studies of local objects, found within the Solar System and local Galactic region, to more distant objects, including studies of galaxies and galaxy clusters. The augmentation of community interest in the charge exchange emission process, in particular from Solar System objects, has led to the idea that exospheric-SWCX may provide a means by which to image the environs of the Earth.

As we as a society become increasingly dependent on space-based technology, the importance of our knowledge and understanding of the interaction between the Sun and Earth becomes more apparent. The complex interplay between the solar wind, magnetosphere, ionosphere and thermosphere requires rigorous study, currently undertaken by a combination of in situ and remote sensing measurements. The magnetosheath has mainly been explored by in situ measurements, although a large-scale, global image of this region would greatly

enhancement our understanding of the plasma dynamics in this area.

Several mission ideas have been suggested in recent years to take advantage of exospheric-SWCX emission and image large regions of the magnetosheath using X-ray instrumentation and these ideas are being disseminated to the community (for example Collier et al. 2010). The author of this thesis has been involved in mission proposals for a lunar-based (*MagEX*, Robertson et al. 2009) and free-flyer imagers (for example STORM, Kuntz et al. 2008). One recent proposal was submitted in response to the ESA's 2010 Cosmic Vision M3 mission call. The project was given the name of AXIOM (Advanced X-ray Imaging of the Magnetosphere, Branduardi-Raymont et al. 2011[1]).

AXIOM would aim to address key questions within the framework of ESA's Cosmic Vision agenda salient point; *'How does the Solar System work?'*. The key science questions by which the instrument design was driven are:

- How do upstream conditions control magnetopause position and shape and magnetosheath thickness?
- How does the location of the magnetopause change in response to prolonged periods of subsolar reconnection?
- Under what conditions do transient boundary layers, such as the plasma depletion layer arise?

AXIOM is a concept for a wide-field X-ray imager (WFI), with the temporal and spatial resolution to answer a selection of fundamental questions regarding the physics of the magnetopause, magnetosheath and bowshock. It would consist of a circularly slumped microchannel plate optic (MPO), with a large area solid-state detector positioned at the focal plane. The

[1] http://www.mssl.ucl.ac.uk/ gbr/AXIOM/index.html

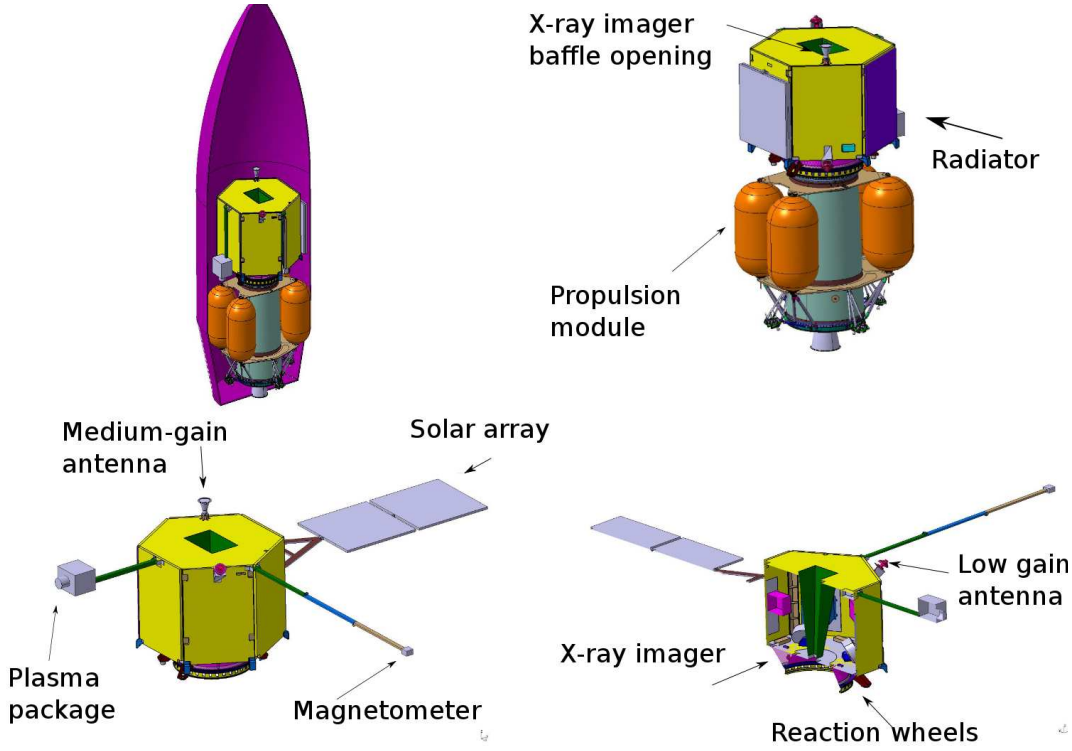


**Figure 9.1:** Basic layout of the AXIOM spacecraft in its housing for launch (top left) and deployed (top right, bottom left and right). Credit: Astrium.

WFI would be supported by a plasma package (consisting of a proton alpha sensor and an ion composition analyser) and a magnetometer, located on a boom extending from the spacecraft. The spacecraft design, including the support spacecraft bus and potential configuration when housed for launch (assuming a Vega launcher), has been proposed by Astrium[2] and is shown in Figure 9.1.

The WFI would be sensitive in the range 0.1 to 2.5 keV, as a minimum requirement for meeting its science targets. The proposal team investigated various configurations of the instrument and presented baseline field-of-view dimensions of $10^\circ \times 15^\circ$, an optical focal length of 70 cm, an energy resolution of $< 65$ eV (FWHM) at 0.6 keV and an angular resolution of better than 2 arcminutes. The baseline configuration was chosen to maximise the scientific output whilst avoiding the hazard of the bright Earth. The design of this instrument was led by the need to optimise the design to observe the most prominent SWCX emission lines of

[2] http://www.astrium.eads.net/

O VII and O VIII. The effective area that could be achieved by the instrument, after applying an iridium coating to the MPO and assuming the use of a UV blocking filter and a CCD detector with a quantum efficiency of 80%, is 37 $cm^2$.

Various orbit options were considered for AXIOM by the industrial collaborators (Astrium) taking into account the mass that could be lifted by a Vega launcher, Sun and bright Earth avoidance and hence orbital efficiency, and the radiation environment of the configuration. Included in the considerations were polar elliptical and equatorial circular orbits with different apogee and perigee distances or different radii. The baseline orbital configuration chosen for AXIOM is a Lissajous orbit at the Earth-Moon Lagrangian 1 position, assuming the use of a propulsion system to acquire the desired formation for science operations. Although periodic house keeping is required in this configuration, this orbit allows for a large duty period during each lunar month with only short periods unavailable for primary science observations. These periods could be used for calibration and to observe secondary science targets such as comets and diffuse heliospheric emission.

The author of this thesis took on the role of providing simulated spectra for the AXIOM proposal. Figure 9.2 shows two simulations of background-subtracted exospheric-SWCX emission, one resulting from an incoming quiescent solar wind with nominal density and velocity and the second from a passing CME. To create this plot, an auxiliary response file was constructed using ray-tracing software developed at Leicester to describe the effective area of an MPO and assuming the quantum efficiency of an EPIC-pn CCD detector. The spectral response of the CCD detector at the focal plane was based on an EPIC-MOS response matrix, modified to improve the low-energy shoulder of the current spectral response seen in the MOS cameras. The SWCX spectrum for quiescent solar wind conditions was constructed using 33 Gaussian emission lines using relative cross-sections between major and minor transitions for a particular ion, taken for a solar wind at 400 $km\,s^{-1}$ (see Chapter 6). The model for the SWCX spectrum resulting from a passing CME was based on that de-

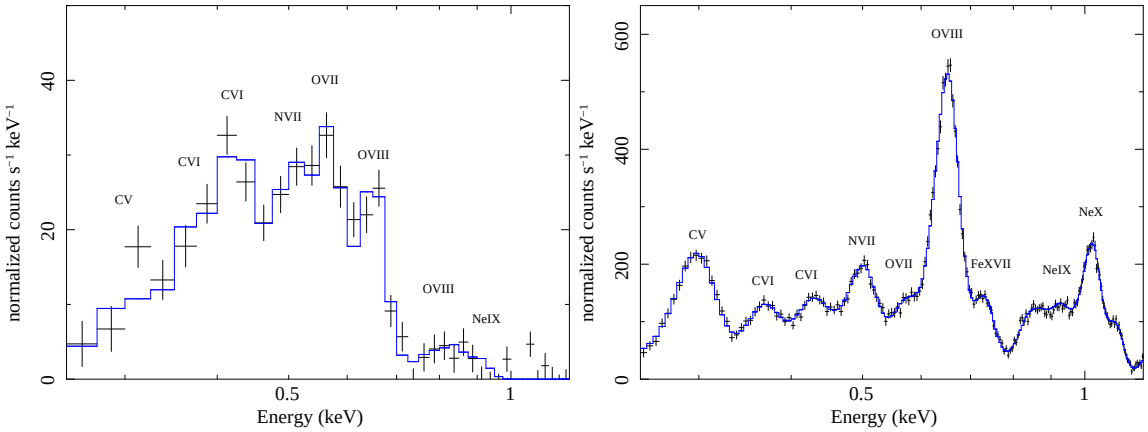


**Figure 9.2:** Simulated background-subtracted spectra produced for the AXIOM proposal (1 ks exposure, total WFI FOV) for emission resulting from (left) quiescent solar wind and (right) from a CME. The major SWCX emission lines have been labelled.

scribed in detail in Chapter 7. The X-ray sky background was modelled to incorporate both the extra-Galactic (unresolved AGN) and local Milky Way X-ray emission (from the halo and Local Hot Bubble) using absorbed power law and Raymond-Smith emission components plus an un-absorbed Raymond-Smith component. A particle-induced X-ray background was added using a model consisting of a power law plus two Gaussian lines representing the fluorescence lines of aluminium and silicon, unfolded through the instrument effective area, see Chapter 2. Both simulations were based on an integration time of 1 ks.

The AXIOM proposal also included simulated WFI images produced by various members of the collaboration. These images were produced for both quiescent and storm (CME) solar wind conditions, for various integration times and were based on the modelling work of Robertson et al. (2006) (and shown in Figure 3.3). These images are shown in Figure 9.3. These images were constructed by folding the expected SWCX emissivity through the detector response and assuming a distance of 51 $R_E$ from the Earth.

At the time of writing, the AXIOM proposal had not, disappointingly, been short-listed by ESA for further study. The authors of the proposal will however continue to promote the mission idea and search for mission opportunities so that the project may progress.

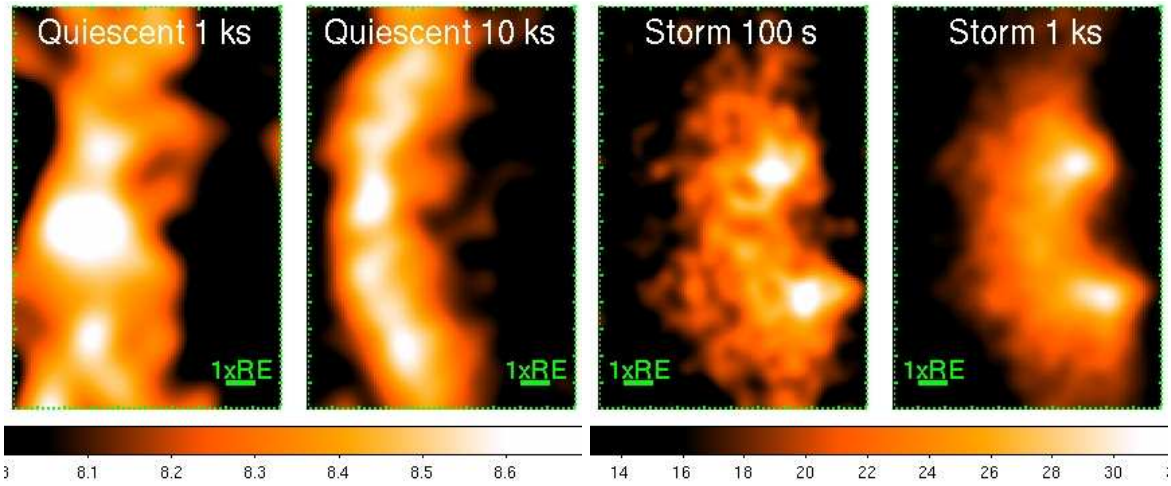


**Figure 9.3:** Simulated WFI images produced for the AXIOM proposal by several collaborators for both quiescent and storm (CME) solar wind conditions, for various integration times. The scale bar is in units of counts $ks^{-1}$ per $0.1^{\circ}$ pixel and the images have been smoothed to bring out detail.

Chapter 10

# Discussion and outlook

We discuss the results presented in this thesis and summarise our main findings. This thesis has shown that exospheric-SWCX emission is not only just one of the various components of the complicated X-ray background for various X-ray astronomical missions, but of interest in its own right scientifically. Observations that have been identified to contain SWCX emission may be used as additional tracers of solar wind constituents, complimenting upstream solar wind monitors. We also comment on potential future areas of investigation involving charge exchange in the Solar System and beyond.

## 10.1 Discussion

We have identified 103 XMM-*Newton* observations, 3.4 % of the sample studied, when temporally variable SWCX emission was present in the data. The timescale of the variability implied that the emission had occurred in the near vicinity of the Earth, i.e. within the exosphere of the Earth or within near interplanetary space. The method presented in this thesis has been able to identify cases of temporally-variable SWCX from within a large sample of

XMM-*Newton* observations using data from the majority of the available archive at the time of the study. This was achieved by identifying periods of a low-energy enhancement, in an energy regime expected to contain the strongest signatures of charge exchange, compared to a higher-energy band which was expected to be free of such features. Two metrics were used to measure the strength of the low-energy enhancement: $\chi^2_\mu$ and $R_\chi$. These values were calculated by comparing two lightcurves, one constructed for the low-energy regime and the second for the higher-energy band. The $\chi^2_\mu$ value was calculated as the reduced-$\chi^2$ computed from a linear fit to a scatter plot between the two lightcurves. The $R_\chi$ was calculated by computing the ratio of the individual $\chi^2$ values from each lightcurve. The SWCX-set cases were taken from those observations presenting the highest $\chi^2_\mu$ and $R_\chi$ values. The corresponding occurrence rate within the sample used in the initial pilot study of Paper I (which has been incorporated into the whole sample presented in this thesis) was $\sim$6.5 %. The data taken from a larger section of the archive and presented in this thesis and published in Paper II covered a wider range in time compared to Paper I. The lower level of detection in the larger sample can be attributed to the reduction in solar activity as this time range extended into a period towards solar minimum. There will be many more XMM-*Newton* observations affected by SWCX, either occurring within the exosphere or near-interplanetary space, such as within the helium focusing cone or at the heliospheric boundary, and undetectable by the method presented in this thesis which has been designed to identify periods of temporally variable emission. SWCX emission occurring within the heliosheath will generally vary over longer periods than exospheric SWCX and so is more suited to detection by observation-to-observation comparison (e.g. observations within the studies of Kuntz & Snowden 2008 and Henley & Shelton 2010). Enhancements from the helium focusing cone will produce some temporal variation but affected observations are strongly constrained by viewing geometry. Those observations within the SWCX-set that involved a line-of-sight that intersected the helium focusing cone did not present remarkable values of a modelled-to-observed flux ratio and therefore the primary source of emission in these cases was taken to be exospheric SWCX.

The method presented in this thesis is only able to identify time-variable SWCX which varies over the length of an observation and therefore the level of contamination quoted in this thesis can only provide a lower limit to the occurrence of exospheric SWCX as observed by XMM-*Newton*. When SWCX emission is only slowly varying or constant over an exposure it will be undetectable by this method. There will also be cases which have slipped detection due to a high percentage of the observation data being removed by the soft proton flare-filtering process, resulting in short lightcurves that are excluded from our analysis. As increased concentrations of solar wind ions in the magnetosheath are expected to mirror increases in the general flux of the solar wind, increased levels of SWCX emission are expected precisely when the flux of solar protons increases. If the on-board radiation monitors of XMM-*Newton* detect a dangerous environment for the satellite, the science instruments are switched into a safe mode which invariably leads to the loss of high SWCX emission periods being available for detection within our sample. Even after soft-proton flare-filtering has been applied to the data, considerable proton contamination may be present. This can result in a significant scatter when plotting either the line-band or continuum lightcurve, whilst potentially masking a clear enhanced period of SWCX-emission during the observation. The level of residual soft-proton contamination may mean that the observation is completely rejected by an observer. If the user does indeed proceed to process the data, the limits presented here on $\chi^2_\mu$ and $R_\chi$ may be useful to guide any further analysis as to whether extra caution should be taken to account for potentially high levels of time-variable SWCX emission. However, they should also be aware that SWCX-emission may still be present even though no time-variable SWCX emission signal has been observed.

We have shown that exospheric SWCX occurs preferentially on the sunward side of the magnetosheath, when the line-of-sight of XMM-*Newton*, pointing towards its astronomical target of interest, intersected the area of strongest expected SWCX emission of the exosphere. This occurs during the northern hemisphere summer months. However, a considerable fraction of the SWCX-affected observations had lines-of-sight that intersected the flanks of the magne-

tosheath, where the SWCX X-ray emission is expected to be weaker. The example presented in Carter et al. (2010) and Chapter 7, along with showing the highest flux of the SWCX set, is one such case whereby XMM-*Newton* was not pointing in the region of strongest expected SWCX flux. This suggests that there are considerable deviations from our current understanding of either or both the hydrogen neutral density and the perturbation of the solar wind in the flank regions of the magnetosheath. A dedicated mission observing SWCX emission to probe the magnetosheath would answer many questions regarding the distribution of mass and mass transfer in the magnetosheath, bowshock and near vicinity of the Earth (Collier et al., 2010).

For each time-variable exospheric-SWCX case and EPIC-MOS instrument, spectra were created for the SWCX-affected and the SWCX-free periods. The resulting spectrum between the two periods became the spectrum used for further spectral analysis (the resultant spectrum). We applied to each resultant spectrum a standardised spectral model of 33 Gaussian lines involving 9 ion species. We set the relative normalisations between emission lines from transitions for one particular species based on ratios of laboratory cross-sections measured for a collisional speed of $400\,\mathrm{km\,s^{-1}}$ between ions and atomic hydrogen. A combined EPIC-MOS flux was calculated between 0.25 and 2.5 keV for each case. The SWCX set showed a large spread in spectrally modelled observed flux. Although the mean solar proton flux during the SWCX-affected period was not a very good indicator of the level of observed flux, there was a positive correlation between these two parameters.

The SWCX set showed a range of spectral characteristics, with O VII and O VIII being the dominant lines. Spectral signatures obtained from these XMM-*Newton* observations, such as the ratio between magnesium and oxygen ion species, may be complementary to data obtained from in-situ solar wind monitors in classifying solar wind plasma types. In addition, a stacked spectrum constructed from all the observations of the SWCX set showed that O VII is by far the most dominant line and that the centroid of the most prominent line is consistent

with the forbidden line transition for this ion species, as expected for the charge exchange emission process.

We have studied the SWCX set with the largest observed flux which we attributed to a CME passing by the Earth. The passage of this CME could be tracked from its signatures at the upwind solar wind monitors ACE and *Wind*, followed by its detection by XMM-*Newton*. This case also formed part of the subset that exhibited the highest Mg XI to O VII and O VIII to O VII ratios. CME plasma is compositionally different to steady state solar wind plasma. Other phenomena, such as co-rotating interacting regions for example, may include high density pulses of plasma but show spectral signatures close to canonical solar wind plasma conditions.

We wished to investigate whether the observed spectrally modelled flux could be estimated using a simple model, constructed using data describing upwind solar wind conditions, and the orbital and target pointing configuration of XMM-*Newton* at the time of each SWCX-set observation. This was first attempted for the specific case of the passing CME, using a static model using the average solar wind conditions at the time of the observation. For the time-dependent model we used simple models of hydrogen densities about the Earth and the perturbations of the solar wind within the region of the magnetosheath. A positive modelled flux, indicating that resultant exospheric SWCX should be detected after taking into account the difference between the SWCX-affected and SWCX-free periods as determined by the X-ray lightcurves, was observed in 80% of cases. Approximately 60% of exospheric-SWCX cases showed an observed-to-modelled flux fractional difference between -1 and 1. Negative values of the modelled flux occurred when the model predicted an emission pulse in the alternative time period to that assigned as the SWCX-affected period. The largest outliers occurred when the solar wind flux was at its weakest. The principal component of the model was the solar wind flux. The presence of the magnetosheath made a large contribution to the modelled emission in a few cases. The actual line-of-sight length through

the magnetosheath did not have any discernable influence on either the observed or modelled flux. The model employed a large parameter space and there are various aspects which are expected to have a large uncertainty. For example the calculation of the time delay from ACE to the Earth will change if the solar wind plasma front is tilted and there are large uncertainties in the distribution of solar wind flow around the magnetosheath, especially in the regions far from the subsolar point. Adapting the model to account for changes in the solar wind $O^{7+}/O^{6+}$ ratio did not improve the observed to modelled flux fractional difference for the SWCX set overall. We have not accounted for any anisotropies in the Earth's exosphere in terms of hydrogen density. In addition there was some suggestion that those cases when XMM-*Newton* was found at positive GSE-Y (the dusk side) resulted in the least well-fitting models, where anisotropies in the shape of the magnetosheath may be most apparent.

This thesis details the analysis of a large data set of XMM-*Newton* archival observations to investigate the incidence of temporally-variable exospheric-SWCX emission over an extended period during the current mission. It is the largest study of SWCX-affected XMM-*Newton* observations to date, and compliments previous work in the literature that has primarily involved the comparison of multiple pointings of the same target field to identify those observations exhibiting signatures of SWCX emission. The technique employed in this work does not require such comparisons between pointings, although is limited to detecting temporally-variable and not steady-state SWCX emission. The positive correlation between the modelled and observed fluxes presented here implies that the model developed has been reasonably successful in determining that exospheric-SWCX emission should be present within a particular dataset. Advances and improvements in the assumptions made in the model, by the author or other interested parties in various research institutes developing similar modelling approaches, will improve the predictive power available to users of XMM-*Newton* when analysing their X-ray observational data.

## 10.2 Outlook

As the solar cycle moves towards its maximum over the next few years, there will be an increase in the frequency of opportunities to study passing transient phenomena such as coronal mass ejections, whose paths may intersect lines-of-sight from space-based X-ray astronomical observatories. Such observations could be prepared for in advance of such an event, and requests for Targets of Opportunity (XMM-*Newton*) or other such discretionary time on other X-ray satellites could be obtained. These observations would be included in any future archival studies of exospheric-SWCX affected XMM-*Newton* observations, which may also incorporate data from the EPIC-pn in the analysis. Any future modelling efforts to estimate the expected line-of-sight emissivity may incorporate solar wind parameters from magneto-hydrodynamical models of the Earth's magnetosheath, to better model the solar wind distribution, particularly in the flank regions.

Charge exchange has been recognised as an important contribution to emission from other extra-Solar System astronomical targets, such as within the rims of supernovae remnants (for example the Cygnus Loop, Katsuda et al. 2011), within the diffuse gas regions of galaxies (for example within M82, Liu et al. 2011) or at boundaries between hot plasma and cold neutral clumps in complex nebulae (for example in the Carina Nebulae, Townsley et al. 2011). Indeed, it will be a ubiquitous emission process throughout the Universe. Charge exchange emitting regions such as cometary comae have been proposed as potential calibration targets for space-based X-ray instrumentation. The charge exchange emission process results in spectra consisting of many emission lines, the number of which depend on the compositional complexity of the plasma involved. Indeed, in the work presented in this thesis, blended lines in spectra from the EPIC-MOS cameras, especially in the energy regime below 0.5 keV, point to the wealth of emission lines that may be found when observing the interaction of solar wind plasma with exospheric neutral hydrogen. Improvements in theoretical and laboratory

cross-sections, involving both single and multi-electron capture processes, will allow more robust models of charge exchange to be tested via astronomical observations, which in turn may aid the low-energy calibration of X-ray instrumentation. Future, high-spectral resolution instruments such as micro-calorimeters will also help in this task.

Future space-based missions to investigate the interaction between the Sun and the Earth could use the exospheric charge-exchange process as a tracer for plasma dynamics in the Earth's magnetosheath. An orbiting satellite, placed at a sufficient distance from the Earth, would be able to image large areas of the magnetosheath providing it was equipped with a large field-of-view optic and adequate effective area. Several proposals based on this premise have been put forward in response to announcements of opportunities for mission concepts. It is hoped that in the relatively near future such a mission will be commissioned and allow this idea to be realised.

# Appendix

**Table A-1:** Table of the SWCX set observations, ranked by $\chi^2_\mu$ (the reduced-$\chi^2$ to the linear fit between the line-band and continuum lightcurves). Also listed for each case are the revolution number (Revn), observation (Obsn), the MOS1 and MOS2 exposure identifiers (Expn M1 and Expn M2) and the ratio of the lightcurve variances ($R_\chi$).

| Ind. | Revn | Obsn | Expn M1 | Expn M2 | $\chi^2_\mu$ | $R_\chi$ | Ind. | Revn | Obsn | Expn M1 | Expn M2 | $\chi^2_\mu$ | $R_\chi$ |
|---|---|---|---|---|---|---|---|---|---|---|---|---|---|
| 1 | 0342 | 0085150301 | U003 | U003 | 27.2 | 10.3 | 53 | 0997 | 0206090201 | S001 | S002 | 2.5 | 2.6 |
| 2 | 0209 | 0093552701 | S001 | S002 | 23.0 | 4.0 | 54 | 0690 | 0134531701 | S002 | S003 | 2.4 | 2.4 |
| 3 | 1014 | 0305920601 | S001 | S002 | 15.0 | 30.9 | 55 | 1023 | 0304531801 | S001 | S002 | 2.4 | 2.2 |
| 4 | 0690 | 0149630301 | S001 | S002 | 14.1 | 21.6 | 56 | 0476 | 0109661201 | S001 | S002 | 2.4 | 2.6 |
| 5 | 0623 | 0150610101 | U002 | U002 | 13.5 | 4.8 | 57 | 1018 | 0212480801 | S001 | S002 | 2.4 | 8.8 |
| 6 | 0339 | 0054540501 | S002 | S003 | 13.2 | 22.4 | 58 | 0871 | 0206360101 | S001 | S002 | 2.4 | 1.3 |
| 7 | 0422 | 0113050401 | S001 | S002 | 12.7 | 12.3 | 59 | 0689 | 0149610401 | S001 | S006 | 2.4 | 1.9 |
| 8 | 0151 | 0094800201 | S001 | S002 | 12.6 | 7.2 | 60 | 0859 | 0203541101 | S001 | S002 | 2.3 | 2.0 |
| 9 | 0657 | 0141980201 | S001 | S002 | 12.0 | 8.1 | 61 | 0354 | 0049340201 | S001 | S002 | 2.3 | 1.8 |
| 10 | 0664 | 0150680101 | S001 | S002 | 9.8 | 5.3 | 62 | 0052 | 0099760201 | S001 | S002 | 2.2 | 1.0 |
| 11 | 0505 | 0153752201 | S002 | S003 | 8.5 | 6.5 | 63 | 0322 | 0094400101 | S001 | S002 | 2.2 | 2.3 |
| 12 | 0271 | 0111550401 | S002 | S005 | 7.8 | 6.9 | 64 | 1232 | 0406420401 | S001 | S002 | 2.1 | 2.3 |
| 13 | 0279 | 0070340501 | S001 | S002 | 7.8 | 2.3 | 65 | 0990 | 0203450201 | S001 | S002 | 2.1 | 4.7 |
| 14 | 0178 | 0101040301 | S001 | S002 | 7.2 | 5.2 | 66 | 0167 | 0106460101 | S001 | S002 | 2.1 | 1.1 |
| 15 | 0139 | 0109060101 | S002 | S003 | 7.0 | 6.1 | 67 | 0395 | 0084140501 | S002 | S003 | 2.1 | 5.8 |
| 16 | 0529 | 0147540101 | S001 | S002 | 6.9 | 7.1 | 68 | 0234 | 0069750101 | S001 | S002 | 2.1 | 1.7 |
| 17 | 1199 | 0402250201 | S001 | S002 | 6.8 | 9.5 | 69 | 0175 | 0110660401 | S002 | S003 | 2.1 | 2.0 |
| 18 | 0676 | 0049540401 | S001 | S002 | 6.5 | 8.9 | 70 | 0554 | 0056021001 | S001 | S002 | 2.0 | 3.5 |
| 19 | 0982 | 0306700301 | S001 | S002 | 6.2 | 9.9 | 71 | 1232 | 0405210601 | S001 | S002 | 2.0 | 1.5 |
| 20 | 0645 | 0150320201 | S001 | S002 | 5.8 | 4.2 | 72 | 0150 | 0105260501 | S001 | S002 | 2.0 | 3.0 |
| 21 | 0630 | 0143150601 | U002 | U002 | 5.7 | 8.0 | 73 | 0634 | 0151400201 | S001 | S002 | 2.0 | 3.4 |
| 22 | 0494 | 0109120101 | S002 | S003 | 5.4 | 7.8 | 74 | 1594 | 0560191501 | S001 | S003 | 2.0 | 1.9 |
| 23 | 0178 | 0110980101 | S001 | S002 | 5.2 | 1.9 | 75 | 0747 | 0200730401 | S001 | S002 | 1.9 | 1.1 |
| 24 | 0114 | 0127921101 | S001 | S002 | 4.9 | 3.8 | 76 | 0428 | 0112520101 | S001 | S002 | 1.9 | 1.2 |
| 25 | 0811 | 0202100301 | S001 | S002 | 4.5 | 3.9 | 77 | 0692 | 0112490301 | S011 | S012 | 1.8 | 1.5 |
| 26 | 0997 | 0303260501 | S001 | S002 | 4.1 | 2.3 | 78 | 0428 | 0112521001 | S001 | S002 | 1.8 | 1.5 |
| 27 | 0163 | 0100640201 | S002 | S003 | 3.7 | 3.7 | 79 | 0875 | 0203750101 | S001 | S002 | 1.8 | 1.9 |
| 28 | 0431 | 0136000101 | S002 | S003 | 3.6 | 2.2 | 80 | 0457 | 0124712501 | S002 | S003 | 1.8 | 2.9 |
| 29 | 0605 | 0146390201 | S001 | S002 | 3.5 | 4.8 | 81 | 0191 | 0093550401 | S001 | S002 | 1.8 | 1.8 |
| 30 | 0906 | 0203361501 | S001 | S002 | 3.4 | 2.7 | 82 | 0882 | 0203610401 | S001 | S003 | 1.8 | 2.2 |
| 31 | 0113 | 0127921001 | S001 | S002 | 3.4 | 2.0 | 83 | 0865 | 0206610201 | S001 | S002 | 1.7 | 1.2 |
| 32 | 0834 | 0200000101 | S001 | S002 | 3.3 | 3.4 | 84 | 1349 | 0406960101 | S001 | S002 | 1.7 | 1.1 |
| 33 | 0846 | 0164560701 | S001 | S002 | 3.3 | 1.8 | 85 | 0750 | 0201160401 | S001 | S002 | 1.6 | 1.8 |
| 34 | 0387 | 0073140501 | S004 | S005 | 3.2 | 1.3 | 86 | 0235 | 0051940501 | S001 | S002 | 1.6 | 2.6 |
| 35 | 1600 | 0553650101 | S001 | S002 | 3.1 | 2.3 | 87 | 0750 | 0201030301 | S001 | S002 | 1.6 | 3.4 |
| 36 | 0555 | 0146510301 | S001 | S002 | 3.0 | 3.5 | 88 | 0420 | 0093190501 | S001 | S002 | 1.5 | 1.0 |
| 37 | 0515 | 0089370501 | S001 | S002 | 2.9 | 2.3 | 89 | 0457 | 0112521301 | S001 | S002 | 1.5 | 2.5 |
| 38 | 1049 | 0300800101 | S002 | S003 | 2.9 | 1.4 | 90 | 0168 | 0101440401 | S001 | S002 | 1.5 | 1.6 |
| 39 | 0376 | 0001930301 | S001 | S002 | 2.9 | 1.6 | 91 | 0369 | 0084230201 | S001 | S002 | 1.5 | 1.3 |
| 40 | 1206 | 0404965401 | S003 | S004 | 2.9 | 1.6 | 92 | 0461 | 0041750101 | S001 | S003 | 1.5 | 1.7 |
| 41 | 0574 | 0110910201 | S002 | S003 | 2.9 | 1.3 | 93 | 0997 | 0201330101 | S001 | S002 | 1.5 | 1.2 |
| 42 | 0136 | 0101440101 | S001 | S002 | 2.9 | 1.7 | 94 | 0630 | 0151390101 | S007 | S008 | 1.5 | 1.2 |
| 43 | 1075 | 0305560101 | S001 | S002 | 2.8 | 2.7 | 95 | 0449 | 0082140301 | S001 | S002 | 1.5 | 1.8 |
| 44 | 0643 | 0141150101 | S001 | S002 | 2.7 | 2.4 | 96 | 0325 | 0085280501 | S001 | S002 | 1.4 | 1.5 |
| 45 | 0918 | 0206430101 | S001 | S002 | 2.7 | 2.2 | 97 | 1555 | 0552410401 | S001 | S002 | 1.4 | 1.0 |
| 46 | 0313 | 0092140101 | S001 | S002 | 2.7 | 2.6 | 98 | 0148 | 0112880801 | S001 | S002 | 1.4 | 1.4 |
| 47 | 0391 | 0085280301 | S001 | S002 | 2.7 | 1.8 | 99 | 0159 | 0112980201 | S001 | S002 | 1.4 | 1.3 |
| 48 | 0173 | 0106660201 | S001 | S002 | 2.7 | 1.2 | 100 | 0676 | 0152460301 | S001 | S002 | 1.3 | 2.8 |
| 49 | 0982 | 0303720301 | S001 | S002 | 2.6 | 2.8 | 101 | 0974 | 0302640101 | S002 | S003 | 1.3 | 1.8 |
| 50 | 0258 | 0112290201 | S001 | S002 | 2.6 | 3.4 | 102 | 1094 | 0306680201 | S001 | S002 | 1.3 | 1.1 |
| 51 | 0260 | 0070340201 | U002 | U002 | 2.6 | 3.3 | 103 | 1364 | 0500500801 | U002 | U002 | 1.3 | 1.7 |
| 52 | 0484 | 0103060201 | S002 | S003 | 2.5 | 1.7 | | | | | | | |

# References

ACUÑA, M. H., OGILVIE, K. W., BAKER, D. N., CURTIS, S. A., FAIRFIELD, D. H. ET AL. (1995). The Global Geospace Science Program and Its Investigations. *Space Science Reviews*, 71, 5–21.

BALUCINSKA-CHURCH, M. & MCCAMMON, D. (1992). Photoelectric absorption cross sections with variable abundances. *ApJ*, 400, 699–+.

BAUTZ, M. W., MILLER, E. D., SANDERS, J. S., ARNAUD, K. A., MUSHOTZKY, R. F. ET AL. (2009). Suzaku Observations of Abell 1795: Cluster Emission to r_200. *PASJ*, 61, 1117–.

BHARDWAJ, A., ELSNER, R. F., RANDALL GLADSTONE, G., CRAVENS, T. E., LISSE, C. M. ET AL. (2007). X-rays from solar system objects. *Planet. Space Sci.*, 55, 1135–1189.

BOCHSLER, P. (2007). Minor ions in the solar wind. *A&A Rev.*, 14, 1–40.

BODEWITS, D. (2007). Cometary X-rays. Solar wind charge exchange in cometary atmospheres. Ph.D. thesis, University of Groningen, P.O. Box 72, 9700 AB Groningen, The Netherlands.

BODEWITS, D., CHRISTIAN, D. J., TORNEY, M., DRYER, M., LISSE, C. M. ET AL. (2007). Spectral analysis of the Chandra comet survey. *A&A*, 469, 1183–1195.

BODEWITS, D., VILLANUEVA, G. L., MUMMA, M. J., LANDSMAN, W. B., CARTER, J. A. ET AL. (2011). Swift-UVOT Grism Spectroscopy of Comets: A First Application to C/2007 N3 (Lulin). *AJ*, 141, 12–+.

BRANDUARDI-RAYMONT, G., BHARDWAJ, A., ELSNER, R. F., GLADSTONE, G. R., RAMSAY, G. ET AL. (2007). A study of Jupiter's aurorae with XMM-Newton. *A&A*, 463, 761–774.

BRANDUARDI-RAYMONT, G., BHARDWAJ, A., ELSNER, R. F. & RODRIGUEZ, P. (2010). X-rays from Saturn: a study with XMM-Newton and Chandra over the years 2002-05. *A&A*, 510, A73+.

BRANDUARDI-RAYMONT, G., SEMBAY, S. F., EASTWOOD, J. P., SIBECK, D. G., ABBEY, A. ET AL. (2011). AXIOM: Advanced X-ray Imaging Of the Magnetosphere. *ArXiv e-prints*.

CARTER, J. A. & READ, A. M. (2007). The XMM-Newton EPIC background and the production of background blank sky event files. *A&A*, 464, 1155–1166.

CARTER, J. A. & SEMBAY, S. (2008). Identifying XMM-Newton observations affected by solar wind charge exchange. Part I. *A&A*, 489, 837–848.

CARTER, J. A., SEMBAY, S. & READ, A. M. (2010). A high charge state coronal mass ejection seen through solar wind charge exchange emission as detected by XMM-Newton. *MNRAS*, 402, 867–878.

CARTER, J. A., SEMBAY, S. & READ, A. M. (2011). Identifying XMM-Newton observations affected by solar wind charge exchange - Part II. *A&A*, 527, A115+.

COLLIER, M. R., MOORE, T. E., SNOWDEN, S. L. & KUNTZ, K. D. (2005). One-up on L1: Can X-rays provide longer advanced warning of solar wind flux enhancements than upstream monitors? *Advances in Space Research,* 35, 2157–2161.

COLLIER, M. R., SIBECK, D. G., CRAVENS, T. E., ROBERTSON, I. P. & OMIDI, N. (2010). Astrophysics Noise: A Space Weather Signal. *Eos Trans. AGU,* 91, 213–214.

COLLIER, M. R., SLAVIN, J. A., LEPPING, R. P., SZABO, A. & OGILVIE, K. (1998). Timing accuracy for the simple planar propagation of magnetic field structures in the solar wind. *Geophys. Res. Lett.*, 25, 2509–2512.

COX, D. P. (1998). in The Local Bubble and Beyond. Berlin: Springer.

CRAVENS, T. E. (1997). Comet Hyakutake x-ray source: Charge transfer of solar wind heavy ions. *Geophys. Res. Lett.*, 24, 105–108.

CRAVENS, T. E. (2000). Heliospheric X-ray Emission Associated with Charge Transfer of the Solar Wind with Interstellar Neutrals. *ApJ,* 532, L153–L156.

CRAVENS, T. E., ROBERTSON, I. P. & SNOWDEN, S. L. (2001). Temporal variations of geocoronal and heliospheric X-ray emission associated with the solar wind interaction with neutrals. *J. Geophys. Res.*, 106, 24883–24892.

DE CHAMBURE, D., LAINÉ, R., VAN KATWIJK, K. & KLETZKINE, P. (1999). XMM's X-ray telescopes. *ESA Bulletin*, 100, 30–42.

DE LUCA, A. & MOLENDI, S. (2004). The 2-8 keV cosmic X-ray background spectrum as observed with XMM-Newton. *A&A*, 419, 837–848.

DENNERL, K. (2006). X-Rays From Mars. *Space Sci. Rev.*, 126, 403–433.

DENNERL, K. (2008). X-rays from Venus observed with Chandra. *Planet. Space Sci.*, 56, 1414–1423.

DENNERL, K. (2010). Charge Transfer Reactions. *Space Sci. Rev.*, 141–+.

DENNERL, K., BURWITZ, V., ENGLHAUSER, J., LISSE, C. & WOLK, S. (2002). Discovery of X-rays from Venus with Chandra. *A&A*, 386, 319–330.

DENNERL, K., ENGLHAUSER, J. & TRÜMPER, J. (1997). X-ray emissions from comets detected in the Röntgen X-ray satellite all-sky survey. *Science*, 277, 1625–1630.

DOMINGO, V., FLECK, B. & POLAND, A. I. (1995). SOHO: The Solar and Heliospheric Observatory. *Space Science Reviews*, 72, 81–84.

EDELSON, R. A. & KROLIK, J. H. (1988). The discrete correlation function - A new method for analyzing unevenly sampled variability data. *ApJ*, 333, 646–659.

EZOE, Y., EBISAWA, K., YAMASAKI, N. Y., MITSUDA, K., YOSHITAKE, H. ET AL. (2010). Time Variability of the Geocoronal Solar-Wind Charge Exchange in the Direction of the Celestial Equator. *PASJ*, 62, 981–.

FAHR, H. J. (1971). The Interplanetary Hydrogen Cone and its Solar Cycle Variations. *A&A*, 14, 263–+.

FAHR, H. J. (1974). The Extraterrestrial UV-Background and the Nearby Interstellar Medium. *Space Science Reviews*, 15, 483–540.

FELDMAN, U., LANDI, E. & SCHWADRON, N. A. (2005). On the sources of fast and slow solar wind. *Journal of Geophysical Research (Space Physics)*, 110, 7109–+.

FRASER, G. W. (1989). X-ray detectors in astronomy.

FREYBERG, M. J. (1998). On the Zero-Level of the Soft X-ray Background. In D. BREITSCHWERDT, M. J. FREYBERG, & J. TRUEMPER, ed., IAU Colloq. 166: The Local Bubble and Beyond, vol. 506 of *Lecture Notes in Physics, Berlin Springer Verlag*. 113–116.

FREYBERG, M. J., BRIEL, U. G., DENNERL, K., HABERL, F., HARTNER, G. D. ET AL. (2004). EPIC pn-CCD detector aboard XMM-Newton: status of the background calibration. In K. A. FLANAGAN & O. H. W. SIEGMUND, ed., Society of Photo-Optical Instrumentation Engineers (SPIE) Conference Series, vol. 5165 of *Society of Photo-Optical Instrumentation Engineers (SPIE) Conference Series*. 112–122.

FUJIMOTO, R., MITSUDA, K., MCCAMMON, D., TAKEI, Y., BAUER, M. ET AL. (2007). Evidence for Solar-Wind Charge-Exchange X-Ray Emission from the Earth's Magnetosheath. *PASJ*, 59, 133–140.

GALEAZZI, M., GUPTA, A., COVEY, K. & URSINO, E. (2007). XMM-Newton Observations of the Diffuse X-Ray Background. *ApJ*, 658, 1081–1087.

GEISS, J., GLOECKLER, G., VON STEIGER, R., BALSIGER, H., FISK, L. A. ET AL. (1995). The Southern High-Speed Stream: Results from the SWICS Instrument on Ulysses. *Science*, 268, 1033–1036.

GLOECKLER, G., CAIN, J., IPAVICH, F. M., TUMS, E. O., BEDINI, P. ET AL. (1998). Investigation of the composition of solar and interstellar matter using solar wind and pickup ion measurements with SWICS and SWIMS on the ACE spacecraft. *Space Science Reviews*, 86, 497–539.

HENLEY, D. B. & SHELTON, R. L. (2008). Comparing Suzaku and XMM-Newton Observations of the Soft X-Ray Background: Evidence for Solar Wind Charge Exchange Emission. *ApJ*, 676, 335–350.

HENLEY, D. B. & SHELTON, R. L. (2010). An XMM-Newton Survey of the Soft X-ray Background. I. The O VII and O VIII Lines Between l = 120° and l = 240°. *ApJS*, 187, 388–408.

HODGES, R. R. J. (1994). Monte Carlo simulation of the terrestrial hydrogen exosphere. *J. Geophys. Res.*, 99, 23229–+.

HOWELL, S. B. (2006). Handbook of CCD astronomy.

JANSEN, F., LUMB, D., ALTIERI, B., CLAVEL, J., EHLE, M. ET AL. (2001). XMM-Newton observatory. I. The spacecraft and operations. *A&A*, 365, L1–L6.

KATSUDA, S., TSUNEMI, H., MORI, K., UCHIDA, H., KOSUGI, H. ET AL. (2011). Possible Charge-exchange X-ray Emission in the Cygnus Loop Detected with Suzaku. *ApJ*, 730, 24–+.

KHAN, H. & COWLEY, S. W. H. (1999). Observations of the response time of high-latitude ionospheric convection to variations in the interplanetary magnetic field using EISCAT and IMP-8 data. *Annales Geophysicae*, 17, 1306–1335.

KOUTROUMPA, D., ACERO, F., LALLEMENT, R., BALLET, J. & KHARCHENKO, V. (2007). OVII and OVIII line emission in the diffuse soft X-ray background: heliospheric and galactic contributions. *A&A*, 475, 901–914.

KOUTROUMPA, D., COLLIER, M. R., KUNTZ, K. D., LALLEMENT, R. & SNOWDEN, S. L. (2009a). Solar Wind Charge Exchange Emission from the Helium Focusing Cone: Model to Data Comparison. *ApJ*, 697, 1214–1225.

KOUTROUMPA, D., LALLEMENT, R., KHARCHENKO, V. & DALGARNO, A. (2009b). The Solar Wind Charge-eXchange Contribution to the Local Soft X-ray Background. Model to Data Comparison in the 0.1–1.0 keV Band. *Space Science Reviews*, 143, 217–230.

KOUTROUMPA, D., LALLEMENT, R., KHARCHENKO, V., DALGARNO, A., PEPINO, R. ET AL. (2006). Charge-transfer induced EUV and soft X-ray emissions in the heliosphere. *A&A*, 460, 289–300.

KRASNOPOLSKY, V. A., GREENWOOD, J. B. & STANCIL, P. C. (2004). X-Ray and extreme ultraviolet emissions from comets. *Space Science Reviews*, 113, 271–374.

KUNTZ, K., COLLIER, M. R., SIBECK, D. G., PORTER, F. S., CARTER, J. A. ET AL. (2008). The Sheath Transport Observer for the Redistribution of Mass (STORM) Imager. *AGU Fall Meeting Abstracts*, A1630+.

KUNTZ, K. D. & SNOWDEN, S. L. (2008). The EPIC-MOS particle-induced background spectra. *A&A*, 478, 575–596.

LALLEMENT, R. (2004). The heliospheric soft X-ray emission pattern during the ROSAT survey: Inferences on Local Bubble hot gas. *A&A*, 418, 143–150.

LISSE, C. M., DENNERL, K., ENGLHAUSER, J., HARDEN, M., MARSHALL, F. E. ET AL. (1996). Discovery of X-ray and Extreme Ultraviolet Emission from Comet C/Hyakutake 1996 B2. *Science*, 274, 205–209.

LIU, J., MAO, S. & WANG, Q. D. (2011). Charge Exchange X-ray Emission of M82: K$\alpha$ triplets of O VII, Ne IX, and Mg XI. *ArXiv e-prints*.

LUMB, D. H., WARWICK, R. S., PAGE, M. & DE LUCA, A. (2002). X-ray background measurements with XMM-Newton EPIC. *A&A*, 389, 93–105.

MANN, R., FOLKMANN, F. & BEYER, H. F. (1981). Selective electron capture into highly stripped Ne and N target atoms after heavy-ion impact. *Journal of Physics B Atomic Molecular Physics*, 14, 1161–1181.

MATEOS, S., SAXTON, R. D., READ, A. M. & SEMBAY, S. (2009). Statistical evaluation of the flux cross-calibration of the XMM-Newton EPIC cameras. *A&A*, 496, 879–889.

MCCOMAS, D. J., BAME, S. J., BARKER, P., FELDMAN, W. C., PHILLIPS, J. L. ET AL. (1998). Solar Wind Electron Proton Alpha Monitor (SWEPAM) for the Advanced Composition Explorer. *Space Science Reviews*, 86, 563–612.

NESS, J., SCHMITT, J. H. M. M. & ROBRADE, J. (2004). Detection of Saturnian X-ray emission with XMM-Newton. *A&A*, 414, L49–L52.

OGILVIE, K. W., CHORNAY, D. J., FRITZENREITER, R. J., HUNSAKER, F. ET AL. (1995). SWE, A Comprehensive Plasma Instrument for the Wind Spacecraft. *Space Science Reviews*, 71, 55–77.

ØSTGAARD, N., MENDE, S. B., FREY, H. U., GLADSTONE, G. R. & LAUCHE, H. (2003). Neutral hydrogen density profiles derived from geocoronal imaging. *Journal of Geophysical Research (Space Physics)*, 108, 1300–+.

OWEN, C. J., MARCHAUDON, A., DUNLOP, M. W., FAZAKERLEY, A. N., BOSQUED, J. ET AL. (2008). Cluster observations of "crater" flux transfer events at the dayside high-latitude magnetopause. *Journal of Geophysical Research (Space Physics)*, 113, 7–+.

PARKER, E. N. (1958). Dynamics of the Interplanetary Gas and Magnetic Fields. *ApJ*, 128, 664–+.

PEPINO, R., KHARCHENKO, V., DALGARNO, A. & LALLEMENT, R. (2004). Spectra of the X-Ray Emission Induced in the Interaction between the Solar Wind and the Heliospheric Gas. *ApJ*, 617, 1347–1352.

PORTER, F. S., ABBEY, T. F., BANNISTER, N. P., CARTER, J. A., COLLIER, M. ET AL. (2008). The Lunar X-ray Observatory (LXO). In Proceedings of the SPIE Conference Series, vol. 7011.

PRADAS, J. & KERP, J. (2005). XMM-Newton data processing for faint diffuse emission. Proton flares, exposure maps and report on EPIC MOS1 bright CCDs contamination. *A&A*, 443, 721–733.

QUEMERAIS, E., LALLEMENT, R. & BERTAUX, J. (1993). Lyman-alpha observations as a possible means for the detection of the heliospheric interface. *J. Geophys. Res.*, 98, 15199–+.

READ, A. M. & PONMAN, T. J. (2003). The XMM-Newton EPIC background: Production of background maps and event files. *A&A*, 409, 395–410.

REISENFELD, D. B., BURNETT, D. S., BECKER, R. H., GRIMBERG, A. G., HEBER, V. S. ET AL. (2007). Elemental Abundances of the Bulk Solar Wind: Analyses from Genesis and ACE. *Space Science Reviews*, 130, 79–86.

RICHARDSON, I. G. & CANE, H. V. (2004). Identification of interplanetary coronal mass ejections at 1 AU using multiple solar wind plasma composition anomalies. *Journal of Geophysical Research (Space Physics)*, 109, 9104–+.

ROBERTSON, I. P., COLLIER, M. R., CRAVENS, T. E. & FOK, M.-C. (2006). X-ray emission from the terrestrial magnetosheath including the cusps. *Journal of Geophysical Research (Space Physics)*, 111, 12105–+.

ROBERTSON, I. P. & CRAVENS, T. E. (2003a). Spatial maps of heliospheric and geocoronal X-ray intensities due to the charge exchange of the solar wind with neutrals. *Journal of Geophysical Research (Space Physics)*, 108, 8031–+.

ROBERTSON, I. P. & CRAVENS, T. E. (2003b). X-ray emission from the terrestrial magnetosheath. *Geophys. Res. Lett.*, 30, 080000–1.

ROBERTSON, I. P., CRAVENS, T. E., SNOWDEN, S. & LINDE, T. (2001). Temporal and Spatial Variations of Heliospheric x-ray Emissions Associated with Charge Transfer of the Solar Wind with Interstellar Neutrals. *Space Science Reviews*, 97, 401–405.

ROBERTSON, I. P., SEMBAY, S., STUBBS, T. J., KUNTZ, K. D., COLLIER, M. R. ET AL. (2009). Solar wind charge exchange observed through the lunar exosphere. *Geophys. Res. Lett.*, 36, 21102–+.

RYUFUKU, H., SASAKI, K. & WATANABE, T. (1980). Oscillatory behavior of charge transfer cross sections as a function of the charge of projectiles in low-energy collisions. *Phys. Rev. A*, 21, 745–750.

SCHMITT, J. H. M. M., SNOWDEN, S. L., ASCHENBACH, B., HASINGER, G., PFEFFERMANN, E. ET AL. (1991). A soft X-ray image of the moon. *Nature*, 349, 583–587.

SCHWADRON, N. A. & CRAVENS, T. E. (2000). Implications of Solar Wind Composition for Cometary X-Rays. *ApJ*, 544, 558–566.

SHUE, J.-H., SONG, P., RUSSELL, C. T., STEINBERG, J. T., CHAO, J. K. ET AL. (1998). Magnetopause location under extreme solar wind conditions. *J. Geophys. Res.*, 103, 17691–17700.

SLAVIN, J. D. (2009). The Origins and Physical Properties of the Complex of Local Interstellar Clouds. *Space Sci. Rev.*, 143, 311–322.

SMITH, R. K., BRICKHOUSE, N. S., LIEDAHL, D. A. & RAYMOND, J. C. (2001). Collisional Plasma Models with APEC/APED: Emission-Line Diagnostics of Hydrogen-like and Helium-like Ions. *ApJ*, 556, L91–L95.

SMITH, R. K., EDGAR, R. J., PLUCINSKY, P. P., WARGELIN, B. J., FREEMAN, P. E. ET AL. (2005). Chandra Observations of MBM 12 and Models of the Local Bubble. *ApJ*, 623, 225–234.

SNOWDEN, S. L., COLLIER, M. R., CRAVENS, T., KUNTZ, K. D., LEPRI, S. T. ET AL. (2009). Observation of Solar Wind Charge Exchange Emission from Exospheric Material in and Outside Earth's Magnetosheath 2008 September 25. *ApJ*, 691, 372–381.

SNOWDEN, S. L., COLLIER, M. R. & KUNTZ, K. D. (2004). XMM-Newton Observation of Solar Wind Charge Exchange Emission. *ApJ*, 610, 1182–1190.

SNOWDEN, S. L., COX, D. P., MCCAMMON, D. & SANDERS, W. T. (1990). A model for the distribution of material generating the soft X-ray background. *ApJ*, 354, 211–219.

SNOWDEN, S. L., FREYBERG, M. J., PLUCINSKY, P. P., SCHMITT, J. H. M. M., TRUEMPER, J. ET AL. (1995). First Maps of the Soft X-Ray Diffuse Background from the ROSAT XRT/PSPC All-Sky Survey. *ApJ*, 454, 643–+.

SNOWDEN, S. L., MUSHOTZKY, R. F., KUNTZ, K. D. & DAVIS, D. S. (2008). A catalog of galaxy clusters observed by XMM-Newton. *A&A*, 478, 615–658.

SPREITER, J. R., SUMMERS, A. L. & ALKSNE, A. Y. (1966). Hydromagnetic flow around the magnetosphere. *Planet. Space Sci.*, 14, 223–+.

STONE, E. C., FRANDSEN, A. M., MEWALDT, R. A., CHRISTIAN, E. R., MARGOLIES, D. ET AL. (1998). The Advanced Composition Explorer. *Space Science Reviews*, 86, 1–22.

STRÜDER, L., BRIEL, U., DENNERL, K., HARTMANN, R., KENDZIORRA, E. ET AL. (2001). The European Photon Imaging Camera on XMM-Newton: The pn-CCD camera. *A&A*, 365, L18–L26.

TOWNSLEY, L. K., BROOS, P. S., CHU, Y., GRUENDL, R. A., OEY, M. S. ET AL. (2011). The Integrated Diffuse X-ray Emission of the Carina Nebula Compared to Other Massive Star-forming Regions. *ArXiv e-prints*.

TURNER, M. J. L., ABBEY, A., ARNAUD, M., BALASINI, M., BARBERA, M. ET AL. (2001). The European Photon Imaging Camera on XMM-Newton: The MOS cameras : The MOS cameras. *A&A*, 365, L27–L35.

WANG, X., WURZ, P., BOCHSLER, P., IPAVICH, F., PAQUETTE, J. ET AL. (2005). Effect of Coronal Mass Ejection Interactions on the SOHO/CELIAS/MTOF Measurements. In DERE, K., WANG, J. & YAN, Y., eds., Coronal and Stellar Mass Ejections, vol. 226 of *IAU Symposium*. 409–413.

WARGELIN, B. J., BEIERSDORFER, P. & BROWN, G. V. (2008). EBIT charge-exchange measurements and astrophysical applications. *Canadian Journal of Physics*, 86, 151–169.

WARGELIN, B. J., MARKEVITCH, M., JUDA, M., KHARCHENKO, V., EDGAR, R. ET AL. (2004). Chandra Observations of the “Dark” Moon and Geocoronal Solar Wind Charge Transfer. *ApJ*, 607, 596–610.

WATSON, M. G., SCHRÖDER, A. C., FYFE, D., PAGE, C. G., LAMER, G. ET AL. (2009). The XMM-Newton serendipitous survey. V. The Second XMM-Newton serendipitous source catalogue. *A&A*, 493, 339–373.

WEISSKOPF, M. C., TANANBAUM, H. D., VAN SPEYBROECK, L. P. & O'DELL, S. L. (2000). Chandra X-ray Observatory (CXO): overview. In TRUEMPER, J. E. & ASCHENBACH, B., eds., Society of Photo-Optical Instrumentation Engineers (SPIE) Conference Series, vol. 4012 of *Society of Photo-Optical Instrumentation Engineers (SPIE) Conference Series*. 2–16.

WELLER, C. S. & MEIER, R. R. (1974). Observations of helium in the interplanetary/interstellar wind - The solar-wake effect. *ApJ*, 193, 471–476.

WELSH, B. Y. & SHELTON, R. L. (2009). The trouble with the Local Bubble. *Ap&SS*, 323, 1–16.

WILMS, J., ALLEN, A. & MCCRAY, R. (2000). On the Absorption of X-Rays in the Interstellar Medium. *ApJ*, 542, 914–924.

WITTE, M., BANASZKIEWICZ, M. & ROSENBAUER, H. (1996). Recent results on the parameters of the interstellar helium from the ULYSSES/GAS experiment. *Space Sci. Rev.*, 78, 289–296.

YAN, M., SADEGHPOUR, H. R. & DALGARNO, A. (1998). Photoionization Cross Sections of He and H 2. *ApJ*, 496, 1044–+.

ZHAO, L., ZURBUCHEN, T. & FISK, L. (2007). ON THE GLOBAL DISTRIBUTION OF SLOW SOLAR WIND. *AGU Fall Meeting Abstracts*, A276+.

ZHAO, L., ZURBUCHEN, T. H. & FISK, L. A. (2009). Global distribution of the solar wind during solar cycle 23: ACE observations. *Geophys. Res. Lett.*, 36, 14104–+.

ZURBUCHEN, T. H., FISK, L. A., GLOECKLER, G. & VON STEIGER, R. (2002). The solar wind composition throughout the solar cycle: A continuum of dynamic states. *Geophys. Res. Lett.*, 29, 090000–1.

ZURBUCHEN, T. H. & RICHARDSON, I. G. (2006). In-Situ Solar Wind and Magnetic Field Signatures of Interplanetary Coronal Mass Ejections. *Space Science Reviews*, 123, 31–43.